Faculty of Mathematics and Physics
Charles University in Prague

ELASTIC FINITE DIFFERENCE SCHEME FOR TOPOGRAPHY MODELS ON IRREGULAR GRIDS

Diploma Thesis

Ivo Opršal

supervisor: Jiří Zahradník

Prague 1996

This research had been carried out at:

Charles University,
Faculty of Mathematics and Physics,
Department of Geophysics,
V Holešovičkách 2,
180 00 Praha 8,
Czech Republic

tel.: 42–2–8576 2546
fax.: 42–2–8576 2555
Email: io@karel.troja.mff.cuni.cz
jz@karel.troja.mff.cuni.cz

Acknowledgements

First of all I want to thank the supervisor of my diploma thesis Doc. RNDr. Jiří Zahradník CSc., for priceless advice and valuable comments that helped me solve the most difficult problems. I would like to thank my mother for the patience and help during my studies.

The results for the comparison were kindly provided by E. Priolo (OGS, Trieste), and S.Gaffet (Sophia-Antipolis I, Valbonne). Thanks are also due to C. A. Cowan (CCR, Leigh-on-Sea) for grammar corrections of the manuscript, and P. Kottnauer (IRSM, Prague) for help with digitizing the data.

This research was financially supported by the Czech Republic grant GAČR 205/96/1743, the NATO SfS GR-COAL grant and the NATO ENVIR.LG 940714 grant.

Contents

Chapter 1

INTRODUCTION

The finite difference (FD) method is used for the forward modelling of the seismic wave propagation by solving the equations of motion for elastic isotropic media.

The models containing material discontinuities have been solved by two approaches: homogeneous and heterogeneous. The homogeneous approach is based on the use of different FD formulas for the internal grid points, and the surface grid points, corners and interfaces (the latter provided by the traction-continuity condition). The heterogeneous approach is using a single FD formula for all the points of the model. The interface conditions for the heterogeneous formulation are fulfilled through the discontinuous material parameters that are entering the discretized equation of motion.

The heterogeneous formulation used for the free surface is called "vacuum formalism", and it is represented by the elastic parameters, and the displacement equal to 0 above the free surface. The effective parameters used in the "vacuum formalism" (Zahradník, Moczo & Hron, 1993); Zahradník, O'Leary & Sochacki, 1994) are evaluated by geometrical averaging that converts the prescribed topography of the free surface into a step-like approximation. After that, the approximated free surface is composed of elementary steps of minimum height and width given by the vertical and the horizontal grid step, respectively.

To avoid the diffraction caused by the "step-like" surface, we have to employ a finer grid in the vicinity of the topographic free surface. The other reason for the fine meshing is the presence of the low velocity zones in which the fine gridding (with respect to wavelength) is necessary for keeping the accuracy of the computation. The fine grid is combined (via the stability condition) with a small time step, hence more computer time and memory is required.

One of the ways how to reduce the computer memory and time is to use an irregular grid. This grid is supposed to be dense in the places with surface topography and/or the low velocity zones.

The FD homogeneous-formulation modelling on the irregular grids [I], and topography [T] have recently been studied by Falk, Tessmer & Grajevski (1995) [I, irregular time step]; Jastram & Tessmer(1994) [I,T]; Hestholm & Ruud (19..)[I,T; Transformation from curved to rectangular grid]; Jih, McLaughlin & Der (1988) [Polygonal topography]; Hong & Bond (1986) [T]; Illan (1977) [T, arbitrary polygonal surface]. Heterogeneous FD formulation was studied by Moczo & Kristek (1996) [I]; Zahradník & Priolo (1995) [regular grid, free surface]; Zahradník & Hron (1992) [regular grid].

The topography models investigated by other methods were recently published by Seriani, Priolo, Carcione & Padovani, (1993)[Spectral Element Method]; Gaffet & Bouchon [Boundary Integral Equation Method]; Nielsen (1994) [Elimination of grid artifacts]; Tessmer, Kosloff & Behle (1992) [Surface topography achieved by mapping a rectangular grid onto a curved grid]; Kawase (1990) [Discrete wavenumber method, hybrid method].

The aim of this thesis is to derive a new FD scheme for the irregular grid (heterogeneous formulation), and to apply it to topography modelS on the irregular grid. The scheme is called $PSi-2$. The derivation of the $PSi-2$ IS based on the $PS-2$ scheme for the regular grid (Zahradník, 1995).

The $PSi-2$ is numerically tested and the results are compared with other methods. The purpose of the tests is to show, whether modelling on the irregular grid can improve the accuracy with respect to the regular grids, what is the efficiency of the irregular grids with respect the regular fine grids, whether the irregular gridding produces numerical artifacts, and how the irregular grids handle the topography models.

Chapter 2

BASIC EQUATIONS

Seismic waves propagating in a 2-D isotropic heterogeneous medium are separated into SH and P-SV waves. The P-SV case can be described by the following elastodynamic equations:

$$\frac{\partial}{\partial x}\left((\lambda+2\mu)\frac{\partial u}{\partial x}\right)+\frac{\partial}{\partial z}\left(\mu\frac{\partial u}{\partial z}\right)+\frac{\partial}{\partial x}\left(\lambda\frac{\partial w}{\partial z}\right)+\frac{\partial}{\partial z}\left(\mu\frac{\partial w}{\partial x}\right)=\rho\frac{\partial^2 u}{\partial t^2}\ , \tag{2.1}$$

$$\frac{\partial}{\partial x}\left(\mu\frac{\partial w}{\partial x}\right)+\frac{\partial}{\partial z}\left((\lambda+2\mu)\frac{\partial w}{\partial z}\right)+\frac{\partial}{\partial x}\left(\mu\frac{\partial u}{\partial z}\right)+\frac{\partial}{\partial z}\left(\lambda\frac{\partial u}{\partial x}\right)=\rho\frac{\partial^2 w}{\partial t^2}\ , \tag{2.2}$$

with u and w denoting the horizontal and vertical displacement components, respectively. The parameters λ and μ are Lamé's elastic coefficients , and ρ is the density. The compressional and shear wave velocities α and β are given by:

$$\alpha = \sqrt{\frac{\lambda + 2\mu}{\rho}} \,,$$

$$\beta = \sqrt{\frac{\mu}{\rho}} \,.$$

The boundary conditions are described in chapter 4.

Chapter 3

PSi-2 SCHEME FOR IRREGULAR GRID

The PSi-2 scheme for an irregular grid is based upon the PS-2 (Zahradník, 1995) scheme for a regular grid.

3.1 Irregular grid

The grid is rectangular with irregularity defined by the spatially varying grid steps DX and DZ (figure 3.1). This allows to make it dense in places where required, e.g. due to topography, low velocity regions inside the model, and along the interfaces. The finite difference approximations for mixed and non-mixed derivatives, appearing in 2-D elastodynamic equations for P-SV waves, are derived for an irregular grid in a similar way to the case of the regular grid studied by Zahradník (1995).

3.2 A *non-mixed* derivative

The second derivative with respect to z is expressed by:

$$\frac{\partial}{\partial z}(a\frac{\partial f}{\partial z}) = \frac{\partial}{\partial z}g\,, \tag{3.1}$$

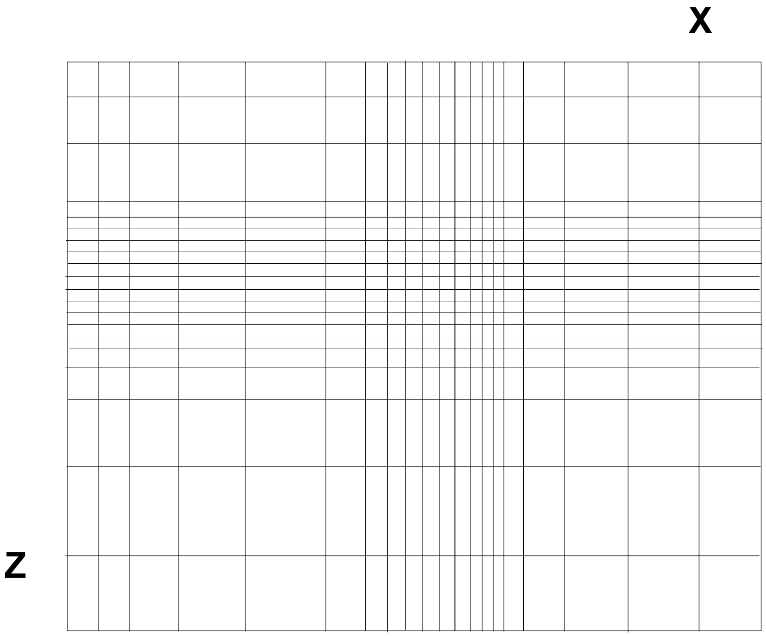

Figure 3.1: *A schematic example of the irregular grid.*

where a is the elastic parameter of the medium, f either the vertical or horizontal component of the displacement, and:

$$g = a \cdot \frac{\partial f}{\partial z} \, . \tag{3.2}$$

If we divide equation 3.2 by a and in sequence integrate both sides from $(0,0)$ to $(0,1)$, then we get:

$$\int_{(0,0)}^{(0,1)} \left.\frac{g}{a}\right|_{x=0} dz = \int_{(0,0)}^{(0,1)} \left.\frac{\partial f}{\partial z}\right|_{x=0} dz \; . \tag{3.3}$$

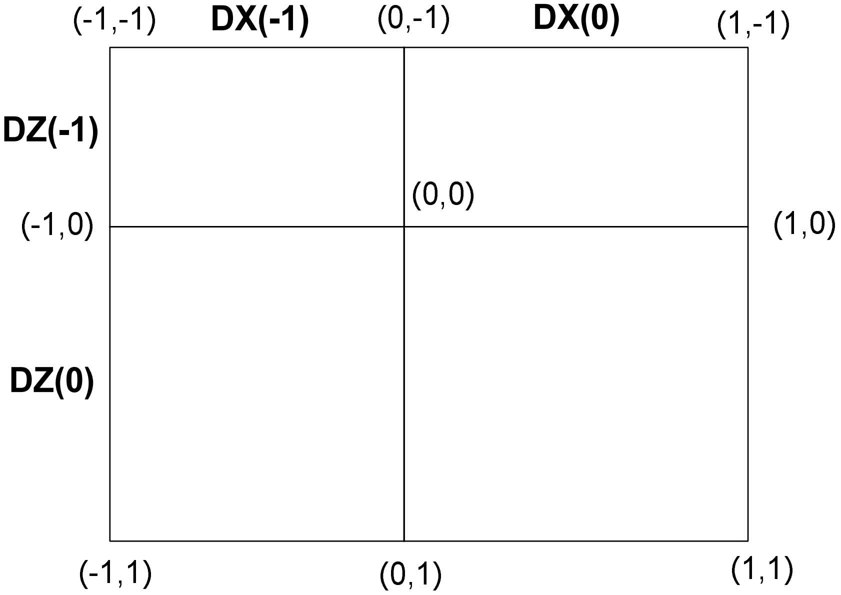

Figure 3.2: *The stencil for the finite difference approximations.*

After applying the mean-value theorem to the left hand side of equation 3.3 we obtain:

$$g_{0,\frac{1}{2}} \int_{(0,0)}^{(0,1)} \left.\frac{dz}{a}\right|_{x=0} = \int_{(0,0)}^{(0,1)} \left.\frac{g}{a}\right|_{x=0} dz \;, \tag{3.4}$$

where $g_{0,\frac{1}{2}}$ is the mean-value of g in point$(0,\frac{1}{2})$.
Let us define:

$$a_s = a_{0,\frac{1}{2}} = DZ(0) \left(\int_{(0,0)}^{(0,1)} \left.\frac{dz}{a}\right|_{x=0} \right)^{-1} \;, \tag{3.5}$$

where a is the parameter of the medium along the grid line $x = 0$ within the interval shown in the integration limits. Then $a_s = a_{0,\frac{1}{2}}$ is the geometric average of a. The distance between $(0,1)$ and $(0,0)$ is specified

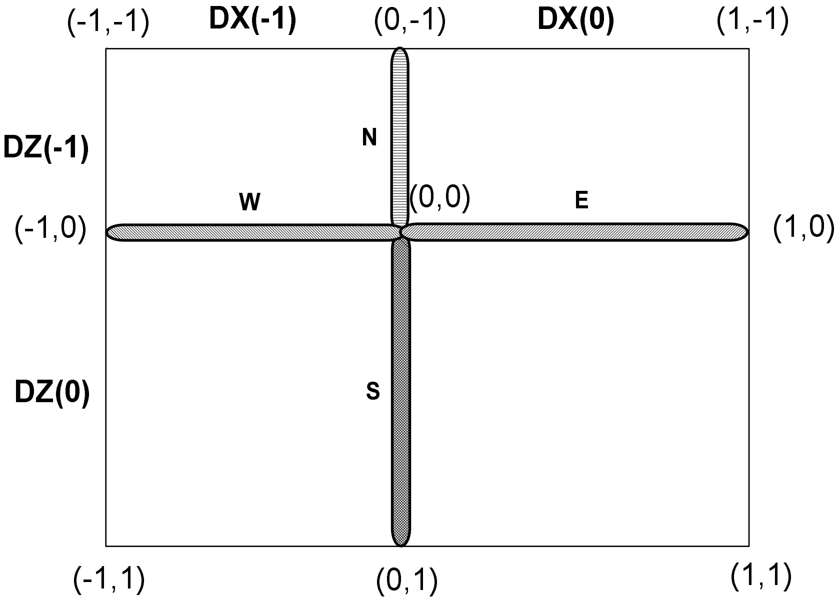

Figure 3.3: *The vertical and horizontal parameters for the following* short-form *approximation to* $\frac{\partial}{\partial x}(\frac{\partial f}{\partial x})$, $\frac{\partial}{\partial z}(\frac{\partial f}{\partial z})$.

by $DZ(0)$.
After inserting equation 3.5 into 3.4 we get:

$$g_{0,\frac{1}{2}} = \frac{a_{0,\frac{1}{2}}}{\mathrm{DZ}(0)} \cdot \int_{(0,0)}^{(0,1)} \frac{\partial f}{\partial z} dz \ . \tag{3.6}$$

The integration of the right-hand side in 3.3 provides:

$$\int_{(0,0)}^{(0,1)} \frac{\partial f}{\partial z} dz = f_{0,1} - f_{0,0} \ , \tag{3.7}$$

where $f_{0,1}, f_{0,0}$ are the point values of u and w respectively. The g approximation is then:

$$g_{0,\frac{1}{2}} = \frac{a_{0,\frac{1}{2}}}{\mathrm{DZ}(0)} \cdot \int_{(0,0)}^{(0,1)} \frac{\partial f}{\partial z} dz = \frac{a_{0,\frac{1}{2}}}{\mathrm{DZ}(0)} \cdot (f_{0,1} - f_{0,0}) \ . \tag{3.8}$$

Proceeding similarly with $g_{0,-\frac{1}{2}}$, we obtain the *non-mixed* second derivative approximation:

$$\frac{\partial}{\partial z}(a\frac{\partial f}{\partial z}) \doteq \frac{g_{0,\frac{1}{2}} - g_{0,-\frac{1}{2}}}{\frac{1}{2}(DZ(-1) + DZ(0))} =$$

$$= 2 \cdot \frac{1}{DZ(-1) + DZ(0)} \cdot \left(a_{\mathrm{s}} \frac{f_{0,1} - f_{0,0}}{DZ(0)} - a_{\mathrm{n}} \frac{f_{0,0} - f_{0,-1}}{DZ(-1)} \right) \tag{3.9}$$

Parameter a_{n} is analogous to a_{s} as shown in figure 3.3. For $h = DZ(-1) = DZ(0)$, i.e. for a regular grid, equation 3.9 transforms to that of regular grid (Zahradník, 1995):

$$\frac{\partial}{\partial z}(a\frac{\partial f}{\partial z}) \doteq \frac{1}{h^2} \cdot (a_{\mathrm{s}}(f_{0,1} - f_{0,0}) -$$

$$-a_{\mathrm{n}}(f_{0,0} - f_{0,-1})) \tag{3.10}$$

Using analogous procedure we get the formula for $\frac{\partial}{\partial x}(a\frac{\partial f}{\partial x})$:

$$\frac{\partial}{\partial x}(a\frac{\partial f}{\partial x}) \doteq 2 \cdot \frac{1}{DX(-1) + DX(0)} \cdot \left(a_{\mathrm{e}} \frac{f_{1,0} - f_{0,0}}{DX(0)} - a_{\mathrm{w}} \frac{f_{0,0} - f_{-1,0}}{DX(-1)} \right) . \tag{3.11}$$

Parameters $a_{\mathrm{e}}, a_{\mathrm{w}}$ are effective parameters as shown in figure 3.3.

3.3 A *mixed* derivative

The *mixed* derivative is approximated in two forms. The conditions of their use are specified later.

3.3.1 Short form

The short form is to be used inside the medium and/or at the interface between two media. It's derivation is similar to that for the *non-mixed* derivative. The expression for the second partial derivative with respect to z and x is

$$\frac{\partial f}{\partial z}(a\frac{\partial}{\partial x}) = \frac{\partial}{\partial z}g \ , \tag{3.12}$$

where

$$\frac{\partial}{\partial z}g \doteq \frac{g_{0,\frac{1}{2}} - g_{0,-\frac{1}{2}}}{(DZ(-1)+DZ(0))} \ , \tag{3.13}$$

where g is evaluated similarly as in equation 3.6:

$$g_{0,\frac{1}{2}} \doteq \frac{\int_{(0,0)}^{(0,1)} \frac{\partial f}{\partial x}\Big|_{x=0} dz}{\int_{(0,0)}^{(0,1)} \frac{dz}{a}\Big|_{x=0} dz} = \tag{3.14}$$

$$= \frac{a_{\mathrm{s}}}{DZ(0)} \cdot \int_{(0,0)}^{(0,1)} \frac{\partial f}{\partial x}\bigg|_{x=0} dz \ . \tag{3.15}$$

Parameter a_{s} is defined as before by harmonic averaging, see figure 3.3, but (in contrast to equation 3.6) the integral

$$\int_{(0,0)}^{(0,1)} \frac{\partial f}{\partial x}\bigg|_{x=0} dz \tag{3.16}$$

cannot be calculated exactly now. However, we can use the following approximation:

$$g_{0,\frac{1}{2}} \doteq \frac{a_{\mathrm{s}}}{DZ(0)} \cdot \frac{\partial f}{\partial x}\bigg|_{0,\frac{1}{2}} \cdot DZ(0) \doteq$$

$$\doteq a_{\mathrm{s}} \cdot \frac{f_{1,\frac{1}{2}} - f_{-1,\frac{1}{2}}}{DX(-1)+DX(0)} \ .$$

Assuming further

$$f_{1,\frac{1}{2}} = \frac{f_{1,0}+f_{1,1}}{2} \ ,$$

$$f_{-1,\frac{1}{2}} = \frac{f_{-1,0}+f_{-1,1}}{2} \ ,$$

then

$$g_{0,\frac{1}{2}} \doteq \frac{a_{\mathrm{s}}}{DX(-1)+DX(0)} \cdot \frac{1}{2} \cdot (f_{1,0}+f_{1,1}) - (f_{-1,0}+f_{-1,1})) \ . \qquad (3.17)$$

Treating $g_{0,-\frac{1}{2}}$ likewise leads to the *mixed-derivative* finite difference approximation of g. Thus the so-called *short form* reads:

$$\frac{\partial}{\partial z}(a\frac{\partial f}{\partial x}) \doteq$$

$$\doteq \frac{1}{DZ(-1)+DZ(0)} \cdot \frac{1}{DX(-1)+DX(0)} \cdot$$

$$\cdot \left[a_{\mathrm{s}}\,(f_{1,0}+f_{1,1}-f_{-1,0}-f_{-1,1}) - a_{\mathrm{n}}\,(f_{1,-1}+f_{1,0}-f_{-1,-1}-f_{-1,0})\right] \qquad (3.18)$$

For $DZ(-1) = DZ(0)$ and $DX(-1) = DX(0)$ the equation 3.18 simplifies to that of the regular grid of Zahradník (1995):

$$\frac{\partial}{\partial z}(a\frac{\partial f}{\partial x}) \doteq$$

$$\doteq 2 \cdot \frac{1}{4h^2} \cdot [a_{\mathrm{s}}\,(f_{1,0}+f_{1,1}-f_{-1,0}-f_{-1,1}) -$$

$$-a_{\mathrm{n}}\,(f_{1,-1}+f_{1,0}-f_{-1,-1}-f_{-1,0})] \qquad (3.19)$$

Using analogous procedure we get the approximation of $\frac{\partial f}{\partial x}(a\frac{\partial}{\partial z})$:

$$\frac{\partial}{\partial x}(a\frac{\partial f}{\partial z}) \doteq \frac{1}{DZ(-1)+DZ(0)} \cdot \frac{1}{DX(-1)+DX(0)} \cdot$$

$$\cdot \left[a_{\mathrm{e}}\,(f_{0,1}+f_{1,1}-f_{0,-1}-f_{1,-1}) - a_{\mathrm{w}}\,(f_{-1,1}+f_{0,1}-f_{-1,-1}-f_{0,-1})\right] \ . \qquad (3.20)$$

Parameters $a_{\mathrm{e}}, a_{\mathrm{w}}$ are effective parameters as shown in figure 3.2.

3.3.2 Full form

The following approximation is designed mainly to treat the *free-surface* grid points (shown later). The *full form* can be also used for internal grid points, but more computer time is needed.

The *full-form* approximation is using the g function, but, in contrast to the *short-form* stencil, the values of the first derivatives and effective parameters are needed at the locations between the grid lines (see fig. 3.4, 3.5).

$$\frac{\partial}{\partial z}\left(a\frac{\partial f}{\partial x}\right) = \frac{\partial}{\partial z} g\ '$$

the *full-form* is defined as:

$$\frac{\partial}{\partial z} g \doteq \frac{1}{2} \cdot \frac{(g_{-\frac{1}{2},\frac{1}{2}} + g_{\frac{1}{2},\frac{1}{2}}) - (g_{-\frac{1}{2},-\frac{1}{2}} + g_{\frac{1}{2},-\frac{1}{2}})}{(DZ(-1) + DZ(0))} \ . \tag{3.21}$$

After applying the mean-value theorem, the g-value in point $(\frac{1}{2},\frac{1}{2})$ is:

$$g_{\frac{1}{2},\frac{1}{2}} \doteq \frac{a_{\mathrm{se}}}{\mathrm{DX}(0)} \cdot \left.\frac{\partial f}{\partial x}\right|_{(\frac{1}{2},\frac{1}{2})} \cdot (DX(0)) \doteq ,$$

$$\doteq \frac{a_{\mathrm{se}}}{DX(0)} \cdot (f_{1,\frac{1}{2}} - f_{0,\frac{1}{2}}) \ .$$

We again use:

$$f_{1,\frac{1}{2}} = \frac{f_{1,0} + f_{1,1}}{2} \ ,$$

$$f_{0,\frac{1}{2}} = \frac{f_{0,0} - f_{0,1}}{2} \ ,$$

thus:

$$g_{\frac{1}{2},\frac{1}{2}} \doteq \frac{a_{\mathrm{se}}}{2 \cdot DX(0)} \cdot \ (f_{1,0} + f_{1,1} - f_{0,0} - f_{0,1}) \ . \tag{3.22}$$

The complete stencil, made of four parts constructed likewise, is:

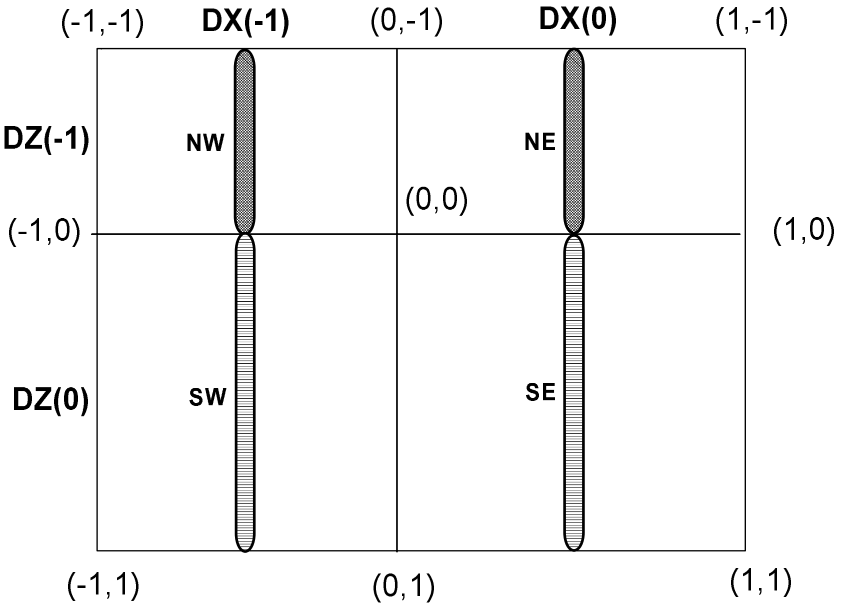

Figure 3.4: *The vertical parameters for the* full-form *approximation to* $\frac{\partial}{\partial z}(\frac{\partial f}{\partial x})$.

$$
\begin{aligned}
\frac{\partial}{\partial z}(a\frac{\partial f}{\partial x}) = \frac{\partial}{\partial z}g \doteq \\
\doteq \frac{\frac{1}{2}}{DZ(-1)+DZ(0)} \cdot \Big[a_{\text{se}} \cdot \frac{1}{DX(0)}(f_{1,0}+f_{1,1}-f_{0,0}-f_{0,1}) + \\
+ a_{\text{sw}} \cdot \frac{1}{DX(-1)}(f_{0,0}+f_{0,1}-f_{-1,0}-f_{-1,1}) - \\
- a_{\text{ne}} \cdot \frac{1}{DX(0)}(f_{1,-1}+f_{1,0}-f_{0,-1}-f_{0,0}) - \\
- a_{\text{nw}} \cdot \frac{1}{DX(-1)}(f_{0,-1}+f_{0,0}-f_{-1,-1}-f_{-1,0}) \Big] \; . \qquad (3.23)
\end{aligned}
$$

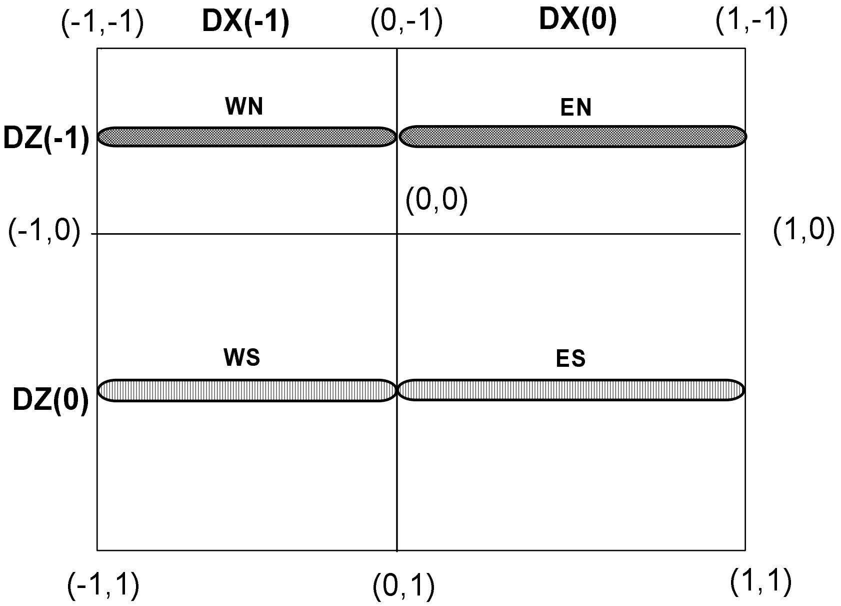

Figure 3.5: *The horizontal parameters for the* full-form *approximation to* $\frac{\partial}{\partial x}(\frac{\partial f}{\partial z})$.

Parameters $a_{\text{se}}, a_{\text{sw}}, a_{\text{ne}}, a_{\text{nw}}$ are effective parameters belonging to the particular arms of the finite difference stencil, see figure 3.4 For $DZ(-1) = DZ(0)$ and $DX(-1) = DX(0)$ the equation again simplifies to the case of regular grid (Zahradník, 1995).

With $h = DZ(-1) = DX(0)$ we get:

$$\frac{\partial}{\partial z}(a\frac{\partial f}{\partial x}) = \frac{\partial}{\partial z}g \doteq$$

$$\doteq \frac{1}{4h^2} \cdot [a_{\text{se}}(f_{1,0} + f_{1,1} - f_{0,0} - f_{0,1}) + a_{\text{sw}}(f_{0,0} + f_{0,1} - f_{-1,0} - f_{-1,1}) -$$

$$-a_{\mathrm{ne}}(f_{1,-1}+f_{1,0}-f_{0,-1}-f_{0,0})-a_{\mathrm{nw}}(f_{0,-1}+f_{0,0}-f_{-1,-1}-f_{-1,0})] \ . \tag{3.24}$$

In a similar way we get :

$$\frac{\partial}{\partial z}(a\frac{\partial f}{\partial x}) = \frac{\partial}{\partial z}g \doteq$$

$$\begin{aligned}\doteq \frac{\frac{1}{2}}{DZ(-1)+DZ(0)} \cdot \Bigg[& a_{\mathrm{se}} \cdot \frac{1}{DX(0)}(f_{1,0}+f_{1,1}-f_{0,0}-f_{0,1})+ \\ & +a_{\mathrm{sw}} \cdot \frac{1}{DX(-1)}(f_{0,0}+f_{0,1}-f_{-1,0}-f_{-1,1})- \\ & -a_{\mathrm{ne}} \cdot \frac{1}{DX(0)}(f_{1,-1}+f_{1,0}-f_{0,-1}-f_{0,0})- \\ & -a_{\mathrm{nw}} \cdot \frac{1}{DX(-1)}(f_{0,-1}+f_{0,0}-f_{-1,-1}-f_{-1,0}) \Bigg] \ . \end{aligned} \tag{3.25}$$

Parameters $a_{\mathrm{se}}, a_{\mathrm{sw}}, a_{\mathrm{ne}}, a_{\mathrm{nw}}$ are the same as in equation 3.22. The derivative $\frac{\partial}{\partial x}(a\frac{\partial f}{\partial z})$ is quite analogous:

$$\frac{\partial}{\partial x}(a\frac{\partial}{\partial z}) \doteq$$

$$\begin{aligned}\doteq \frac{\frac{1}{2}}{DX(-1)+DX(0)} \cdot \Bigg[& a_{\mathrm{es}} \cdot \frac{1}{DZ(0)}(f_{0,1}+f_{1,1}-f_{0,0}-f_{1,0})+ \\ & +a_{\mathrm{en}} \cdot \frac{1}{DZ(-1)}(f_{0,0}+f_{1,0}-f_{0,-1}-f_{1,-1})- \\ & -a_{\mathrm{ws}} \cdot \frac{1}{DZ(0)}(f_{-1,1}+f_{0,1}-f_{-1,0}-f_{0,0})- \\ & -a_{\mathrm{wn}} \cdot \frac{1}{DZ(-1)}(f_{-1,0}+f_{0,0}-f_{-1,-1}-f_{0,-1}) \Bigg] \ . \end{aligned} \tag{3.26}$$

Parameters $a_{\mathrm{es}}, a_{\mathrm{ws}}, a_{\mathrm{en}}, a_{\mathrm{wn}}$ are effective parameters belonging to the particular arms of the finite difference stencil (figure 3.5).

3.3.3 The finite-difference approximation to the space derivatives

Let us denote $L_u(u,w)$, and $L_w(u,w)$ the FD approximation of the left-hand side of equations 2.1, 2.2, respectively. Then the short-form approximation for the u component is:

$$
\begin{gathered}
L_u(u,w) = 2 \cdot \frac{1}{DX(-1)+DX(0)} \cdot \\
\cdot \left((\lambda_{\mathrm{e}} + 2\mu_{\mathrm{e}}) \frac{u_{1,0}-u_{0,0}}{DX(0)} - (\lambda_{\mathrm{w}} + 2\mu_{\mathrm{w}}) \frac{u_{0,0}-u_{-1,0}}{DX(-1)} \right) + \\
+2 \cdot \frac{1}{DZ(-1)+DZ(0)} \cdot \left(\mu_{\mathrm{s}} \frac{u_{0,1}-u_{0,0}}{DZ(0)} - \mu_{\mathrm{n}} \frac{u_{0,0}-u_{0,-1}}{DZ(-1)} \right) + \\
+ \frac{1}{DZ(-1)+DZ(0)} \cdot \frac{1}{DX(-1)+DX(0)} \cdot \\
\cdot \left[\lambda_{\mathrm{e}} \left(w_{0,1} + w_{1,1} - w_{0,-1} - w_{1,-1} \right) - \right. \\
\left. - \lambda_{\mathrm{w}} \left(w_{-1,1} + w_{0,1} - w_{-1,-1} - w_{0,-1} \right) \right] + \\
+ \frac{1}{DZ(-1)+DZ(0)} \cdot \frac{1}{DX(-1)+DX(0)} \cdot \\
\cdot \left[\lambda_{\mathrm{s}} \left(w_{1,0} + w_{1,1} - w_{-1,0} - w_{-1,1} \right) - \lambda_{\mathrm{n}} \left(w_{1,-1} + w_{1,0} - w_{-1,-1} - w_{-1,0} \right) \right] \ ,
\end{gathered}
\tag{3.27}
$$

for w component:

$$
\begin{gathered}
L_w(u,w) = \\
= 2 \cdot \frac{1}{DX(-1)+DX(0)} \cdot \left(\mu_{\mathrm{e}} \frac{w_{1,0}-w_{0,0}}{DX(0)} - \mu_{\mathrm{w}} \frac{w_{0,0}-w_{-1,0}}{DX(-1)} \right) + \\
+2 \cdot \frac{1}{DZ(-1)+DZ(0)} \cdot \\
\cdot \left((\lambda_{\mathrm{s}} + 2\mu_{\mathrm{s}}) \frac{w_{0,1}-w_{0,0}}{DZ(0)} - (\lambda_{\mathrm{n}} + 2\mu_{\mathrm{n}}) \frac{w_{0,0}-w_{0,-1}}{DZ(-1)} \right) +
\end{gathered}
$$

$$
\begin{aligned}
&+\frac{1}{DZ(-1)+DZ(0)}\cdot\frac{1}{DX(-1)+DX(0)}\cdot\\
&\cdot\left[\mu_{\mathrm{e}}\left(u_{0,1}+u_{1,1}-u_{0,-1}-u_{1,-1}\right)-\mu_{\mathrm{w}}\left(u_{-1,1}+u_{0,1}-u_{-1,-1}-u_{0,-1}\right)\right]+\\
&+\frac{1}{DZ(-1)+DZ(0)}\cdot\frac{1}{DX(-1)+DX(0)}\cdot\\
&\cdot\left[\mu_{\mathrm{s}}\left(u_{1,0}+u_{1,1}-u_{-1,0}-u_{-1,1}\right)-\right.\\
&\left.-\mu_{\mathrm{n}}\left(u_{1,-1}+u_{1,0}-u_{-1,-1}-u_{-1,0}\right)\right]\ . \qquad (3.28)
\end{aligned}
$$

Similarly the full-form approximation for the u component is:

$$
\begin{aligned}
&L_u(u,w)=2\cdot\frac{1}{DX(-1)+DX(0)}\cdot\\
&\cdot\left((\lambda_{\mathrm{e}}+2\mu_{\mathrm{e}})\frac{u_{1,0}-u_{0,0}}{DX(0)}-(\lambda_{\mathrm{w}}+2\mu_{\mathrm{w}})\frac{u_{0,0}-u_{-1,0}}{DX(-1)}\right)+\\
&+2\cdot\frac{1}{DZ(-1)+DZ(0)}\cdot\left(\mu_{\mathrm{s}}\frac{u_{0,1}-u_{0,0}}{DZ(0)}-\mu_{\mathrm{n}}\frac{u_{0,0}-u_{0,-1}}{DZ(-1)}\right)+\\
&+\frac{\frac{1}{2}}{DX(-1)+DX(0)}\cdot\left[\lambda_{\mathrm{es}}\cdot\frac{1}{DZ(0)}(w_{0,1}+w_{1,1}-w_{0,0}-w_{1,0})+\right.\\
&+\lambda_{\mathrm{en}}\cdot\frac{1}{DZ(-1)}(w_{0,0}+w_{1,0}-w_{0,-1}-w_{1,-1})-\\
&-\lambda_{\mathrm{ws}}\cdot\frac{1}{DZ(0)}(w_{-1,1}+w_{0,1}-w_{-1,0}-w_{0,0})-\\
&\left.-\lambda_{\mathrm{wn}}\cdot\frac{1}{DZ(-1)}(w_{-1,0}+w_{0,0}-w_{-1,-1}-w_{0,-1})\right]+\\
&+\frac{\frac{1}{2}}{DZ(-1)+DZ(0)}\cdot\left[\lambda_{\mathrm{se}}\cdot\frac{1}{DX(0)}(w_{1,0}+w_{1,1}-w_{0,0}-w_{0,1})+\right.\\
&+\lambda_{\mathrm{sw}}\cdot\frac{1}{DX(-1)}(w_{0,0}+w_{0,1}-w_{-1,0}-w_{-1,1})-
\end{aligned}
$$

$$-\lambda_{\mathrm{ne}} \cdot \frac{1}{DX(0)}(w_{1,-1} + w_{1,0} - w_{0,-1} - w_{0,0}) -$$

$$-\lambda_{\mathrm{nw}} \cdot \frac{1}{DX(-1)}(w_{0,-1} + w_{0,0} - w_{-1,-1} - w_{-1,0})\Big] \ , \tag{3.29}$$

and the full-form approximation for the w component is:

$$L_w(u, w) =$$

$$= 2 \cdot \frac{1}{DX(-1) + DX(0)} \cdot \left(\mu_{\mathrm{e}} \frac{w_{1,0} - w_{0,0}}{DX(0)} - \mu_{\mathrm{w}} \frac{w_{0,0} - w_{-1,0}}{DX(-1)}\right) +$$

$$+2 \cdot \frac{1}{DZ(-1) + DZ(0)} \cdot$$

$$\cdot \left((\lambda_{\mathrm{s}} + 2\mu_{\mathrm{s}}) \frac{w_{0,1} - w_{0,0}}{DZ(0)} - (\lambda_{\mathrm{n}} + 2\mu_{\mathrm{n}}) \frac{w_{0,0} - w_{0,-1}}{DZ(-1)}\right) +$$

$$+ \frac{\frac{1}{2}}{DX(-1) + DX(0)} \cdot \Big[\mu_{\mathrm{es}} \cdot \frac{1}{DZ(0)}(u_{0,1} + u_{1,1} - u_{0,0} - u_{1,0}) +$$

$$+\mu_{\mathrm{en}} \cdot \frac{1}{DZ(-1)}(u_{0,0} + u_{1,0} - u_{0,-1} - u_{1,-1}) -$$

$$-\mu_{\mathrm{ws}} \cdot \frac{1}{DZ(0)}(u_{-1,1} + u_{0,1} - u_{-1,0} - u_{0,0}) -$$

$$-\mu_{\mathrm{wn}} \cdot \frac{1}{DZ(-1)}(u_{-1,0} + u_{0,0} - u_{-1,-1} - u_{0,-1})\Big] +$$

$$+ \frac{\frac{1}{2}}{DZ(-1) + DZ(0)} \cdot \Big[\mu_{\mathrm{se}} \cdot \frac{1}{DX(0)}(u_{1,0} + u_{1,1} - u_{0,0} - u_{0,1}) +$$

$$+\mu_{\mathrm{sw}} \cdot \frac{1}{DX(-1)}(u_{0,0} + u_{0,1} - u_{-1,0} - u_{-1,1}) -$$

$$-\mu_{\mathrm{ne}} \cdot \frac{1}{DX(0)}(u_{1,-1} + u_{1,0} - u_{0,-1} - u_{0,0}) -$$

$$-\mu_{\mathrm{nw}} \cdot \frac{1}{DX(-1)}(u_{0,-1} + u_{0,0} - u_{-1,-1} - u_{-1,0})\Big] \ . \tag{3.30}$$

3.3.4 The finite-difference approximation to the time derivative

For the computation of the wavefield we need discretized time, proceeding with the constant step Δt (the value of Δt is discussed in section *Stability and accuracy* (3.3.6)). The time of the M^{th} level is determined by:

$$t = M \cdot \Delta t \quad .$$

Let us define each of the displacement components:

1. At a "new" time level (computed time level): $f_{i,j}^{M+1}$
2. At a "present" time level: $f_{i,j}^{M}$
3. At an "old" time level: $f_{i,j}^{M-1}$

The value of f is defined at point (i,j), with $i,j \in \{-1,1\}$, which represents the same scheme as shown in figure 3.2 . The second derivative with respect to time in grid point $k=i$, $l=j$ is approximated by:

$$\frac{\partial^2 f}{\partial t^2} \doteq \frac{f_{i,j}^{M+1} - 2f_{i,j}^{M} + f_{i,j}^{M-1}}{(\Delta t)^2} \tag{3.31}$$

Let us define $L_u^M(u,w)$, and $L_w^M(u,w)$ as the operators $L_u(u,w)$, and $L_w(u,w)$ (discussed in 3.3.3) at the time level M.

After inserting $L_u^M(u,w)$ and equation 3.31 into 2.1 we get :

$$L_u^M(u,w) = \rho_{i,j} \frac{U_{i,j}^{M+1} - 2U_{i,j}^{M} + U_{i,j}^{M-1}}{(\Delta t)^2} \;, \tag{3.32}$$

where $\rho_{i,j}$ is the density in grid point (i,j). From 3.32 we get the approximation for the u component of displacement at a "new" time level in grid point $k=i$, $l=j$:

$$U_{i,j}^{M+1} = \frac{(\Delta t)^2}{\rho_{i,j}} L_u^M(u,w) + 2U_{i,j}^{M} - U_{i,j}^{M-1} \;, \tag{3.33}$$

analogously for equation 2.2 we get:

$$W_{i,j}^{M+1} = \frac{(\Delta t)^2}{\rho_{i,j}} L_w^M(u,w) + 2W_{i,j}^M - W_{i,j}^{M-1} \,, \tag{3.34}$$

Equations 3.33 and 3.34 are explicit FD approximations to equations 2.1, 2.2, respectively. These equations, together with 3.27, 3.3.3, 3.29, 3.30 represent the main formulas of this thesis.

3.3.5 Consistency with *free-surface* boundary conditions

We investigate the boundary behaviour of our scheme for a typical model surface by inserting Taylor's expansion for the u and the w components into FD approximations given by equations 3.33, 3.34. In this case, for simplicity, we assume a regular grid with grid steps $\Delta x = \Delta z = h$, and a homogeneous medium with λ, μ being the elastic parameters. The free-surface specifications are in figure 3.6.

- horizontal planar surface
  for 3.33:

$$0 + o(t^2) = (\mu U_z + \mu W_x) + o(h) \tag{3.35}$$

  for 3.34:

$$0 + o(t^2) = ((\lambda + 2\mu) W_z + \lambda U_x) + o(h) \tag{3.36}$$

- vertical planar surface:
  for 3.33:

$$0 + o(t^2) = (-(\lambda + 2\mu) U_x - \lambda W_z) + o(h) \tag{3.37}$$

  for 3.34:

$$0 + o(t^2) = (-\mu W_x - \mu U_z) + o(h) \tag{3.38}$$

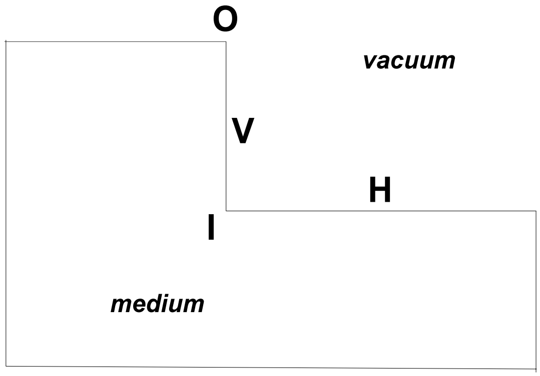

Figure 3.6: *Planar free surface, and the free surface corners. H -horizontal free surface, V -vertical free surface, O -outer corner, I -inner corner. The grid lines are, for instance, the same as in figure 5.39.*

The equations 3.35, 3.36, 3.37, 3.38 are the first-order approximations to the standard equation of the free surface, see e.g. Zahradník,Hron & Moczo (1993).

- outer corner:
  for 3.33:

$$0 + o(t^2) = (-(\lambda + 2\mu)U_x + \mu U_z - \lambda W_z + \mu W_x) + o(h) \quad (3.39)$$

  for 3.34:

$$0 + o(t^2) = (-\mu W_x + (\lambda + 2\mu)W_z - \mu U_z + \lambda U_x) + o(h) \quad (3.40)$$

- inner corner:
  for 3.33:

$$0 + o(t^2) = (-(\lambda + 2\mu)U_x + \mu U_z - \lambda W_z + \mu W_x) + o(h) \quad (3.41)$$

for 3.34:

$$0 + o(t^2) = (-\mu W_x + (\lambda + 2\mu)W_z - \mu U_z + \lambda U_x) + o(h) \qquad (3.42)$$

The equations for the outer and the inner corner are linear combinations of the free-surface conditions for the horizontal and the vertical free surface (equations 3.35, 3.36, 3.37, 3.38) with an equal weight. The approximations for the surface corners are also of the first order of accuracy,are the same for the outer and inner corner.

3.3.6 Stability and accuracy

I For the explicit scheme on a regular square grid, there is a theoretically derived stability condition relating the spatial grid step h and the time step Δt (Virieux, 1986):

$$\Delta t \leq \frac{h}{\sqrt{2} \cdot \alpha_{max}} \,, \qquad (3.43)$$

where α_{max} is the highest velocity in the medium. For the heterogeneous formulation of the explicit scheme of the second-order accuracy we use an empirically found condition.Let

$$h_{min} = min(\Delta x_{min}, \Delta z_{min}) \,,$$

with Δx_{min}, Δz_{min} denoting the minimal grid steps appearing in the irregular grid.
Then the time step is:

$$\Delta t \leq \frac{h_{min}}{c \cdot \alpha_{max}} \,, \qquad (3.44)$$

where $\sqrt{2} \leq c$, usually $1.5 \leq c$.

We found a very important phenomenon: For the model of step-like layer of low velocities (section 5.2.4) on the regular grid ($S1$) with the grid steps $\Delta x = \Delta z = 2.4$ m, and the time step $\Delta t = 0.0005$ s we had $c = 1.600$. After making the grid 5 times denser and, at the same time, and also decreasing the time step 5 times, as it is described for the model $S2$ (thus $\Delta x_{min} = \Delta z_{min} = 0.48$ m, $\Delta t = 0.0001$ rms), there appeared an instability visible in receiver $R2$ (the dashed frame area in figures 5.40, 5.41), however, there still was $c = 1.600$ (see equation 3.44).

After decreasing the time step by 8% to $\Delta t = 0.000092$ s ($c = 1.739$) the solution was stabilized.

The described phenomenon shows, that in case of the irregular grid, it cannot be guaranteed that the constant c empirically found for a certain grid apply also for another grid.

II We also found cases in which the scheme is unconditionally unstable i.e. for Δt according to 3.44. The two cases presented here are shown in figures 3.7, 3.8. Some of the parameters (see figures 3.7, 3.8) are equal to 0 due to geometrical averaging (see equation 3.5), and they yield numerical instability in points denoted by stars. To avoid these numerical problems, our algorithm is automatically modifying the model surface into the shape represented by the highlighted dotted line (figures 3.7, 3.8). The $PSi-2$ is stable after this modification of the model surface, of course, at the same time, the condition 3.44 must be fulfilled.

III To keep numerical dispersion at a reasonably low level (Alford, Kelly & Boore, 1974), we determine the largest possible grid step $\widetilde{\Delta x} = \widetilde{\Delta z} = \tilde{h}$ in every particular area of the model:

$$\tilde{h} = \frac{\tilde{\beta}}{10 \cdot f^*_{max}} \ , \tag{3.45}$$

where f^*_{max} is the frequency of the time function spectrum, at which the absolute value of the spectrum falls below 1% of the maximum spectral value; $\tilde{\beta}$ is the S wave velocity in the area. Thus the chosen grid steps Δx and Δz must fulfill conditions:

$$\Delta x \leq \tilde{h} \; , \tag{3.46}$$

$$\Delta z \leq \tilde{h} \; , \tag{3.47}$$

to avoid the numerical dispersion.

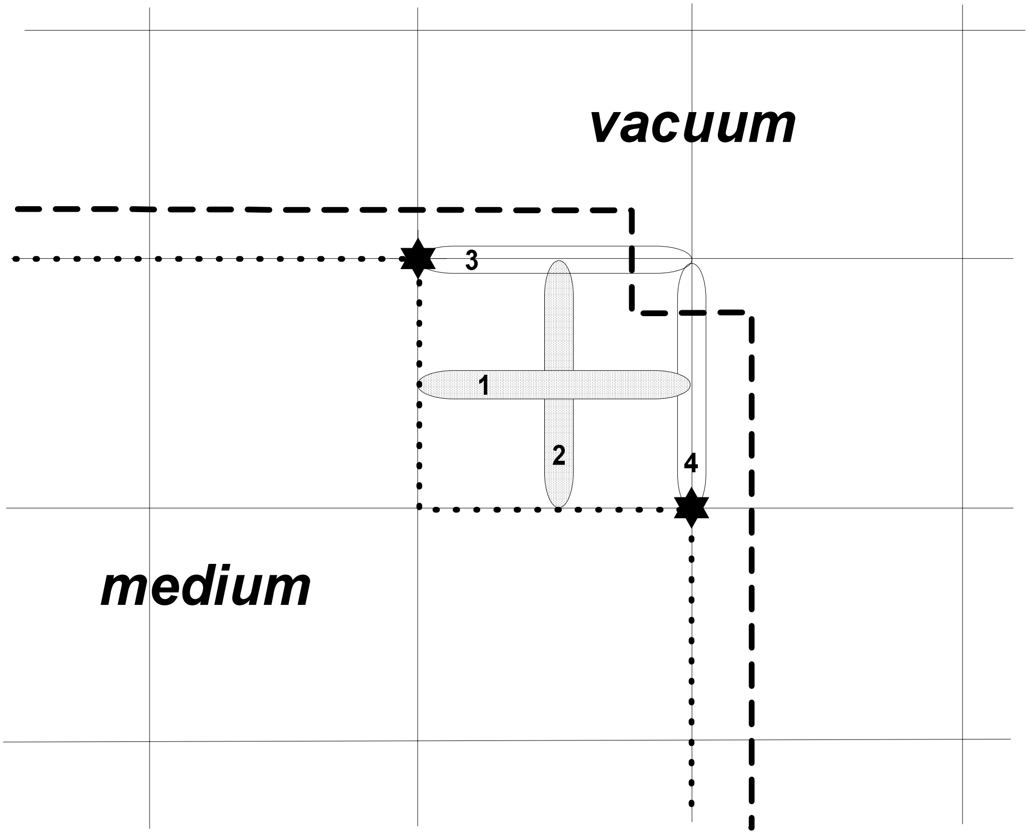

Figure 3.7: *Situation causing instability (described in section 3.3.6, subsection* II*) when computing in grid points denoted by the stars. The highlighted dashed line represents the prescribed planar surface, numbers "1", "2", "3", and "4" denote parameters* a_1*, and* a_2*,* a_3*, and* a_4*, respectively. Here, due to the geometrical averaging (see sections 3.3.6, and 3.2; equation 3.5),* $a_3 = 0$*,* $a_4 = 0$*. The highlighted dotted line represents our free-surface modification with which the* $PSi - 2$ *scheme is stabilized.*

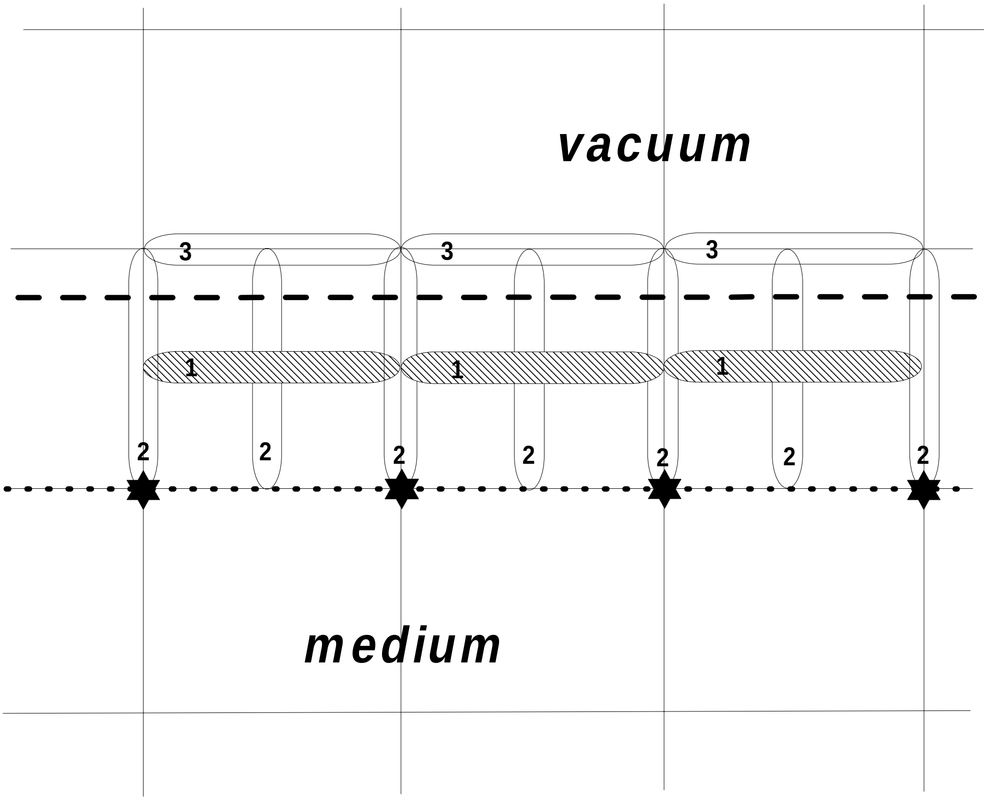

Figure 3.8: *Situation causing instability (described in section 3.3.6, subsection* II*) when computing in grid points denoted by the stars. The highlighted dashed line represents the prescribed surface, numbers "1", "2", and "3" denote parameters* a_1*, and* a_2*,* a_3*, respectively. Here, due to the geometrical averaging (see sections 3.3.6, and 3.2; equation 3.5),* $a_2 = 0$*,* $a_3 = 0$*. The highlighted dotted line represents our free-surface modification with which the* $PSi - 2$ *scheme is stabilized.*

Chapter 4

BOUNDARY CONDITIONS

4.1 Non-reflecting boundaries

To absorb the waves reflected back from the edges of the numerical model, so-called *non-reflecting boundaries* were used (Stacey, 1988).

4.1.1 Equations

Let us consider a homogeneous isotropic medium, adjacent to the non-reflecting boundaries, with α and β the compressional and shear wave velocities, respectively.Then the equations are:

Edges

- bottom:

$$U_{zt} = -\frac{1}{\beta}U_{tt} + \frac{\alpha}{\beta}(\alpha - \beta)W_{xz} + \left(\frac{\alpha^2}{\beta} - \alpha + \frac{1}{2}\beta\right) U_{xx} \qquad (4.1)$$

$$W_{zt} = -\frac{1}{\alpha}W_{tt} + \frac{\beta}{\alpha}(\alpha - \beta)U_{xz} + \left(\frac{\beta^2}{\alpha} - \beta + \frac{1}{2}\alpha\right) W_{xx} \qquad (4.2)$$

- left boundary:

$$W_{xt} = \frac{1}{\beta}W_{tt} - \frac{\alpha}{\beta}(\alpha - \beta)U_{xz} - \left(\frac{\alpha^2}{\beta} - \alpha + \frac{1}{2}\beta\right)W_{zz} \tag{4.3}$$

$$U_{xt} = \frac{1}{\alpha}U_{tt} - \frac{\beta}{\alpha}(\alpha - \beta)W_{xz} - \left(\frac{\beta^2}{\alpha} - \beta + \frac{1}{2}\alpha\right)U_{zz} \tag{4.4}$$

- right boundary:

$$W_{xt} = -\frac{1}{\beta}W_{tt} + \frac{\alpha}{\beta}(\alpha - \beta)U_{xz} + \left(\frac{\alpha^2}{\beta} - \alpha + \frac{1}{2}\beta\right)W_{zz} \tag{4.5}$$

$$U_{xt} = -\frac{1}{\alpha}U_{tt} + \frac{\beta}{\alpha}(\alpha - \beta)W_{xz} + \left(\frac{\beta^2}{\alpha} - \beta + \frac{1}{2}\alpha\right)U_{zz} \tag{4.6}$$

Corners

The Stacey's corners of the model were reported as not always stable (personal discussion with P. Moczo and J. Chroust). Therefore we used the following approximations:

- bottom-right corner:

$$U_t = -\alpha(U_x + U_z) \tag{4.7}$$

$$W_t = -\beta(W_x + W_z) \tag{4.8}$$

- bottom-left corner:

$$U_t = \alpha(U_x - U_z) \tag{4.9}$$

$$W_t = \beta(W_x - W_z) \tag{4.10}$$

- top-left corner:

$$U_t = \alpha(U_x + U_z) \tag{4.11}$$

$$W_t = \beta(W_x + W_z) \tag{4.12}$$

- top-right corner:

$$U_t = \alpha(-U_x + U_z) \tag{4.13}$$

$$W_t = \beta(-W_x + W_z) \tag{4.14}$$

4.1.2 Finite difference formulations

The finite difference approximations to the non-reflecting boundaries are described here, using the stencil as shown in figure 3.3. The stencil point $(0, 0)$ is placed into a particular point of the model. The way in which the lines in the model are actually numbered is shown in figure 4.1.

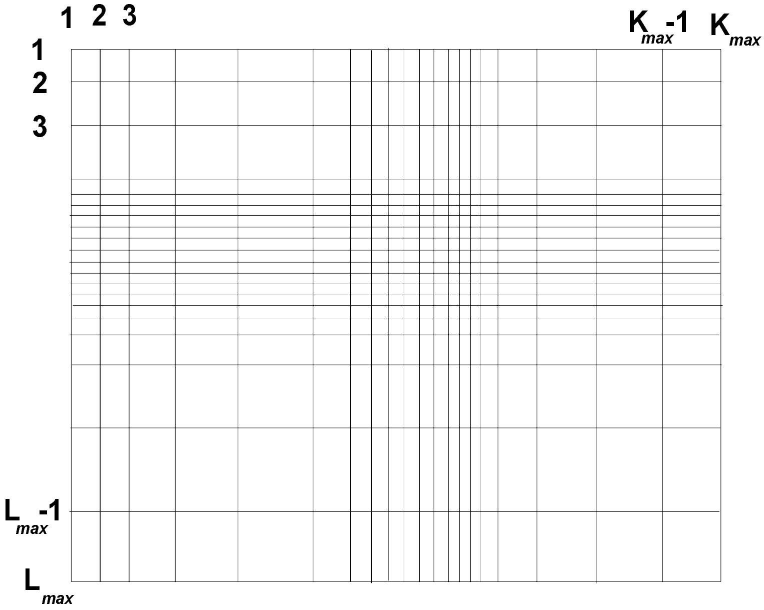

Figure 4.1: *Diagram showing the numbering of the lines in the model with irregular grid.*

The position of the stencils is described by figure 4.2, and it is specified before each application of the *non-reflecting boundary* approximation.

Moreover we define here two horizontal grid lines L_{top}, R_{top} where the line representing the free surface meets the left and the right edges of the model, respectively (see figure 4.3). The following FD approximations are given below for all the edges and the corners of the model, because such detailed equations are usually missing in the literature, in particular for the irregular grid.

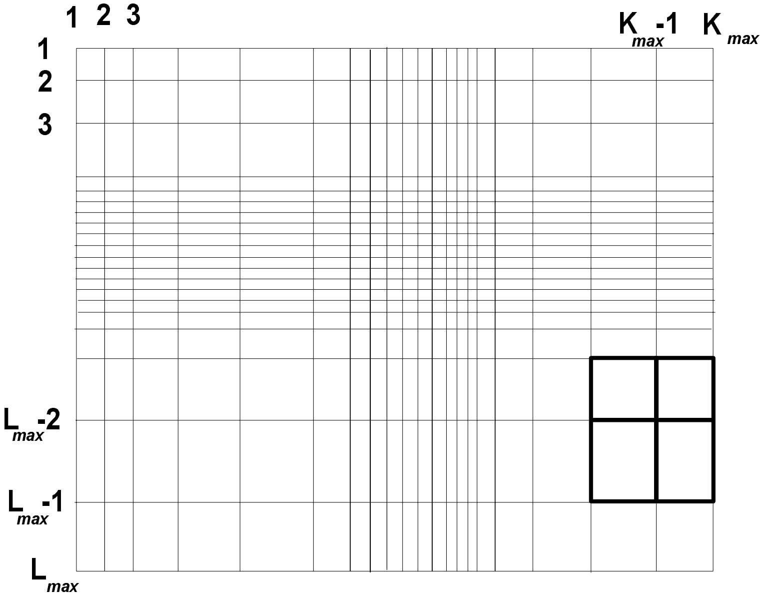

Figure 4.2: *The highlighted frame corresponds to figure 3.2, and its position in this case is at point* $(K_{max}-1, L_{max}-2)$.

Edges

- bottom
  The stencil position is $(k, L_{max}-1)$, where $k \in \{2, K_{max}-1\}$.

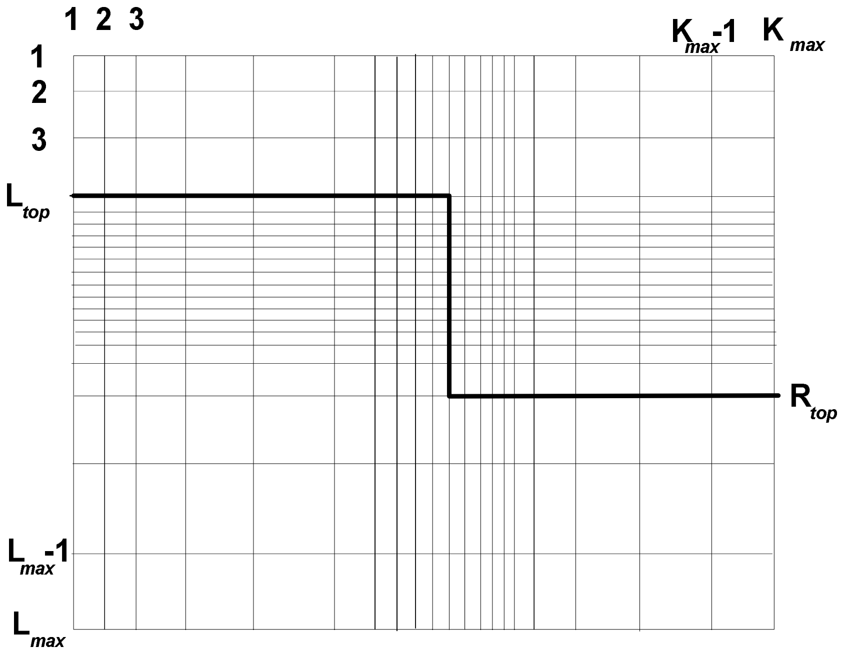

Figure 4.3: *Definition of L_{top}, R_{top} lines; the highlighted line corresponds to the FD approximation of the surface.*

For u component:

$$U_{0,1}^{M+1} = \left(1 + \frac{DZ(0)}{\beta \cdot \Delta t}\right)^{-1} \cdot$$

$$\cdot \left[P1 \cdot DZ(0) \cdot \Delta t - \left(-U_{0,0}^{M+1} - U_{0,1}^{M-1} + U_{0,0}^{M-1}\right) - \right.$$

$$\left. - \frac{DZ(0)}{\beta \cdot \Delta t} \cdot \left(U_{0,0}^{M+1} - 2(U_{0,0}^{M} + U_{0,1}^{M}) + U_{0,0}^{M-1} + U_{0,1}^{M-1}\right)\right] , \quad (4.15)$$

for w component:

$$W_{0,1}^{M+1} = \left(1 + \frac{DZ(0)}{\alpha \cdot \Delta t}\right)^{-1} \cdot$$

$$\cdot \Big[P2 \cdot DZ(0) \cdot \Delta t - \left(-W_{0,0}^{M+1} - W_{0,1}^{M-1} + W_{0,0}^{M-1}\right) -$$

$$-\frac{DZ(0)}{\alpha \cdot \Delta t} \cdot \left(W_{0,0}^{M+1} - 2(W_{0,0}^{M} + W_{0,1}^{M}) + W_{0,0}^{M-1} + W_{0,1}^{M-1}\right)\Big] \ , \tag{4.16}$$

where:

$$P1 = \frac{\alpha}{\beta}(\alpha - \beta) \cdot \widetilde{W}_{zx} + \left(\frac{\alpha^2}{\beta} - \alpha + \frac{1}{2}\beta\right) \cdot \widetilde{U}_{xx} \ ,$$

$$P2 = \frac{\beta}{\alpha}(\alpha - \beta) \cdot \widetilde{U}_{zx} + \left(\frac{\beta^2}{\alpha} - \beta + \frac{1}{2}\alpha\right) \cdot \widetilde{W}_{xx} \ ,$$

$$\widetilde{W}_{zx} = \frac{DX(-1)}{DX(-1) + DX(0)} \cdot$$

$$\cdot \left[\frac{1}{DX(1) \cdot DZ(0)}(W_{1,1}^{M} - W_{1,0}^{M} - W_{0,1}^{M} + W_{0,0}^{M}) - \right.$$

$$\left. -\frac{DX(0)}{(DX(-1))^2 \cdot DZ(0)}(W_{0,1}^{M} - W_{0,0}^{M} - W_{-1,1}^{M} + W_{-1,0}^{M})\right] \ ,$$

$$\widetilde{U}_{zx} = \frac{DX(-1)}{DX(-1) + DX(0)} \cdot$$

$$\cdot \left[\frac{1}{DX(1) \cdot DZ(0)}(U_{1,1}^{M} - U_{1,0}^{M} - U_{0,1}^{M} + U_{0,0}^{M}) - \right.$$

$$\left. -\frac{DX(0)}{(DX(-1))^2 \cdot DZ(0)}(U_{0,1}^{M} - U_{0,0}^{M} - U_{-1,1}^{M} + U_{-1,0}^{M})\right] \ ,$$

$$\begin{gathered}
\widetilde{U}_{xx} = \frac{1}{DX(-1)+DX(0)} \cdot \\
\cdot \left[\frac{U^M_{1,1}+U^M_{1,0}-U^M_{0,1}-U^M_{0,0}}{DX(0)} - \frac{U^M_{0,1}+U^M_{0,0}-U^M_{-1,1}-U^M_{-1,0}}{DX(0)} \right] ,
\end{gathered}$$

$$\begin{gathered}
\widetilde{W}_{xx} = \frac{1}{DX(-1)+DX(0)} \cdot \\
\cdot \left[\frac{W^M_{1,1}+W^M_{1,0}-W^M_{0,1}-W^M_{0,0}}{DX(0)} - \frac{W^M_{0,1}+W^M_{0,0}-W^M_{-1,1}-W^M_{-1,0}}{DX(0)} \right] ,
\end{gathered}$$

and

$$\alpha = \sqrt{\frac{\lambda_\mathrm{s}+2\mu_\mathrm{s}}{\frac{1}{2}(\rho_{0,0}+\rho_{0,1})}} \quad ,$$

$$\beta = \sqrt{\frac{\mu_\mathrm{s}}{\frac{1}{2}(\rho_{0,0}+\rho_{0,1})}} \quad .$$

- left boundary
  The stencil position is $(2,l)$, where $l \in \{L_{top}, L_{max}-1\}$.
  For u component:

$$\begin{gathered}
U^{M+1}_{-1,0} = \left(1+\frac{DX(-1)}{\alpha\cdot\Delta t}\right)^{-1} \cdot \\
\cdot \Big[P2 \cdot DX(-1) \cdot \Delta t - \left(U^{M+1}_{0,0} + U^{M-1}_{-1,0} - U^{M-1}_{0,0} \right) - \\
- \frac{DX(-1)}{\alpha\cdot\Delta t} \cdot \left(U^{M+1}_{0,0} - 2(U^M_{0,0}+U^M_{-1,0}) + U^{M-1}_{0,0} + U^{M-1}_{-1,0} \right) \Big] ,
\end{gathered} \tag{4.17}$$

for w component:

$$W^{M+1}_{-1,0} = \left(1+\frac{DX(-1)}{\beta\cdot\Delta t}\right)^{-1} \cdot$$

$$\cdot\Big[P1\cdot DX(-1)\cdot\Delta t-\Big(W_{0,0}^{M+1}+W_{-1,0}^{M-1}-W_{0,0}^{M-1}\Big)-$$

$$-\frac{DX(-1)}{\alpha\cdot\Delta t}\cdot\Big(W_{0,0}^{M+1}-2(W_{0,0}^{M}+W_{-1,0}^{M})+W_{0,0}^{M-1}+W_{-1,0}^{M-1}\Big)\Big]\ . \tag{4.18}$$

where:

$$P1=\frac{\alpha}{\beta}(\alpha-\beta)\cdot\widetilde{U}_{xz}+\left(\frac{\alpha^2}{\beta}-\alpha+\frac{1}{2}\beta\right)\cdot\widetilde{W}_{zz}\ ,$$

$$P2=\frac{\beta}{\alpha}(\alpha-\beta)\cdot\widetilde{W}_{xz}+\left(\frac{\beta^2}{\alpha}-\beta+\frac{1}{2}\alpha\right)\cdot\widetilde{U}_{zz}\ ,$$

$$\widetilde{U}_{xz}=\frac{DZ(-1)}{DZ(-1)+DZ(0)}\cdot$$

$$\cdot\left[\frac{1}{DZ(0)\cdot DX(-1)}(U_{0,1}^{M}-U_{-1,1}^{M}-U_{0,0}^{M}+U_{-1,0}^{M})-\right.$$

$$\left.-\frac{DZ(0)}{(DZ(-1))^2\cdot DX(-1)}(U_{0,0}^{M}-U_{-1,0}^{M}-U_{0,-1}^{M}+U_{-1,-1}^{M})\right]\ ,$$

$$\widetilde{W}_{xz}=\frac{DZ(-1)}{DZ(-1)+DZ(0)}\cdot$$

$$\cdot\left[\frac{1}{DZ(0)\cdot DX(-1)}(W_{0,1}^{M}-W_{-1,1}^{M}-W_{0,0}^{M}+W_{-1,0}^{M})-\right.$$

$$\left.-\frac{DZ(0)}{(DZ(-1))^2\cdot DX(-1)}(W_{0,0}^{M}-W_{-1,0}^{M}-W_{0,-1}^{M}+W_{-1,-1}^{M})\right]\ ,$$

$$\widetilde{W}_{zz}=\frac{1}{DZ(-1)+DZ(0)}\cdot$$

$$\cdot\left[\frac{W_{0,1}^M + W_{-1,1}^M - W_{0,0}^M - W_{-1,0}^M}{DZ(0)} - \right.$$

$$\left. - \frac{W_{0,0}^M + W_{-1,0}^M - W_{0,-1}^M - W_{-1,-1}^M}{DZ(-1)}\right] ,$$

$$\widetilde{U}_{zz} = \frac{1}{DZ(-1) + DZ(0)} \cdot$$

$$\cdot\left[\frac{U_{0,1}^M + U_{-1,1}^M - U_{0,0}^M - U_{-1,0}^M}{DZ(0)} - \frac{U_{0,0}^M + U_{-1,0}^M - U_{0,-1}^M - U_{-1,-1}^M}{DZ(-1)}\right] ,$$

and

$$\alpha = \sqrt{\frac{\lambda_{\mathrm{e}} + 2\mu_{\mathrm{e}}}{\frac{1}{2}(\rho_{0,0} + \rho_{-1,0})}} \quad ,$$

$$\beta = \sqrt{\frac{\mu_{\mathrm{e}}}{\frac{1}{2}(\rho_{0,0} + \rho_{-1,0})}} \quad .$$

- right boundary
  The stencil position is $(K_{max} - 1, l)$, where $l \in \{R_{top}, L_{max} - 1\}$.
  For u component:

$$U_{1,0}^{M+1} = \left(1 + \frac{DX(0)}{\alpha \cdot \Delta t}\right)^{-1} \cdot$$

$$\cdot \Big[P2 \cdot DX(0) \cdot \Delta t - \left(-U_{0,0}^{M+1} - U_{1,0}^{M-1} + U_{0,0}^{M-1}\right) -$$

$$\left. - \frac{DX(0)}{\alpha \cdot \Delta t} \cdot \left(U_{0,0}^{M+1} - 2(U_{0,0}^M + U_{1,0}^M) + U_{0,0}^{M-1} + U_{1,0}^{M-1}\right)\right] , \quad (4.19)$$

for w component:

$$W_{1,0}^{M+1} = \left(1 + \frac{DX(0)}{\beta \cdot \Delta t}\right)^{-1} \cdot$$

$$\cdot\left[P2\cdot DX(0)\cdot\Delta t-\left(-W_{0,0}^{M+1}-W_{1,0}^{M-1}+W_{0,0}^{M-1}\right)-\right.$$
$$\left.-\frac{DX(0)}{\beta\cdot\Delta t}\cdot\left(W_{0,0}^{M+1}-2(W_{0,0}^{M}+W_{1,0}^{M})+W_{0,0}^{M-1}+W_{1,0}^{M-1}\right)\right]\ , \tag{4.20}$$

where:

$$P1=\frac{\alpha}{\beta}(\alpha-\beta)\cdot\widetilde{U}_{xz}+\left(\frac{\alpha^2}{\beta}-\alpha+\frac{1}{2}\beta\right)\cdot\widetilde{W}_{zz}\ ,$$

$$P2=\frac{\beta}{\alpha}(\alpha-\beta)\cdot\widetilde{W}_{xz}+\left(\frac{\beta^2}{\alpha}-\beta+\frac{1}{2}\alpha\right)\cdot\widetilde{U}_{zz}\ ,$$

$$\widetilde{U}_{xz}=\frac{DZ(-1)}{DZ(-1)+DZ(0)}\cdot$$
$$\cdot\left[\frac{1}{DZ(0)\cdot DX(0)}(U_{1,1}^{M}-U_{0,1}^{M}-U_{1,0}^{M}+U_{0,0}^{M})-\right.$$
$$\left.-\frac{DZ(0)}{(DZ(-1))^2\cdot DX(0)}(U_{1,0}^{M}-U_{0,0}^{M}-U_{1,-1}^{M}+U_{0,-1}^{M})\right]\ ,$$

$$\widetilde{W}_{xz}=\frac{DZ(-1)}{DZ(-1)+DZ(0)}\cdot$$
$$\cdot\left[\frac{1}{DZ(0)\cdot DX(0)}(W_{1,1}^{M}-W_{0,1}^{M}-W_{1,0}^{M}+W_{0,0}^{M})-\right.$$
$$\left.-\frac{DZ(0)}{(DZ(-1))^2\cdot DX(0)}(W_{1,0}^{M}-W_{0,0}^{M}-W_{1,-1}^{M}+W_{0,-1}^{M})\right]\ ,$$

$$\widetilde{U}_{zz}=\frac{1}{DZ(-1)+DZ(0)}\cdot$$

$$\cdot \left[\frac{U^M_{1,1} + U^M_{0,1} - U^M_{1,0} - U^M_{0,0}}{DZ(0)} - \frac{U^M_{1,0} + U^M_{0,0} - U^M_{1,-1} - U^M_{0,-1}}{DZ(-1)} \right] ,$$

$$\widetilde{W}_{zz} = \frac{1}{DZ(-1) + DZ(0)} \cdot$$

$$\cdot \left[\frac{W^M_{1,1} + W^M_{0,1} - W^M_{1,0} - W^M_{0,0}}{DZ(0)} - \frac{W^M_{1,0} + W^M_{0,0} - W^M_{1,-1} - W^M_{0,-1}}{DZ(-1)} \right] ,$$

and

$$\alpha = \sqrt{\frac{\lambda_{\mathrm{w}} + 2\mu_{\mathrm{w}}}{\frac{1}{2}(\rho_{0,0} + \rho_{1,0})}} \quad ,$$

$$\beta = \sqrt{\frac{\mu_{\mathrm{w}}}{\frac{1}{2}(\rho_{0,0} + \rho_{1,0})}} \quad .$$

Corners

- bottom-right corner — the stencil position is $(K_{max} - 1, L_{max} - 1)$.
  U component:

$$U^{M+1}_{1,1} = U^M_{1,1} - \frac{\alpha \Delta t}{2} \cdot \left[\frac{1}{DX(0)} (U^M_{1,1} + U^M_{1,0} - U^M_{0,1} - U^M_{0,0}) + \right.$$
$$\left. + \frac{1}{DZ(0)} (U^M_{1,1} + U^M_{0,1} - U^M_{1,0} - U^M_{0,0}) \right] \quad , \qquad (4.21)$$

  W component:

$$W^{M+1}_{1,1} = W^M_{1,1} - \frac{\beta \Delta t}{2} \cdot \left[\frac{1}{DX(0)} (W^M_{1,1} + W^M_{1,0} - W^M_{0,1} - W^M_{0,0}) + \right.$$
$$\left. + \frac{1}{DZ(0)} (W^M_{1,1} + W^M_{0,1} - W^M_{1,0} - W^M_{0,0}) \right] \quad . \qquad (4.22)$$

  Velocities α, β are:

$$\alpha = \sqrt{\frac{\lambda_{\mathrm{s}} + \lambda_{\mathrm{e}} + 2(\mu_{\mathrm{s}} + \mu_{\mathrm{e}})}{\rho_{0,0} + \rho_{1,1}}} \quad ,$$

$$\beta = \sqrt{\frac{\mu_{\mathrm{s}} + \mu_{\mathrm{e}}}{\rho_{0,0} + \rho_{1,1}}} \quad .$$

- bottom-left corner — the stencil position is $(2, L_{max} - 1)$.
  U component:

$$U^{M+1}_{-1,1} = U^{M}_{-1,1} + \frac{\alpha \Delta t}{2} \cdot \left[\frac{1}{DX(-1)} (U^{M}_{0,1} + U^{M}_{0,0} - U^{M}_{-1,0} - U^{M}_{-1,1}) - \right.$$

$$\left. - \frac{1}{DZ(0)} (U^{M}_{0,1} + U^{M}_{-1,1} - U^{M}_{0,0} - U^{M}_{-1,0}) \right] \quad , \tag{4.23}$$

W component:

$$W^{M+1}_{-1,1} = W^{M}_{-1,1} + \frac{\beta \Delta t}{2} \cdot \left[\frac{1}{DX(-1)} (W^{M}_{0,1} + W^{M}_{0,0} - W^{M}_{-1,0} - W^{M}_{-1,1}) - \right.$$

$$\left. - \frac{1}{DZ(0)} (W^{M}_{0,1} + W^{M}_{-1,1} - W^{M}_{0,0} - W^{M}_{-1,0}) \right] \quad , \tag{4.24}$$

Velocities α, β :

$$\alpha = \sqrt{\frac{\lambda_{\mathrm{s}} + \lambda_{\mathrm{w}} + 2(\mu_{\mathrm{s}} + \mu_{\mathrm{w}})}{\rho_{0,0} + \rho_{-1,1}}} \quad ,$$

$$\beta = \sqrt{\frac{\mu_{\mathrm{s}} + \mu_{\mathrm{w}}}{\rho_{0,0} + \rho_{-1,1}}} \quad .$$

- upper-left corner — the stencil position is $(2, L_{top} + 1)$.
  U component:

$$U^{M+1}_{-1,-1} =$$

$$= U^{M}_{-1,-1} + \frac{\alpha \Delta t}{2} \cdot \left[\frac{1}{DX(-1)} (U^{M}_{0,0} + U^{M}_{0,-1} - U^{M}_{-1,0} - U^{M}_{-1,-1}) + \right.$$

$$\left. + \frac{1}{DZ(-1)} (U^{M}_{0,0} + U^{M}_{-1,0} - U^{M}_{0,-1} - U^{M}_{-1,-1}) \right] \quad , \tag{4.25}$$

W component:

$$W^{M+1}_{-1,-1} =$$

$$= W^M_{-1,-1} + \frac{\beta \Delta t}{2} \cdot \left[\frac{1}{DX(-1)} (W^M_{0,0} + W^M_{0,-1} - W^M_{-1,0} - W^M_{-1,-1}) + \right.$$

$$\left. + \frac{1}{DZ(-1)} (W^M_{0,0} + W^M_{-1,0} - W^M_{0,-1} - W^M_{-1,-1}) \right] \quad , \tag{4.26}$$

Velocities α, β :

$$\alpha = \sqrt{\frac{\lambda_\mathrm{n} + \lambda_\mathrm{w} + 2(\mu_\mathrm{n} + \mu_\mathrm{w})}{\rho_{0,0} + \rho_{-1,-1}}} \quad ,$$

$$\beta = \sqrt{\frac{\mu_\mathrm{n} + \mu_\mathrm{w}}{\rho_{0,0} + \rho_{-1,-1}}} \quad .$$

- upper-right corner — the stencil position is $(K_{max} - 1, R_{top} + 1)$.
  U component:

$$U^{M+1}_{1,-1} = U^M_{1,-1} + \frac{\alpha \Delta t}{2} \cdot \left[-\frac{1}{DX(0)} (U^M_{1,0} + U^M_{1,-1} - U^M_{0,0} - U^M_{0,-1}) + \right.$$

$$\left. + \frac{1}{DZ(-1)} (U^M_{0,0} + U^M_{1,0} - U^M_{1,-1} - U^M_{0,-1}) \right] \quad , \tag{4.27}$$

W component:

$$W^{M+1}_{1,-1} = W^M_{1,-1} + \frac{\beta \Delta t}{2} \cdot \left[-\frac{1}{DX(0)} (W^M_{1,0} + W^M_{1,-1} - W^M_{0,0} - W^M_{0,-1}) + \right.$$

$$\left. + \frac{1}{DZ(-1)} (W^M_{0,0} + W^M_{1,0} - W^M_{1,-1} - W^M_{0,-1}) \right] \quad , \tag{4.28}$$

Velocities α, β :

$$\alpha = \sqrt{\frac{\lambda_\mathrm{n} + \lambda_\mathrm{e} + 2(\mu_\mathrm{n} + \mu_\mathrm{e})}{\rho_{0,0} + \rho_{1,-1}}} \quad ,$$

$$\beta = \sqrt{\frac{\mu_\mathrm{n} + \mu_\mathrm{e}}{\rho_{0,0} + \rho_{1,-1}}} \quad .$$

4.2 Tapers

Because even Stacey's conditions do not completely eliminate the boundary reflections, in particular for complicated scattered wavefields, we use an additional method to dump the reflections. It is a taper introduced by Cerjan *et al* (1985) realized artificially by decreasing both the displacement components in a "strip" 40 grid points wide adjacent to the edges of the model.

4.3 Reflecting boundaries

For special cases of symmetrical structures it is very useful to compute just one half of the model, while the other is supplied by a symmetry condition in which the symmetry boundary is perfectly reflecting. The following conditions describe the horizontal and vertical components of the displacement along the vertical symmetry line placed at x_0:

- for the source of P waves (antisymmetry in u, symmetry in w):

$$u|_{x_0,z} = 0 \tag{4.29}$$

$$\left.\frac{\partial w}{\partial x}\right|_{x_0,z} = 0 \tag{4.30}$$

- for the source of S waves (symmetry in u, antisymmetry in w):

$$\left.\frac{\partial u}{\partial x}\right|_{x_0,z} = 0 \tag{4.31}$$

$$w|_{x_0,z} = 0 \tag{4.32}$$

By the source we understand a line source placed in (x_0, z_0). It is a center of compression (for P waves), or a centre of rotation (for S waves).

Conditions 4.29 and 4.30 can also se used in case of a vertical body force, and for the incident P wave. The use of 4.31 and 4.32 is similar: A horizontal body force, and an incident S wave.

4.3.1 Finite difference formulations

Let us consider the conditions of symmetry along a vertical grid line, and the grid line $k = K_{sym}$. In that case the stencil position is (K_{sym}, l), where $l \in \{2, L_{max} - 1\}$.
Moreover, let $DX(-1) = DX(0)$. Then:

- antisymmetry in u, symmetry in w:
  from 4.29, 4.30 we get (respectively):

$$U^M_{1,0} = -U^M_{-1,0} \; , \tag{4.33}$$

$$W^M_{1,0} = W^M_{-1,0} \; , \tag{4.34}$$

- symmetry in u, antisymmetry in w:
  from 4.31, 4.32 we get (respectively):

$$U^M_{1,0} = U^M_{-1,0} \; , \tag{4.35}$$

$$W^M_{1,0} = -W^M_{-1,0} \; . \tag{4.36}$$

Chapter 5

NUMERICAL EXPERIMENTS

5.1 Plane free surface

We investigate three models here. The results retrieved from the *finite-difference* (FD) scheme, developed in this thesis, were compared with the FD method using$PSi - 2$ scheme for the regular grid, and with the *spectral-element* method ($SPEM$) of E.Priolo (Zahradník & Priolo, 1995). The $SPEM$ method is the reference method, because it has high accuracy due to higher-order approximation. All the three models have a planar surface, with a line source applied near the surface. The source is realized by a vertical body force, whose time history is as follows:

$$f(t) = -exp(b) \cdot f_{max} \cdot [f_{max} \cdot (t - t_0) \cdot \cos c + \pi \cdot \sin c] \tag{5.1}$$

$$b = -\frac{1}{2} \cdot f_{max}^2 \cdot (t - t_0)^2 \quad ,$$

$$c = \pi \cdot f_{max} \cdot (t - t_0) \quad ,$$

with $t_0 = 0.136$ s,
and the maximum frequency $f_{max} = 22$ Hz.

5.1.1 Homogeneous half-space

The model is described by figure 5.1 and table 5.1. The source is denoted by S, and the receivers by $R1, R2, R3$, respectively.
The grid lines were numbered as shown in figure 4.1. The source is placed on vertical line $k = 2$ which, at the same time, represents "the plane of symmetry". It is the symmetry in the w component (equation 4.30), and the antisymmetry in the u component (equation 4.29). The time window for the time function is 0.408 s, and for the computation is 2 seconds. Along the bottom and the right side of the model the non-reflecting boundary condition is applied, and also the taper of 40 points, as described in 4.2. The model has the regular grid, with constant grid steps $\Delta x = \Delta z = 4.0$ m.

The results are displayed in figures 5.1, 5.2, 5.3, where they are compared with the $SPEM$ method, and with the analytical solution. The relative normalizing factors are given in table 5.1.1 The results show a very close agreement of our solution compared with the two others.

Table 5.1: *The meaning of the variables is as follows:* α_I, β_I *- P, S wave velocities* (m/s)*;* ρ_I *-density* (kg/m^3)*;* f^*_{max} *-the frequency* (Hz) *at which the absolute value of the spectrum is* 1% *of the maximum spectral value;* Δt *-time step* (s)*;* $\Delta x, \Delta z$ *-grid steps* (m)*;* N_t *-number of time steps;* K, L *-number of vertical and horizontal lines in the model*

α_I	β_I	ρ_I	f^*_{max}
2000	1155	1000	22

Δt	Δx	Δz	N_t	K	L
0.001	4.0	4.0	2000	512	242

Table 5.2: *Relative normalizing factors:* n_{R1u} *is the relative normalizing factor for u component in receiver R1, and analogously for the other receivers and component*

method	n_{R1u}	n_{R2u}	n_{R2u}	n_{R1w}	n_{R2w}	n_{R2w}
$PSi-2$	0.685	0.636	0.136	0.973	1.00	0.632
$SPEM$	0.710	0.634	0.134	0.986	1.00	0.593
analytical	0.688	0.633	0.133	0.983	1.00	0.599

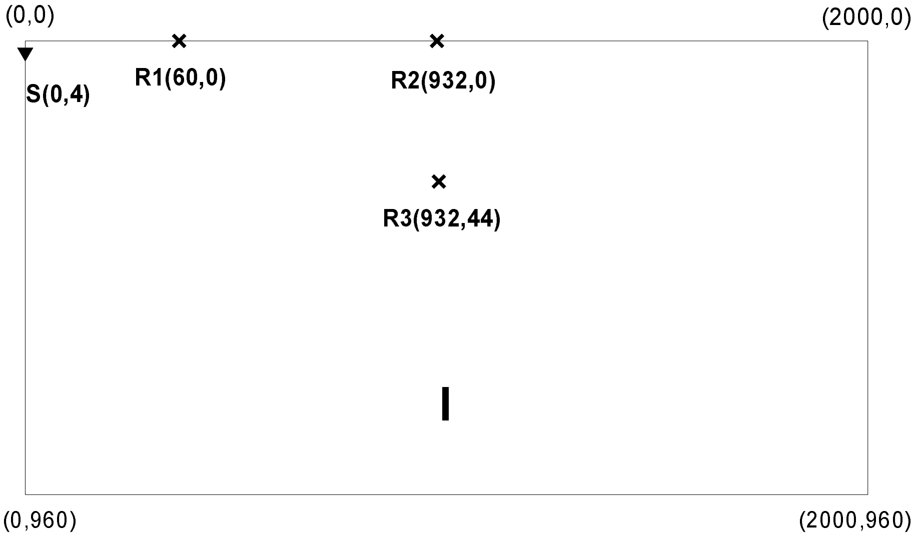

Figure 5.1: *The homogeneous half-space model (coordinates in metres).*

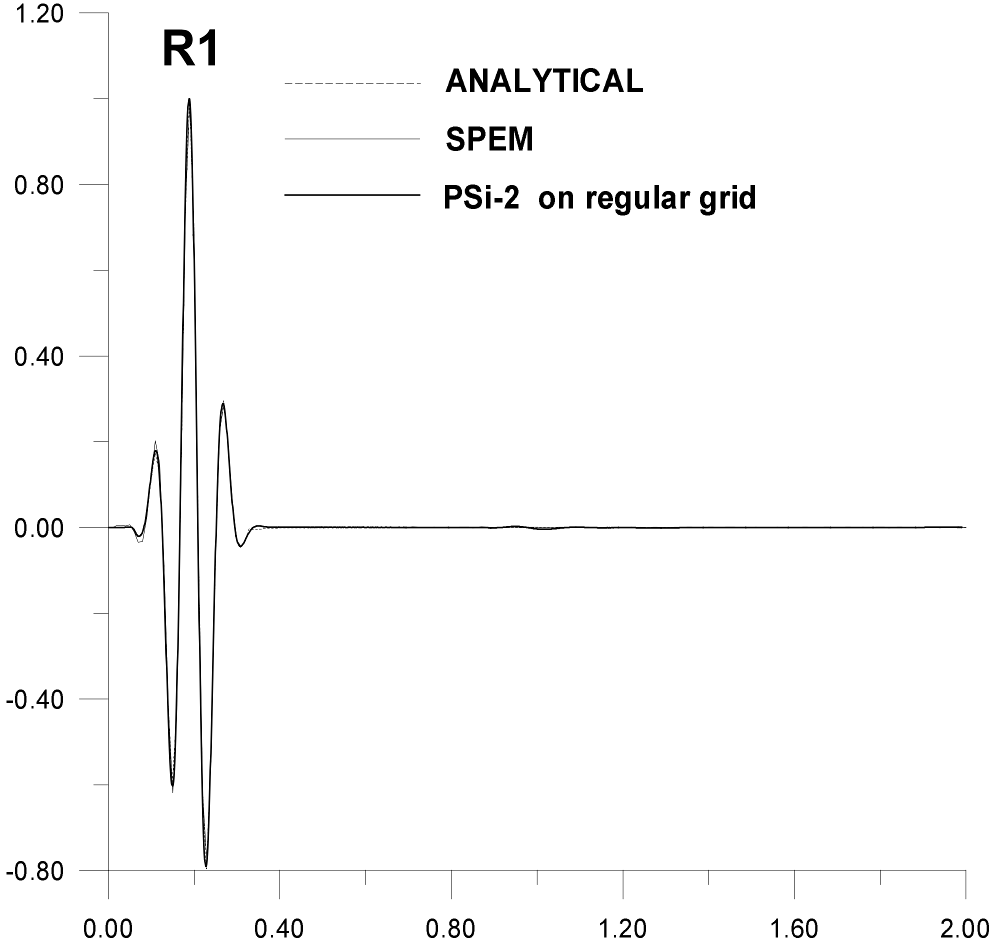

Figure 5.2: *Normalized seismograms for w component in receiver R1.*

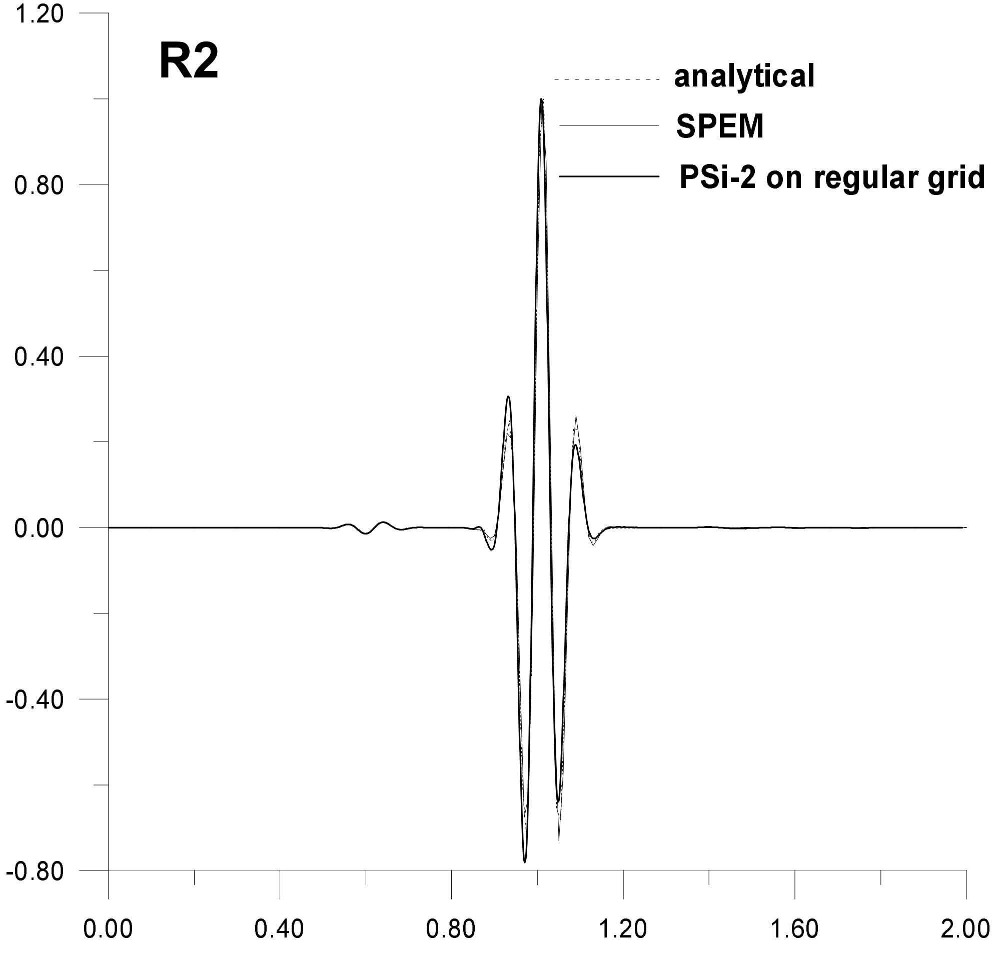

Figure 5.3: *Normalized seismograms for w component in receiver R2.*

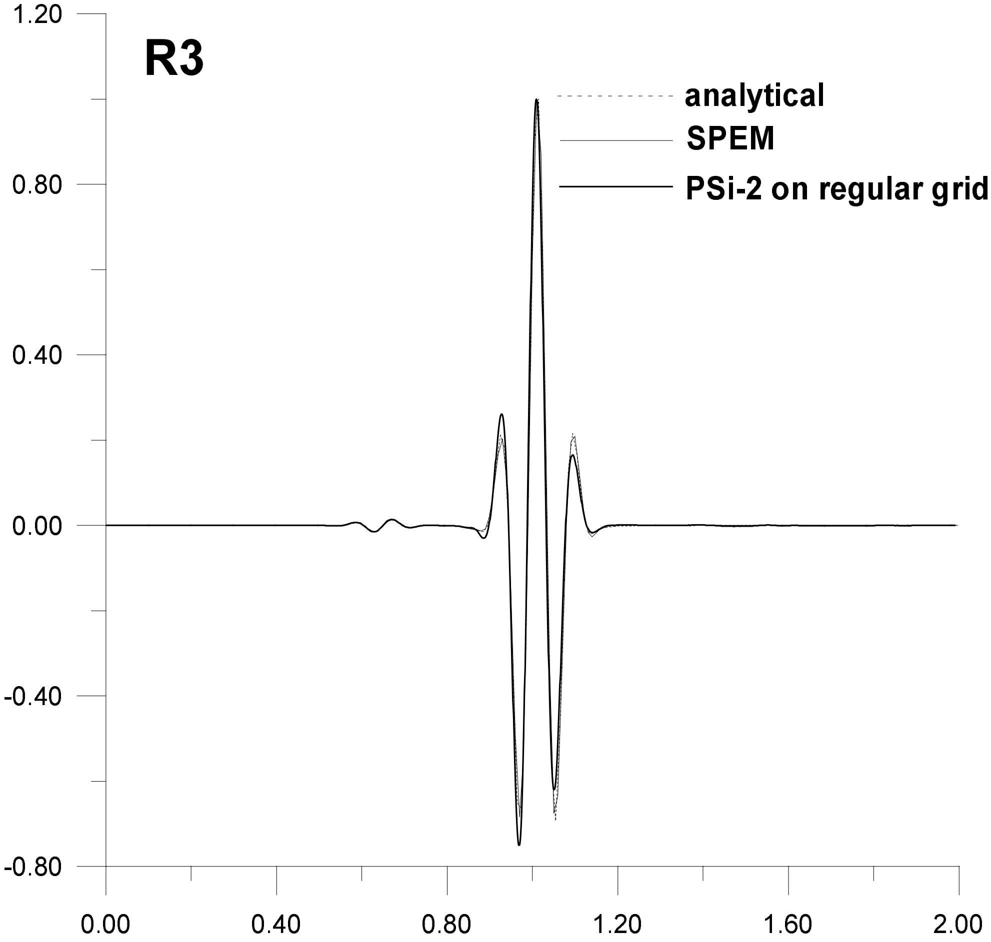

Figure 5.4: *Normalized seismograms for w component in receiver R3.*

5.1.2 Two quarter-spaces

Model with regular grid

This is a two quarter-spaces model (see figure 5.5 and table 5.3). It is a model with a regular grid and with constant grid steps $\Delta x = \Delta z = 4.0$ m. Our results are compared with *SPEM* in figures 5.6, 5.7, 5.8 and in table 5.1.2.

Table 5.3: *The meaning of the variables is:* α_I, β_I *- P, S wave velocities* (m/s) *in block I;* ρ_I *-density* (kg/m^3) *in block I;* α_{II}, β_{II} *-analogous for block II;* f^*_{max} *-the frequency* (Hz) *at which the absolute value of the spectrum is* 1% *of the maximum spectral value;* Δt *-time step* (s)*;* $\Delta x, \Delta z$ *-grid steps* (m)*;* N_t *-number of time steps;* K, L *-number of vertical and horizontal lines in the model*

α_I	β_I	ρ_I	α_{II}	β_{II}	ρ_{II}
2000	1155	1000	3000	1732	2000

f^*_{max}	Δt	Δx	Δz (m)	N_t	K	L
22	0.0005	4.0	4.0	4000	512	242

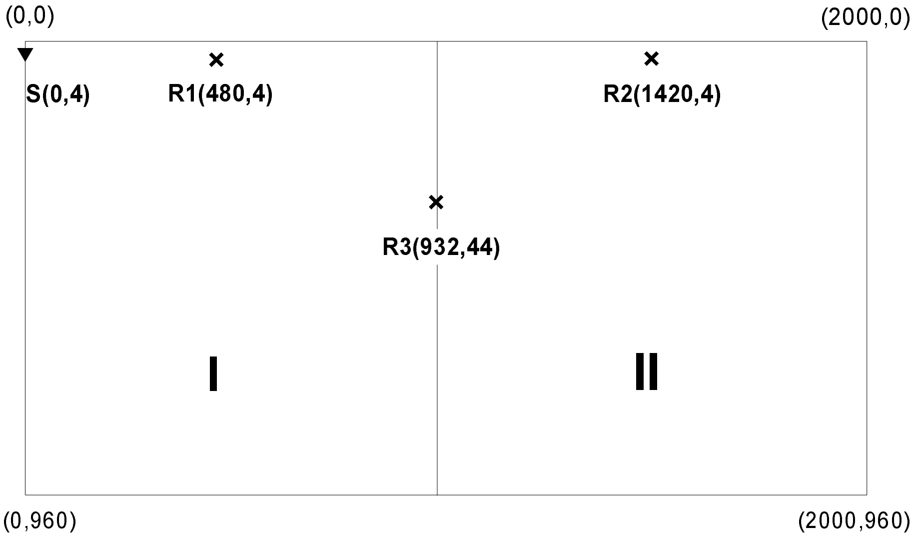

Figure 5.5: *Two quarter-spaces (coordinates in metres).*

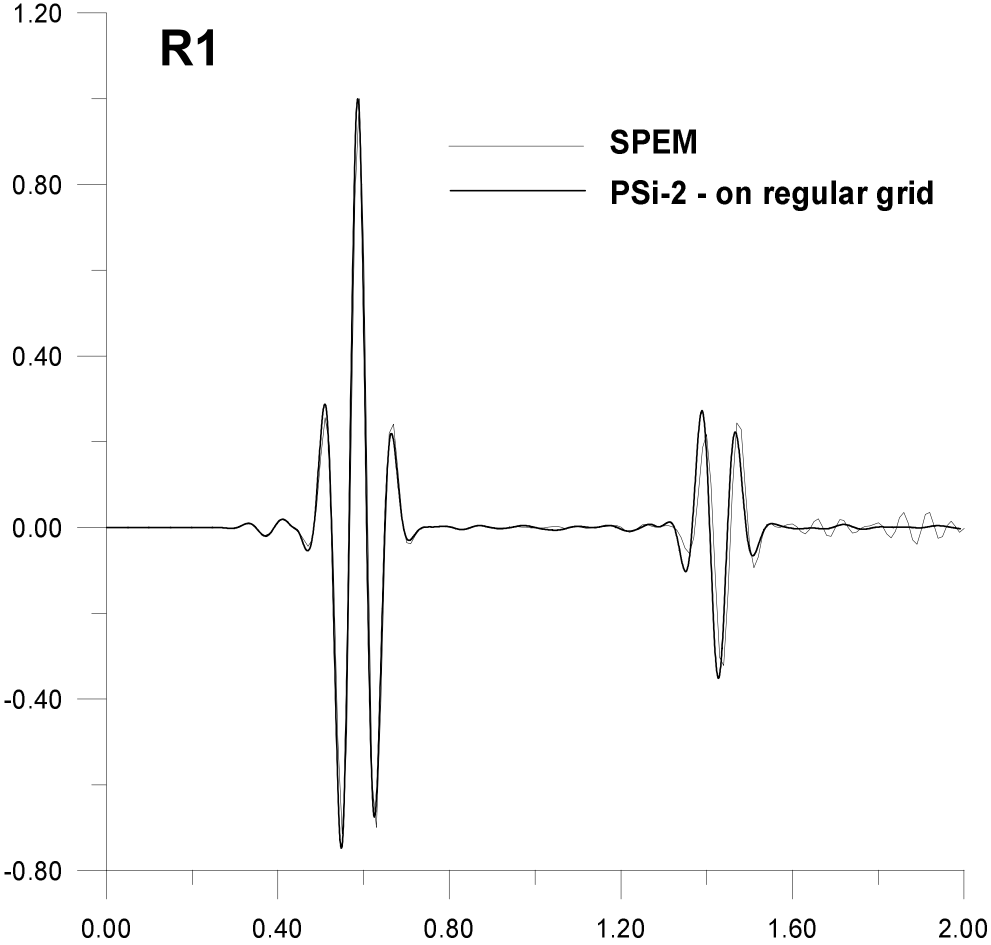

Figure 5.6: *Seismograms for w component in receiver R1 for two quarter-spaces model with a regular grid.*

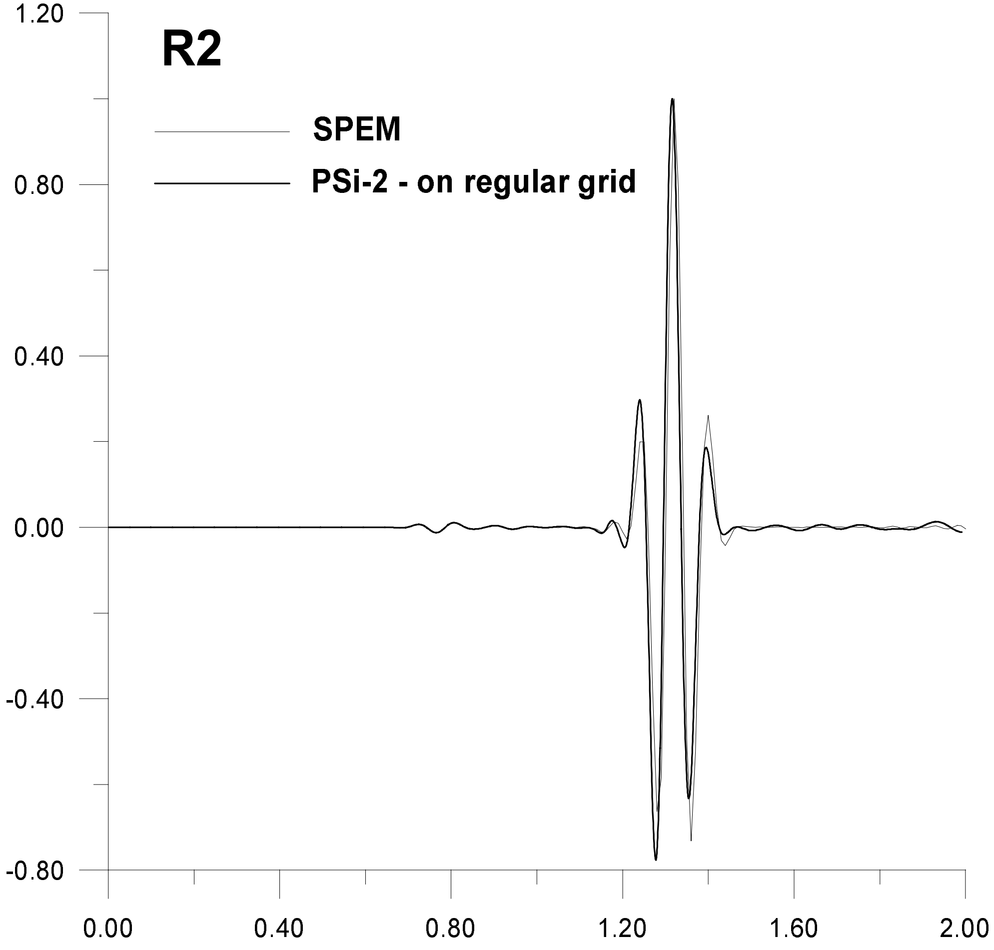

Figure 5.7: *Seismograms for w component in receiver R2 for two quarter-spaces model with a regular grid.*

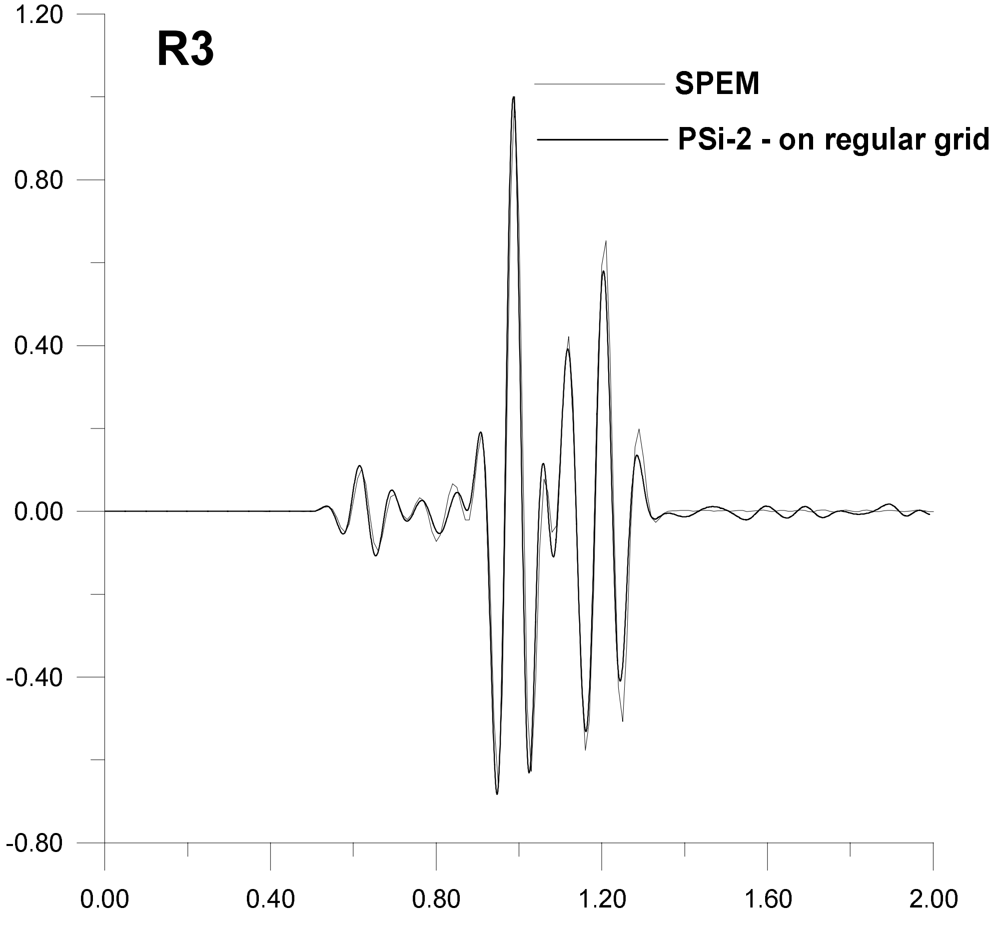

Figure 5.8: *Seismograms for w component in receiver R3 for two quarter-spaces model with a regular grid.*

Model with irregular grid

This two quarter-spaces model has an irregular grid as shown in figure 5.9. It is realized in the following way: the first 10 grid steps between horizontal lines $l = 1$, and $l = 11$ are of $\Delta z = 0.8$ m. Then, between grid lines $l = 11$ and $l = L_{max}$ the grid steps are of $\Delta z = 4.0$ m. Similarly for the vertical lines (figure 5.9): The grid steps are $\Delta x = 4.0$ m between grid lines $k = 1$ and $k = 252$, then $\Delta x = 0.8$ m between grid lines $k = 252$ and $k = 267$, and finally $\Delta x = 4.0$ m between grid lines $k = 267$ and $k = K_{max}$. The interface is lying exactly in the middle between vertical lines $k = 259$, and $k = 260$.

The parameters of the model are shown in table 5.4

Table 5.4: *The meaning of the variables is:* α_I, β_I *- P, S wave velocities* (m/s) *in block I;* ρ_I *-density* (kg/m^3) *in block I;* α_{II}, β_{II} *-analogous for block II;* f^*_{max} *-the frequency* (Hz) *at which the absolute value of the spectrum is* 1% *of the maximum spectral value;* Δt *-time step* (s)*;* $\Delta x_{min}, \Delta z_{min}, \Delta x_{min}, \Delta z_{min}$ *are the minimum and the maximum grid steps* (m) *appearing in the model;* N_t *-number of time steps;* K, L *-number of vertical and horizontal lines in the model*

α_I	β_I	ρ_I	α_{II}	β_{II}	ρ_{II}	f^*_{max}
2000	1155	1000	3000	1732	2000	22

Δt	Δx_{min}	Δz_{min}	Δx_{max}	Δz_{max}	N_t	K	L
0.0001	0.8	0.8	4.0	4.0	4000	512	350

Because the Fortran optimizer (for unknown reasons) didn't compile the subroutine for the *non-reflecting boundary* in this particular model, the bottom and the right-hand side of the model were prescribed as perfectly reflecting boundaries. To avoid the reflections arriving at the receivers during the time window selected for the comparison with the $SPEM$, the model was extended downwards and to the right, with grid steps of 4.0 m in both directions, while the left-hand side was treated by the symmetry conditions as in the model of the two quarter spaces on a regular grid. The time window and the window for time function is exactly the same as in the case of the regular grid.

The results are compared with the $SPEM$ method in figures 5.10, 5.11, 5.12. In certain parts of the seismograms we can see an improvement, i.e. the FD results become closer to the $SPEM$ results than in case of the regular grid. The points of the most significant improvements are specified by arrows. Table 5.1.2 shows the comparison of the normalizing factors n_R.

Table 5.5: *Relative normalizing factors* n_R *as in table 5.1.1*

method	n_{R1u}	n_{R2u}	n_{R2u}	n_{R1w}	n_{R2w}	n_{R2w}
$PSi-2$ $_{regular\ grid}$	0.385	0.174	0.0565	1.00	0.373	0.0676
$PSi-2$ $_{irregular\ grid}$	0.337	0.170	0.0620	1.00	0.373	0.0662
$SPEM$	0.380	0.171	0.0612	1.00	0.373	0.0592

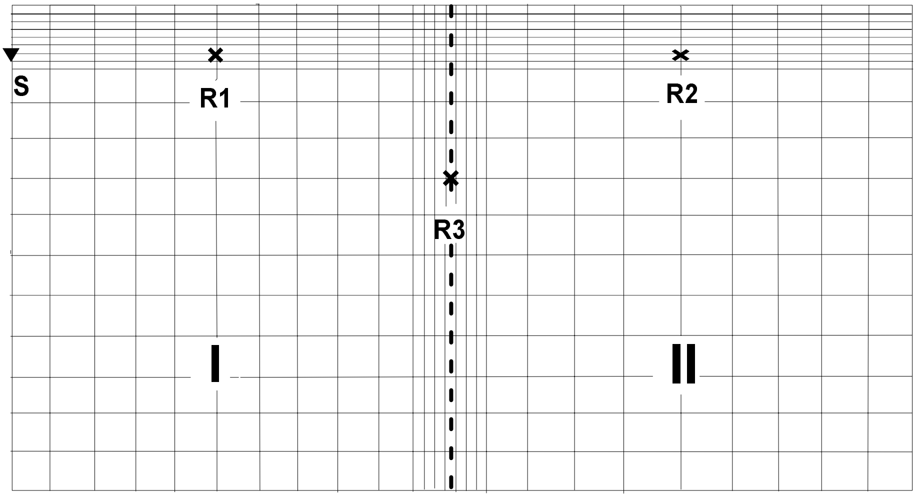

Figure 5.9: *The model of two quarter-spaces with irregular grid, which is denser along the interface and the surface. The highlighted dashed line is the interface.*

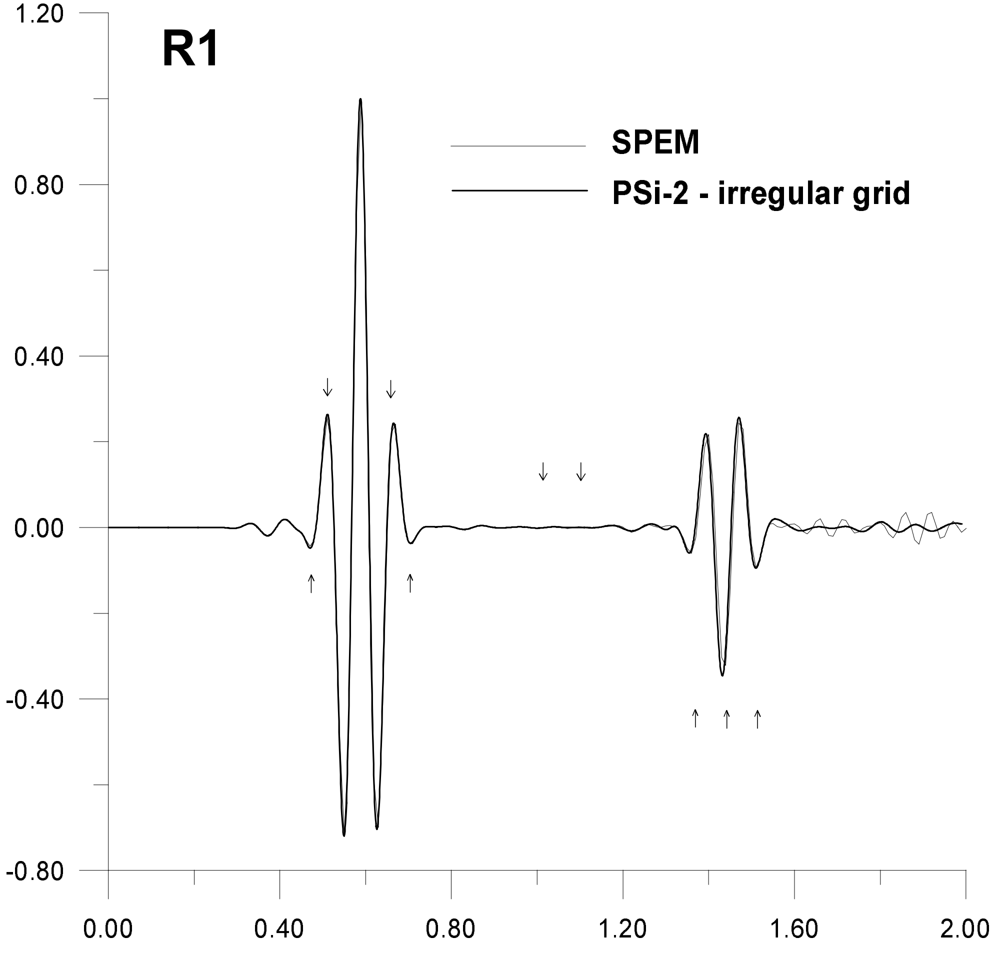

Figure 5.10: *Seismograms for w component in receiver R1 for two quarter-spaces model with irregular grid.*

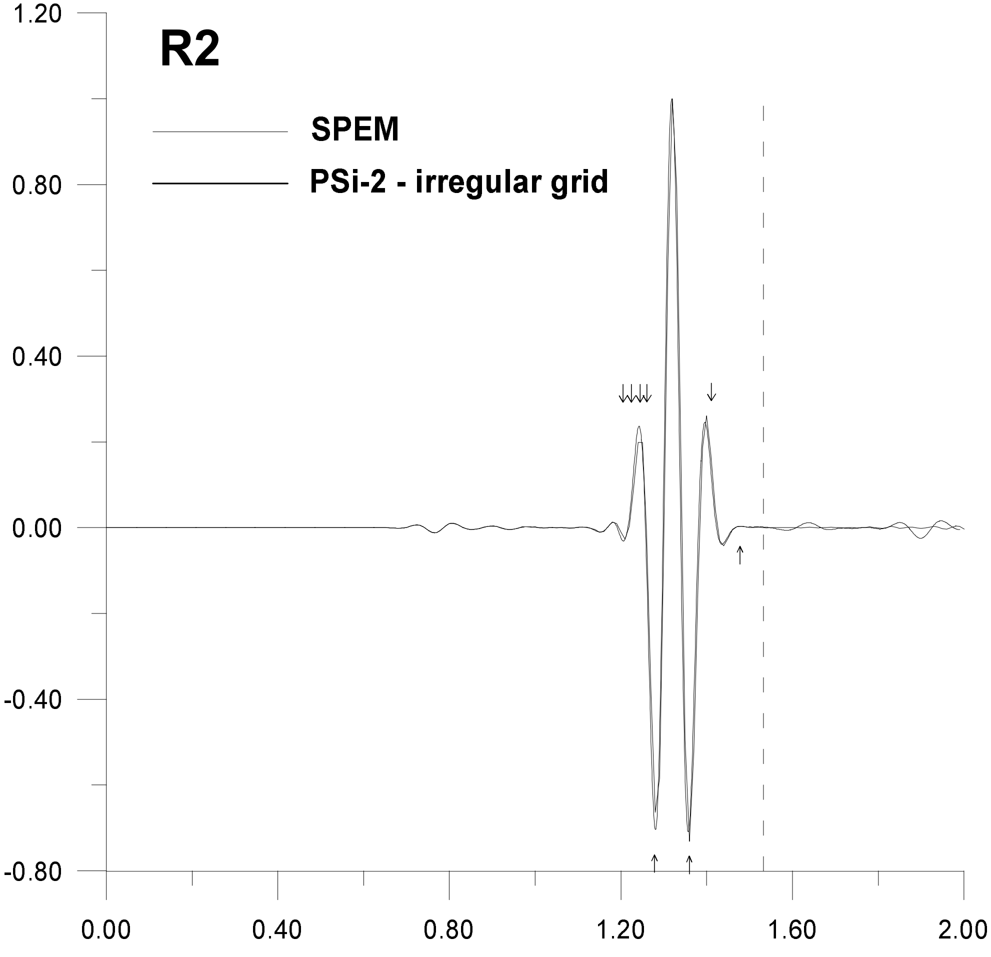

Figure 5.11: *Seismograms for w component in receiver R2 for two quarter-spaces model with a irregular grid.*

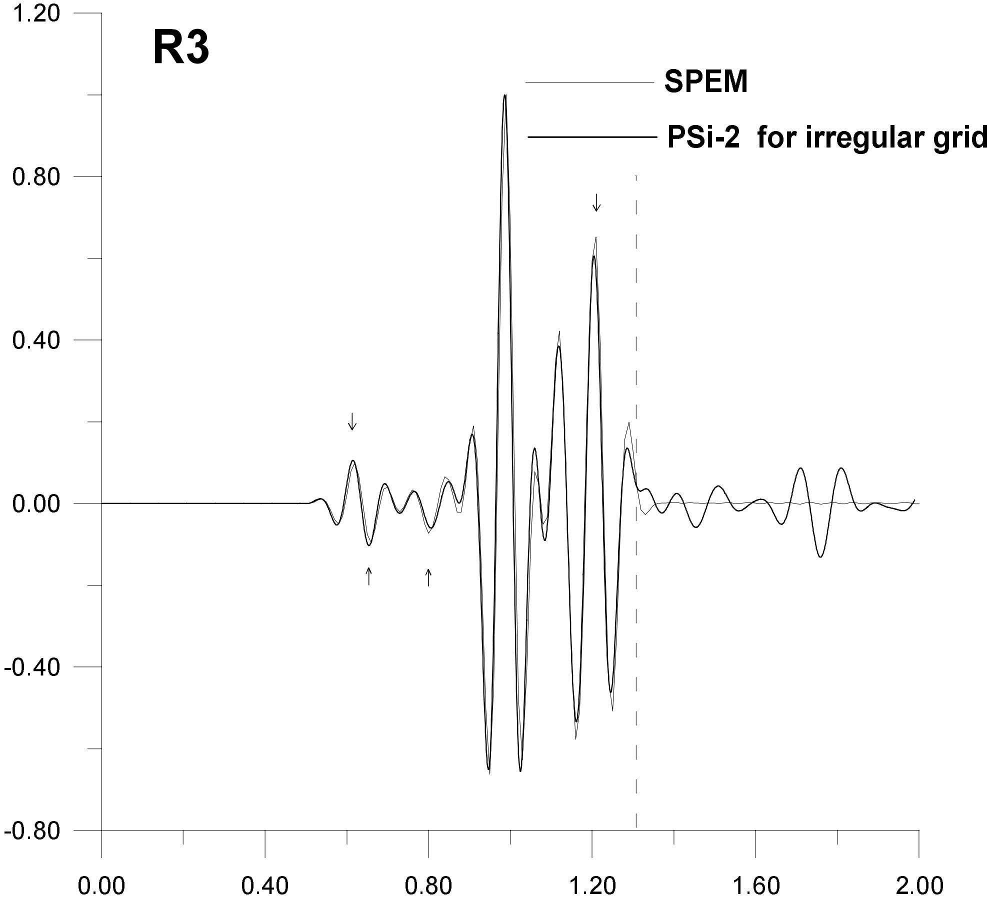

Figure 5.12: *Seismograms for w component in receiver R3 for two quarter-spaces model with irregular grid. The vertical dashed line separates the time without(left) and with(right) reflections from the edges of the model.*

5.1.3 Low-velocity layer

Model with regular grid

This model is set as it is shown by figure 5.13. It is on a regular grid with the same grid steps $\Delta x = \Delta z = 4.0$ m in both directions. The interface is lying between horizontal lines $l = 31$ and $l = 32$, closer to $l = 32$ ("$l = 31.75$"). This model has a symmetry along the left hand side, and Stacey's boundaries with tapers along the bottom and the right-hand edge. The results compared with $SPEM$ are at figures 5.14, 5.15, 5.16. The parameters are in table 5.6.

Table 5.6: *The meaning of the variables are the same as in table 5.3*

α_I	β_I	ρ_I	α_{II}	β_{II}	ρ_{II}	f^*_{max}
2000	1155	1000	3000	1732	2000	22

Δt	Δx	Δz	N_t	K	L
0.0005	4.0 m	4.0 m	4000	512	242

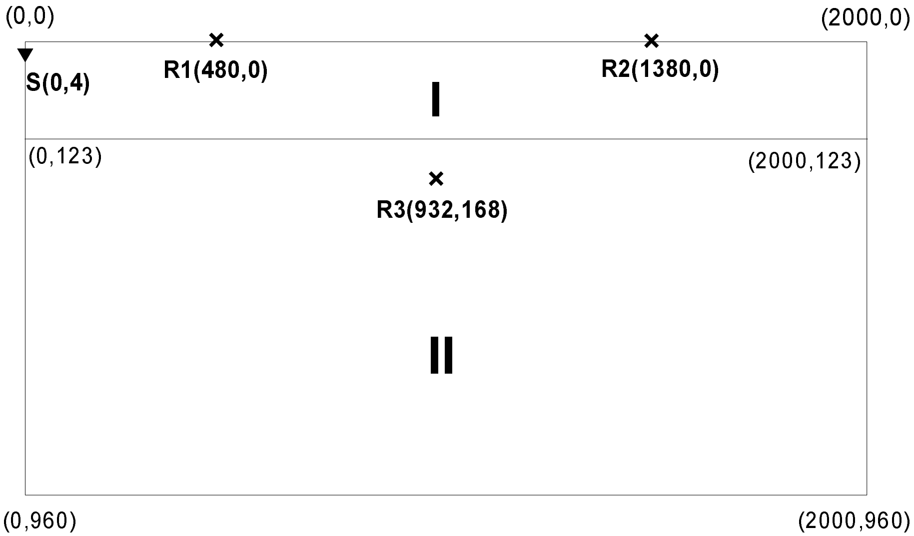

Figure 5.13: *Low-velocity layer (coordinates in metres).*

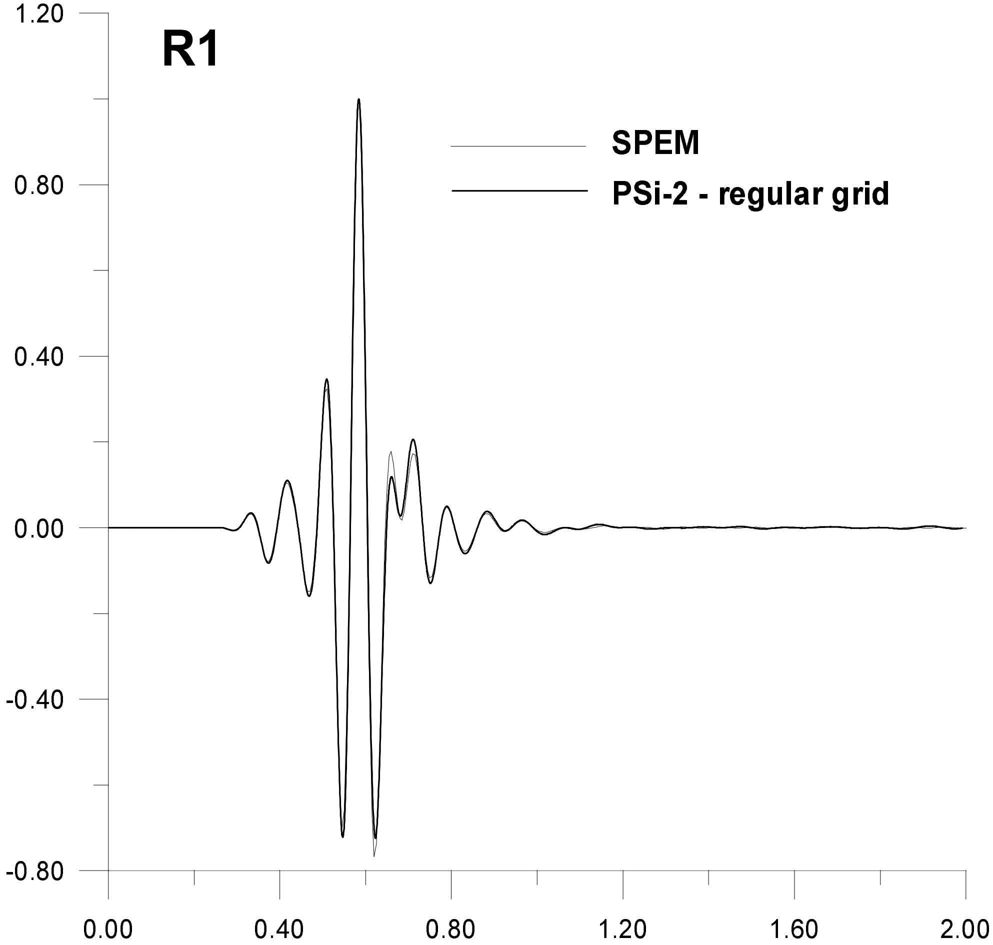

Figure 5.14: *Seismograms for w component in receiver R1 for low-velocity layer model with a regular grid. The vertical dashed line separates the time without(left) and with(right) reflections from the edges of the model.*

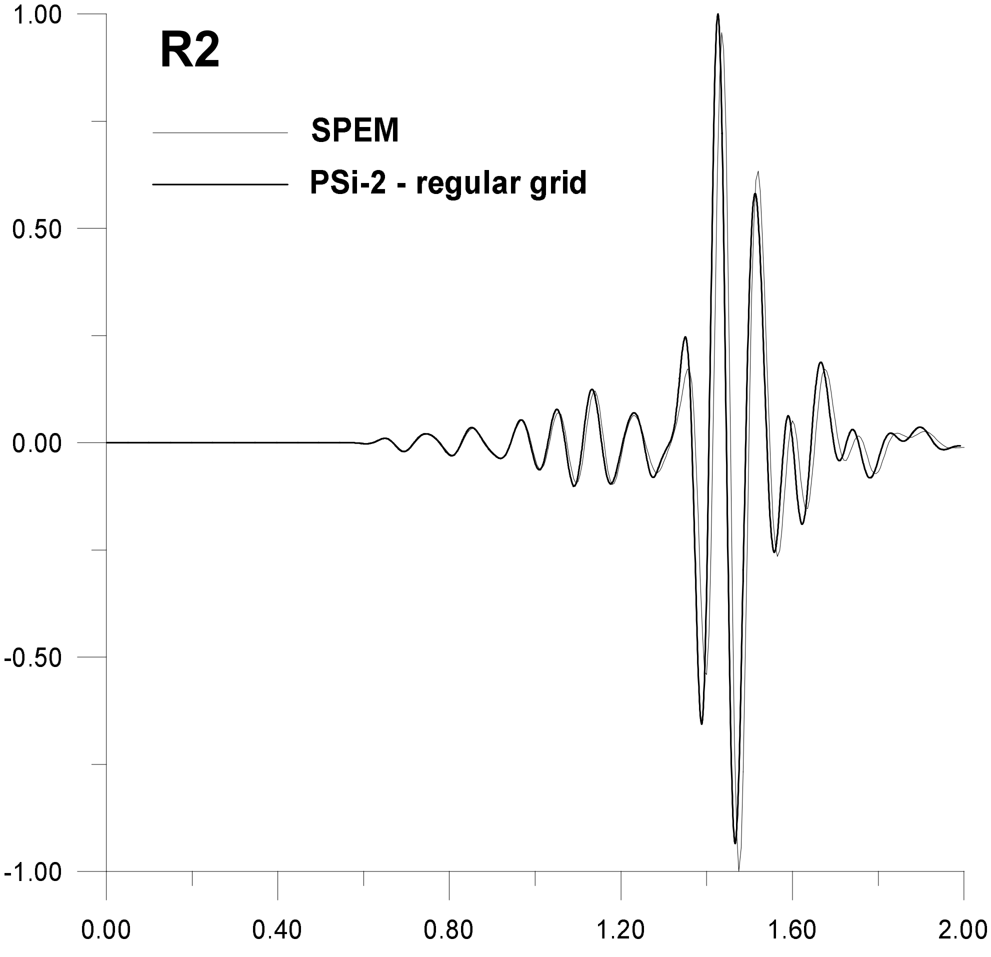

Figure 5.15: *Seismograms for w component in receiver R2 for low-velocity layer model with a regular grid.*

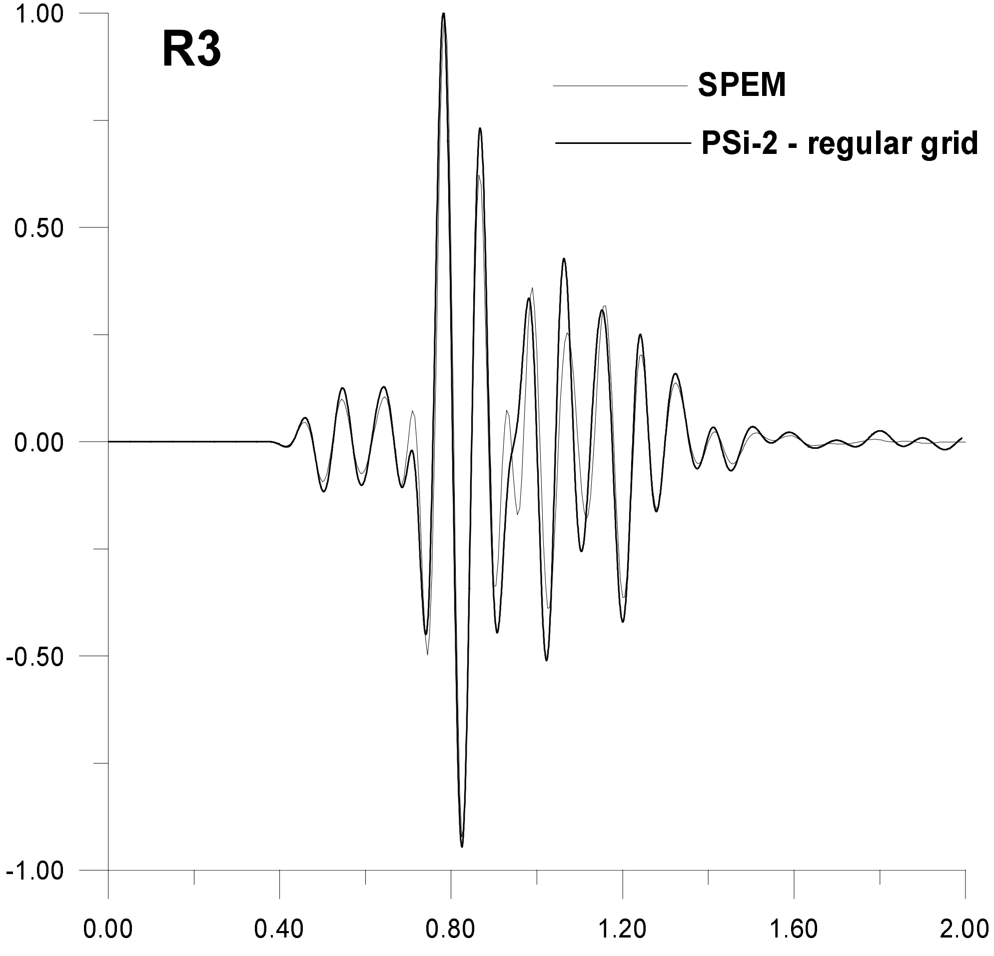

Figure 5.16: *Seismograms for w component in receiver R3 for low-velocity layer model with a regular grid.*

Model with irregular grid

This model of the low-velocity layer was tested on the irregular grid as shown in figure 5.17: The grid step $\Delta x = 4.0$ m applies for the whole model. The first 308 grid steps between the horizontal lines $l = 1$ and $l = 309$ are of $\Delta z = 0.4$ m. The interface is lying exactly in the middle of the grid step between grid lines $l = 308$ and $l = 309$. The grid steps between horizontal grid lines $l = 309$ and $l = L_{max}$ are $\Delta z = 4.0$ m.

Thus the grid step is abruptly increased by 1 : 10 at horizontal grid line $l = 309$. The parameters of the model are in table 5.7

Table 5.7: *The meaning of the variables is the same as in table 5.4*

α_I	β_I	ρ_I	α_{II}	β_{II}	ρ_{II}	f^*_{max}
2000	1155	1000	3000	1732	2000	22

Δt	Δx_{min}	Δz_{min}	Δx_{max}	Δz_{max}	N_t	K	L
0.0001	4.0	0.4	4.0	4.0	4000	512	519

Table 5.8: *Relative normalizing factors n_R as in table 5.1.1*

method	n_{R1u}	n_{R2u}	n_{R2u}	n_{R1w}	n_{R2w}	n_{R2w}
$PSi-2$ *regular grid*	0.596	0.648	0.0198	1.00	0.944	0.0504
$PSi-2$ *irregular grid*	0.601	0.665	0.0187	1.00	0.932	0.0571
$SPEM$	0.602	0.679	0.0195	1.00	0.944	0.0645

The results of the computation are compared with $SPEM$ in figures 5.18, 5.19, 5.20. Moreover, we computed the same model, but with a grid that is denser just 5 grid lines along the interface (on both sides), and 5 grid lines along the surface, again with the grid step contrast 1 : 10, analogous to the vertical interface in the two quarter-spaces model on the irregular grid. The results, not shown here, almost identical to the ones presented, are not disturbed by any of the reflections from the bottom and the right-hand side of the model until the time indicated in the figures by the dashed vertical line.

The improvement, in comparison to the same model on the regular grid, is quite significant now, as proved by a very close agreement with the *SPEM* (see also 5.8).

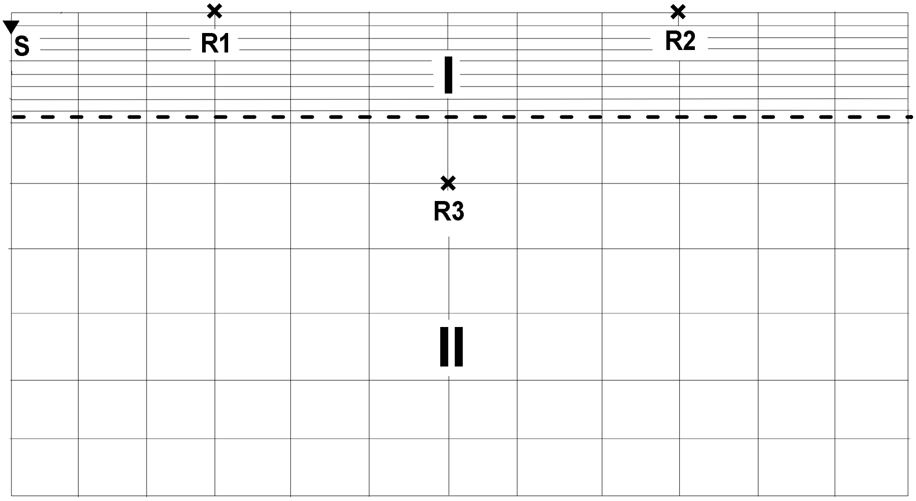

Figure 5.17: *The model of low-velocity layer with irregular grid, which is denser within the layer. The highlighted dashed line is the interface.*

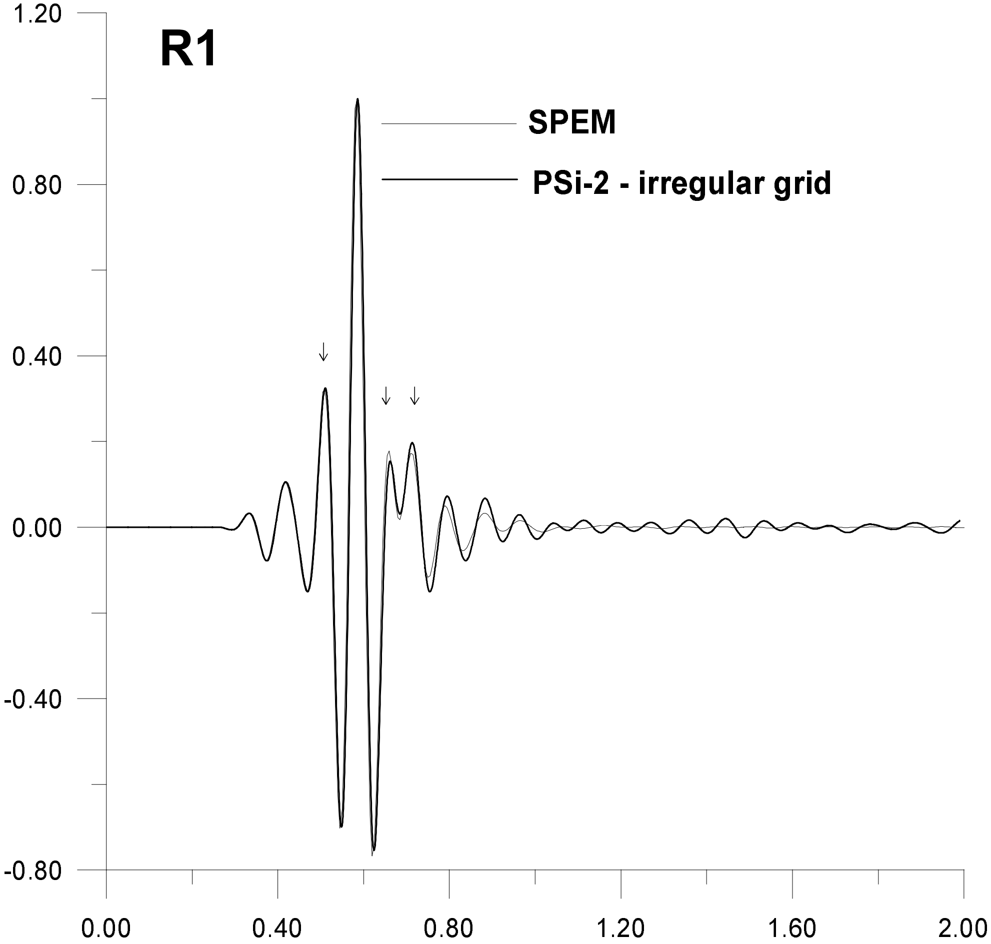

Figure 5.18: *Seismograms for w component in receiver R1 for low-velocity layer model with irregular grid.*

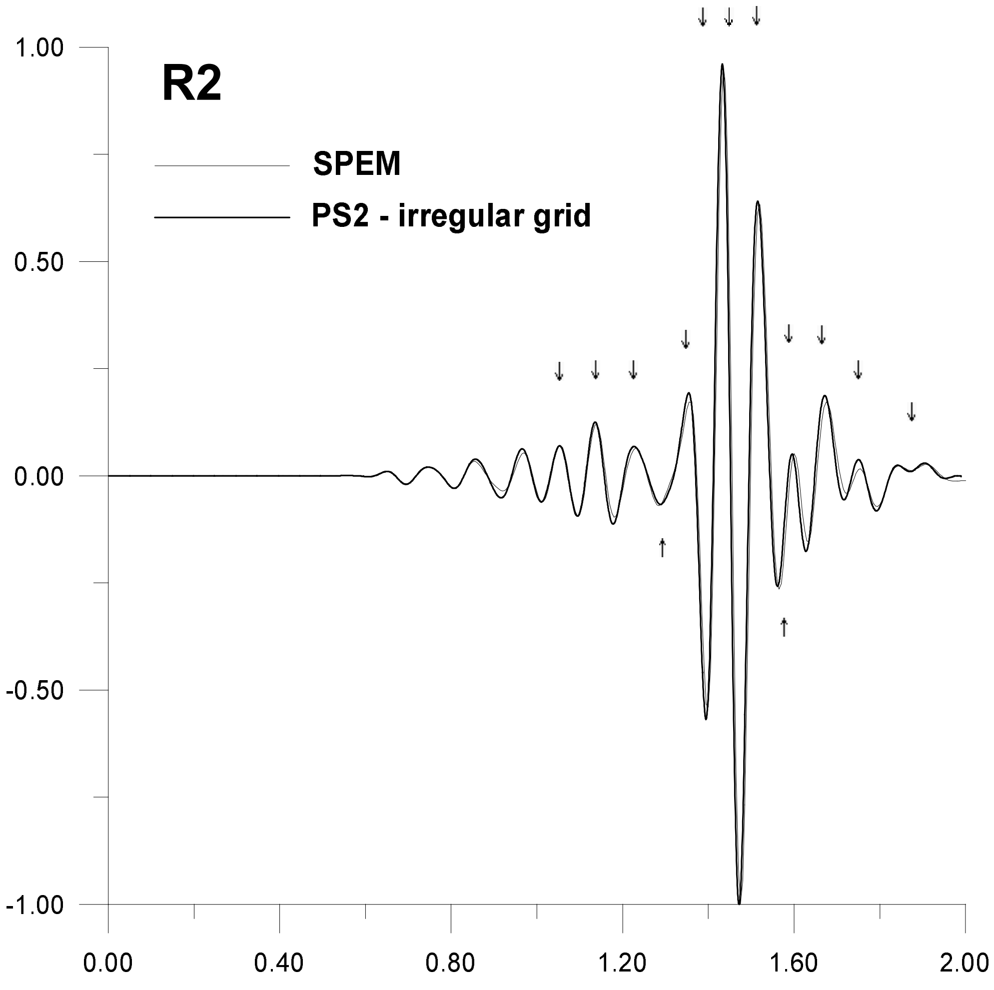

Figure 5.19: *Seismograms for w component in receiver R2 for low-velocity layer model with irregular grid.*

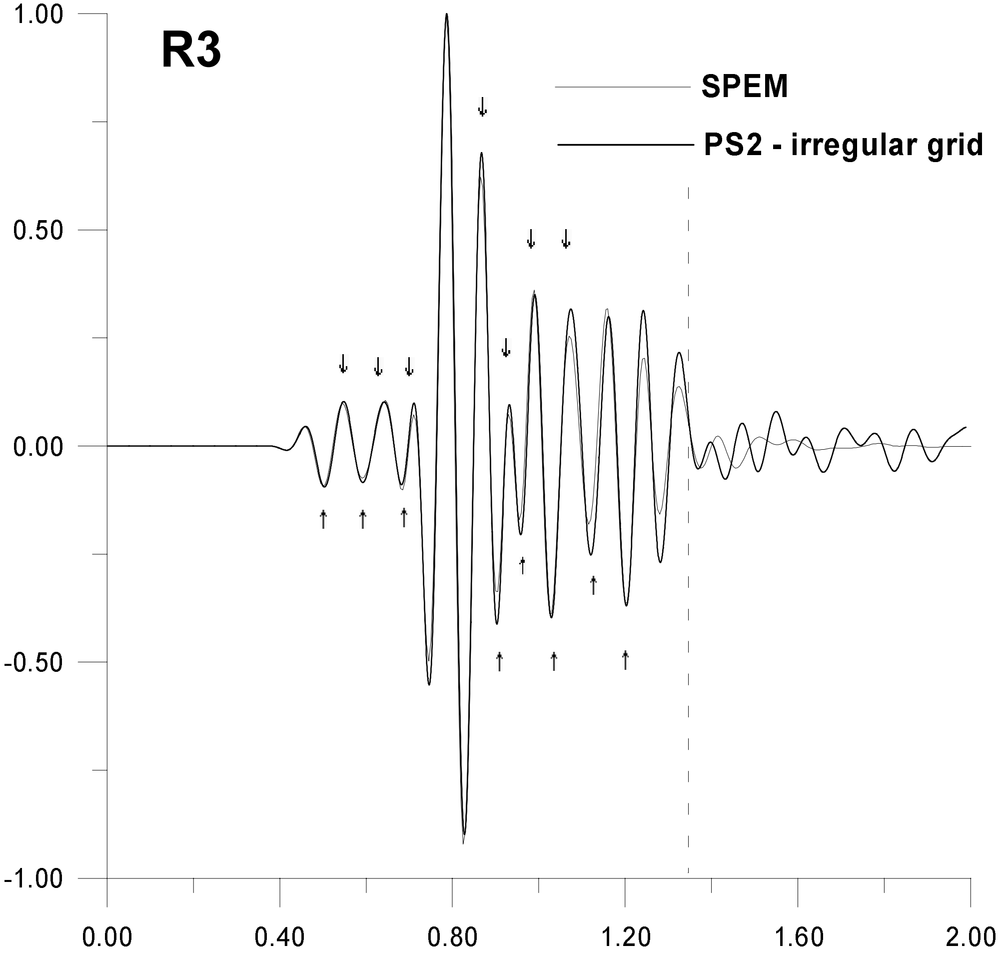

Figure 5.20: *Seismograms for w component in receiver R3 for low-velocity layer model with irregular grid.*

5.2 Topographic features

5.2.1 Step-like surface of homogeneous half-space

In this model we investigated the down-step surface of the homogeneous half-space with an explosive line source, which is denoted by S. The receivers $R1, R2, R3$ were placed as shown in figure 5.21. The grid of the model is regular, with grid step $\Delta z = \Delta z = 1.0$ m. The time function for the explosive source was a finite-duration approximation to Dirac's *delta* function (Aboudi, 1971), with duration time $T = 0.003$ s. There are no artificial reflections in the model, because the arrival time of possible reflections from the boundaries is greater than that of the time window. The parameters of the model are in table 5.9

Table 5.9: *The meaning of the variables is as in table 5.1*

α_I	β_I	ρ_I	f^*_{max}
5000	$5000/\sqrt{3}$	1000	1000

Δt	Δx	Δz	N_t	K	L
0.0001	1.0	1.0	350	320	100

The results were compared with Hong & Bond (1986) in figures 5.21, 5.22, 5.23, where the model is computed by finite differences. Their method is homogeneous, that is the internal grid-points scheme differs from that for the free surface and/or the interface. Moreover the corner grid points are using special formulas (see table 5.2.1).

Our model was exactly the same as that of the referenced paper (hereafter called "original data"), including the employed grid steps. Therefore, the numerical dispersion due to the coarse grid (Alford, Kelly & Boore, 1974) appears in both results. The *original data* for the seismograms, and positions of the receivers and source, were retrieved from a printed copy.

Table 5.10: *The FD formulations used by Hong & Bond(1986), "node" denotes "grid point".*

Node type :	Formulation used :
body node	Bond(1983)
free – surface node	Illan(1975)
surface corner	Illan(1975)

The seismograms were scanned, and digitized. Therefore the accuracy of the *original data* has been substantially affected. Note that the normalizing factors for the receivers $R2$ (table 5.11) are very small, and this also effects the accuracy of the non-normalized seismograms digitized *original data*. Nevertheless, the close agreement of our solution with that of Hong & Bond (1986) is obvious.

Table 5.11: *Relative normalizing factors have the same meaning as in table 5.1.1*

method	n_{R1u}	n_{R2u}	n_{R2u}	n_{R1w}	n_{R2w}	n_{R2w}
$PSi-2$	1.00	0.49	0.42	0.53	0.16	0.13
ORIGINAL DATA	1.00	0.46	0.41	0.47	0.14	0.13

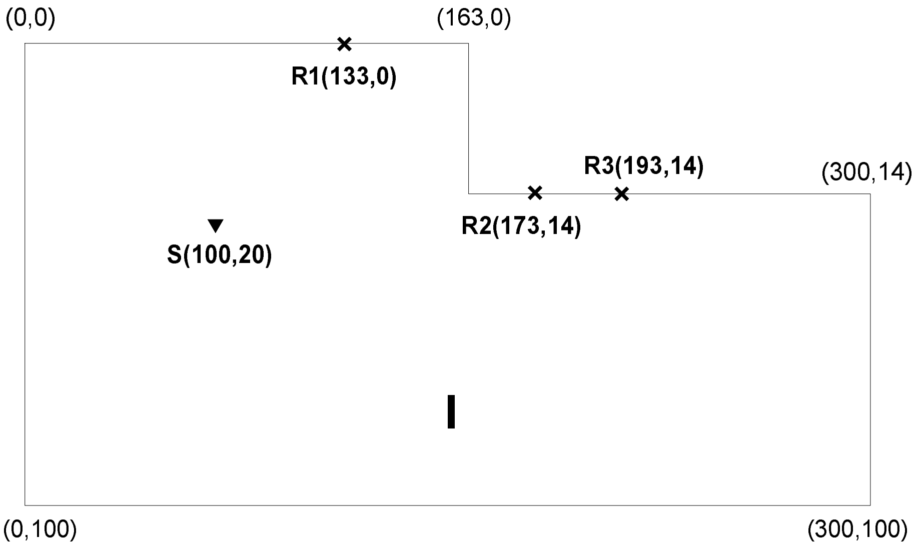

Figure 5.21: *Step-like surface of homogeneous half-space (coordinates in metres).*

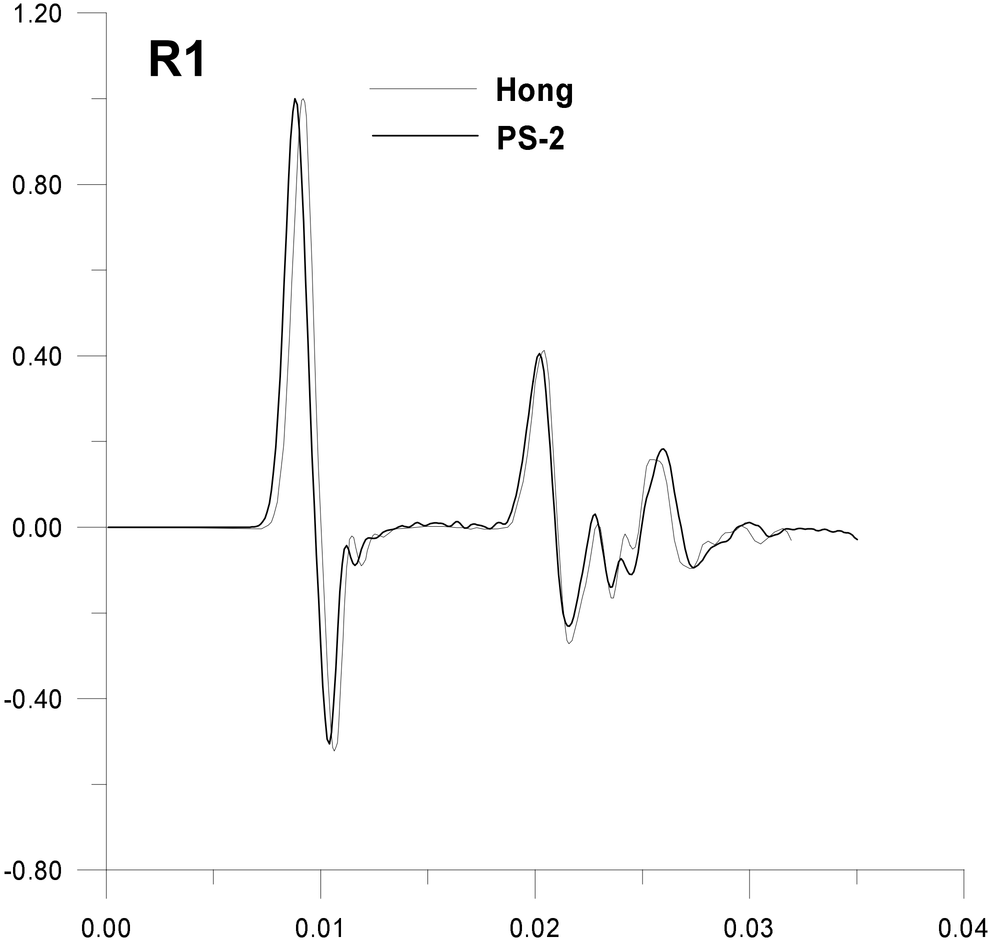

Figure 5.22: *Seismograms for u component in receiver R1 for down-step surface model with a regular grid.*

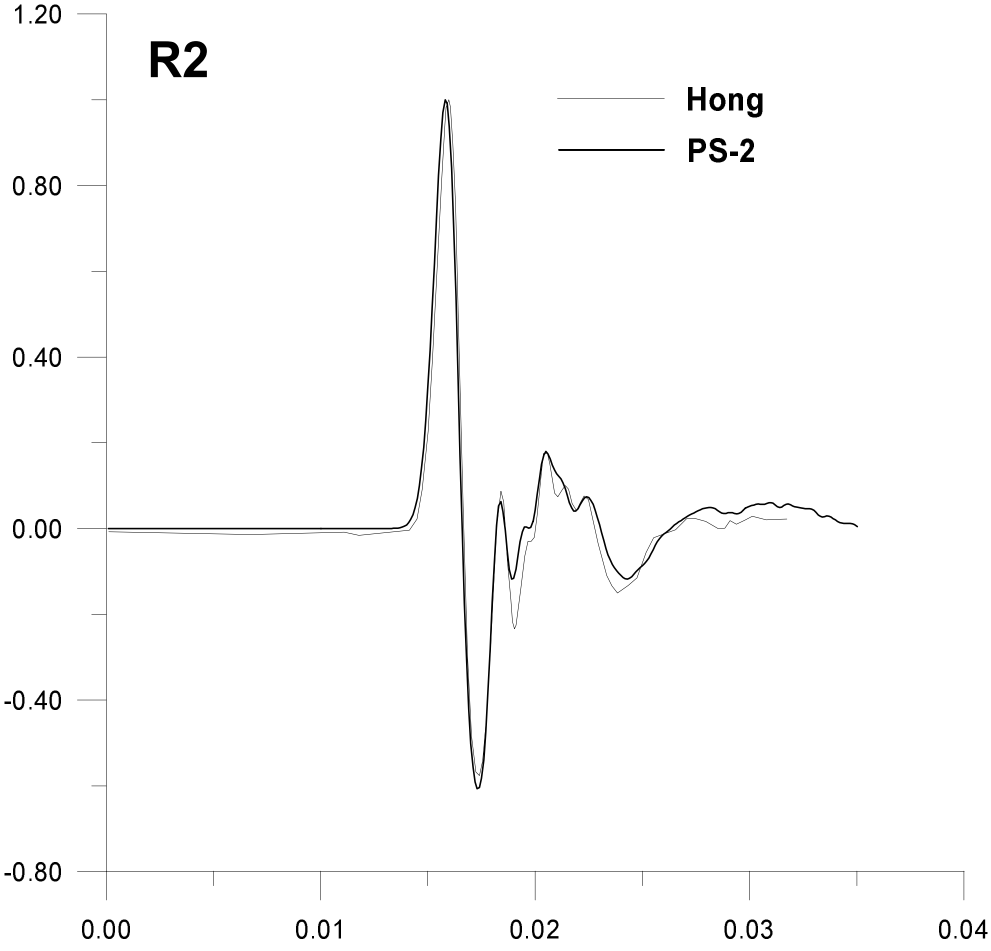

Figure 5.23: *Seismograms for u component in receiver R2 for down-step surface model with a regular grid.*

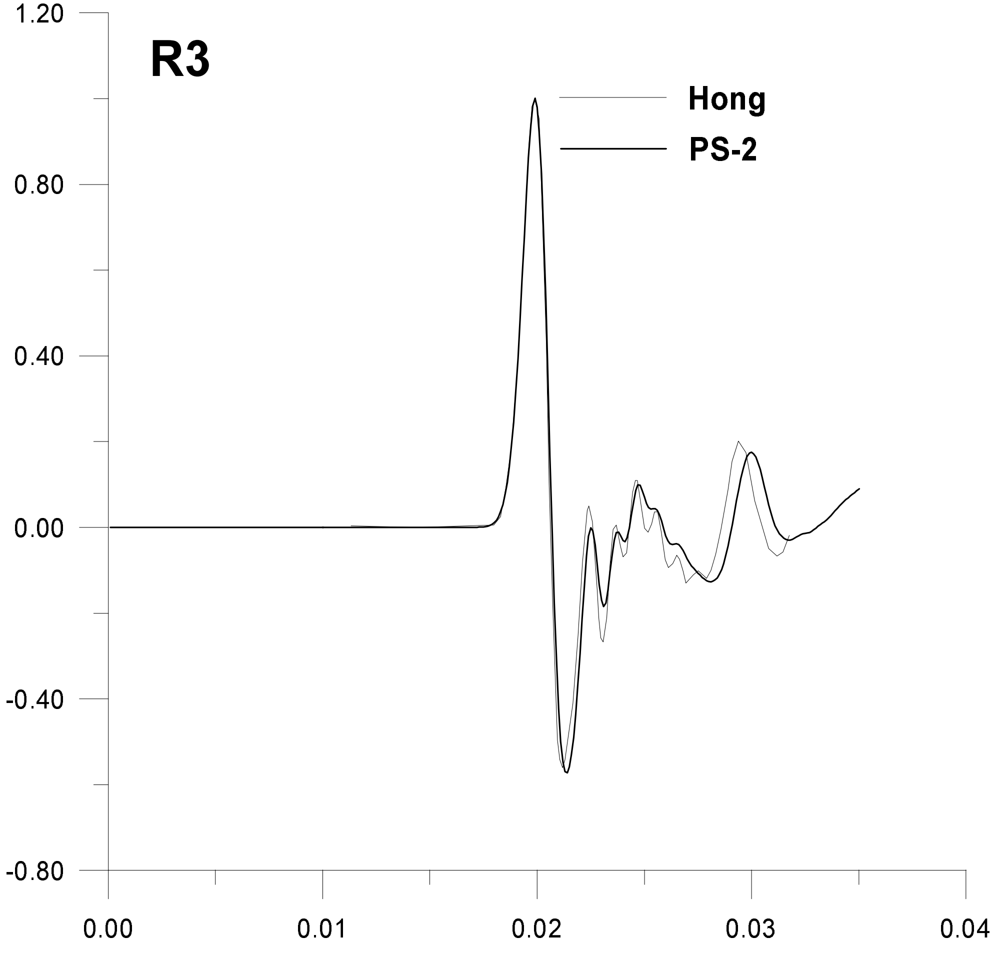

Figure 5.24: *Seismograms for w component in receiver R3 for down-step surface model with a regular grid.*

5.2.2 Ridge-like surface of homogeneous half-space

Because the effective parameters are obtained by geometric averaging, the free topographic surface is not smooth (in contrast to the internal boundaries), but it is composed of elementary steps. Therefore we must approximate the non-planar surface by an irregular meshing. The grid is denser in places with significant topographic features, and coarser in places with a horizontal (or vertical) free surface. We investigated about 10 different kinds of grids for this model, three of them are presented below.

The ridge is symmetrical, and the line explosive source is placed on the vertical symmetry plane at the base of the ridge (see figure 5.25, or the details in figures 5.26 , 5.27). Therefore, we use the symmetry condition for the explosive source (4.29, 4.30), and it is applied at the left-hand side of the model. The receivers $R1..R12$ are located on a free surface with a constant horizontal spacing of 166.66 m, the $R1$ receiver is on the top of the ridge (see figures 5.26 , 5.27).

The model is large, and so there are no artificial reflections arriving to any of the receivers during the defined time window.

The source time function in all the ridge-like models is:

$$f(t) = (b - 0.5) exp(-b) \ , \tag{5.2}$$

$$b = [\pi(t - t_s)/t_p]^2 \ ,$$

$$\text{with } t_p = 0.4875 s, \quad t_s = 0.4875 \text{ s} \ .$$

The time window was $t \in (0s, 4.0s)$ The surface shape is (Bouchon, 1989):

$$s(x) = h(1.0 - a) exp(-3a) \tag{5.3}$$

$$a = (x/l)^2 \ ,$$

$$\text{with } h = 375 \text{ m}, \ l = 1000 \text{ m} \ ,$$

where h and l denote the height and the half-width of the hill.
The equation (5.3) is applied for $x \in (0, l)$, while $s(x) = 0$ for $x > l$.

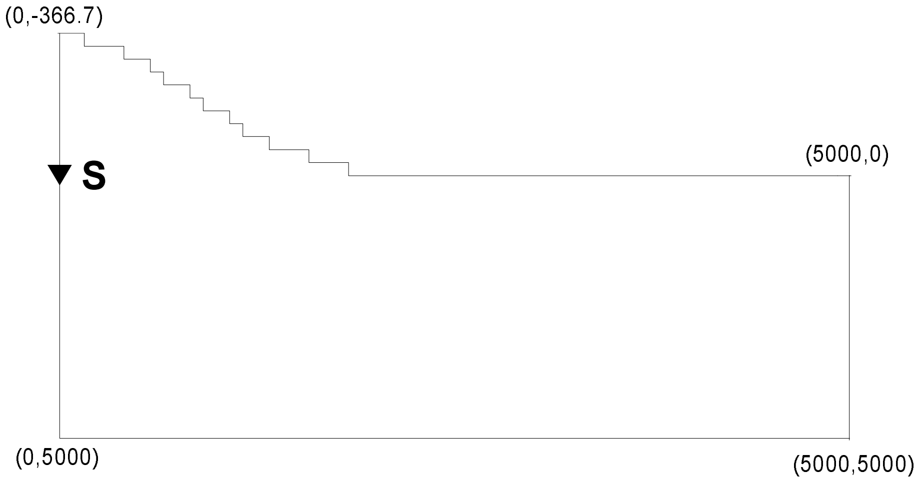

Figure 5.25: *The model of the ridge. The vertical coordinate of the upper left corner might differ in cases of a different meshing. (coordinates in metres).*

Coarse grid model M1 (regular grid)

The parameters of the model are shown in table 5.12. The detailed view at the model surface is in figure 5.26, and the seismograms are in figures 5.28 and 5.29.

Fine grid model M2 (regular grid)

The parameters of the model are shown in table 5.13. The detailed view of the model surface is in figure 5.27. The seismograms are displayed in figures 5.28 and 5.29, where they are compared with the results for the coarse grid.

The results computed for the model $M2$ on the regular fine grid (see table 5.13) were compared with the results obtained from S.Gaffet com-

Table 5.12: *The meaning of the variables is as in table 5.1*

α_I	β_I	ρ_I	f^*_{max}
2000	1000	1000	5.4

Δt	Δx	Δz	N_t	K	L
0.008	33.33	33.33	500	150	150

Table 5.13: *The meaning of the variables is as in table 5.1*

α_I	β_I	ρ_I	f^*_{max}
2000	1000	1000	5.4

Δt	Δx	Δz	N_t	K	L
0.0016	6.667	6.667	2500	750	660

puted by the *Boundary equation Integral Method* (Gaffet & Bouchon, 1989). The comparison is in figures 5.33, 5.34 with *original data* denoting the solution of S.Gaffet.

The agreement is not close, and that is why we agreed with S. Gaffet on the continuing investigation of the problem for this and similar models.

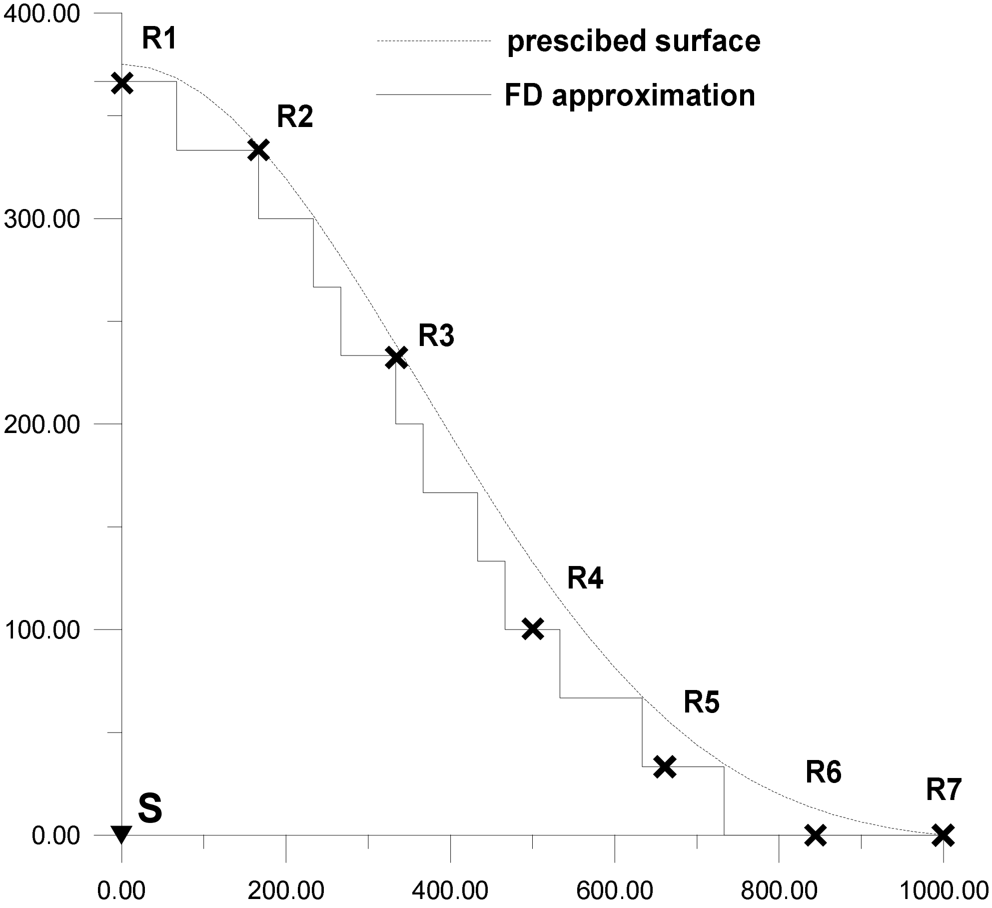

Figure 5.26: *The detail of the ridge for a coarse grid* $\Delta x = \Delta z \doteq 33.33$ m *(coordinates in meters).*

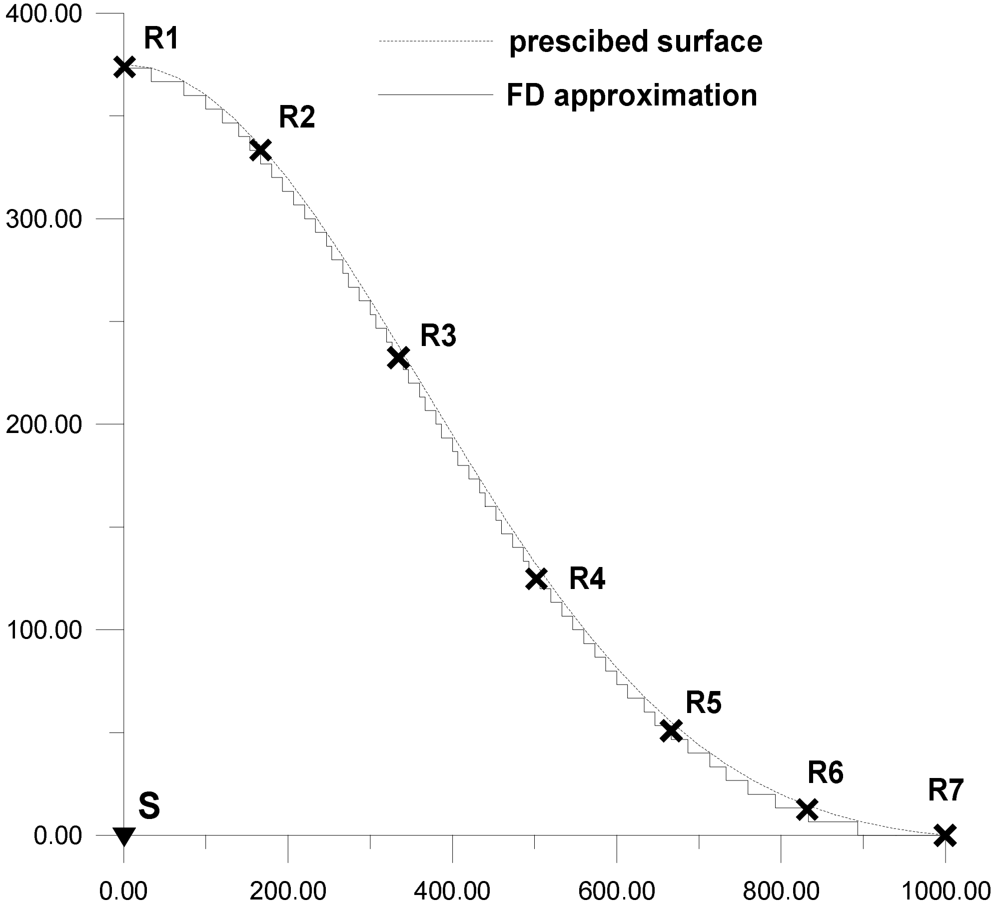

Figure 5.27: *The detail of the ridge for fine-grid model* $\Delta x = \Delta z \doteq 6.67$ m *(coordinates in meters).*

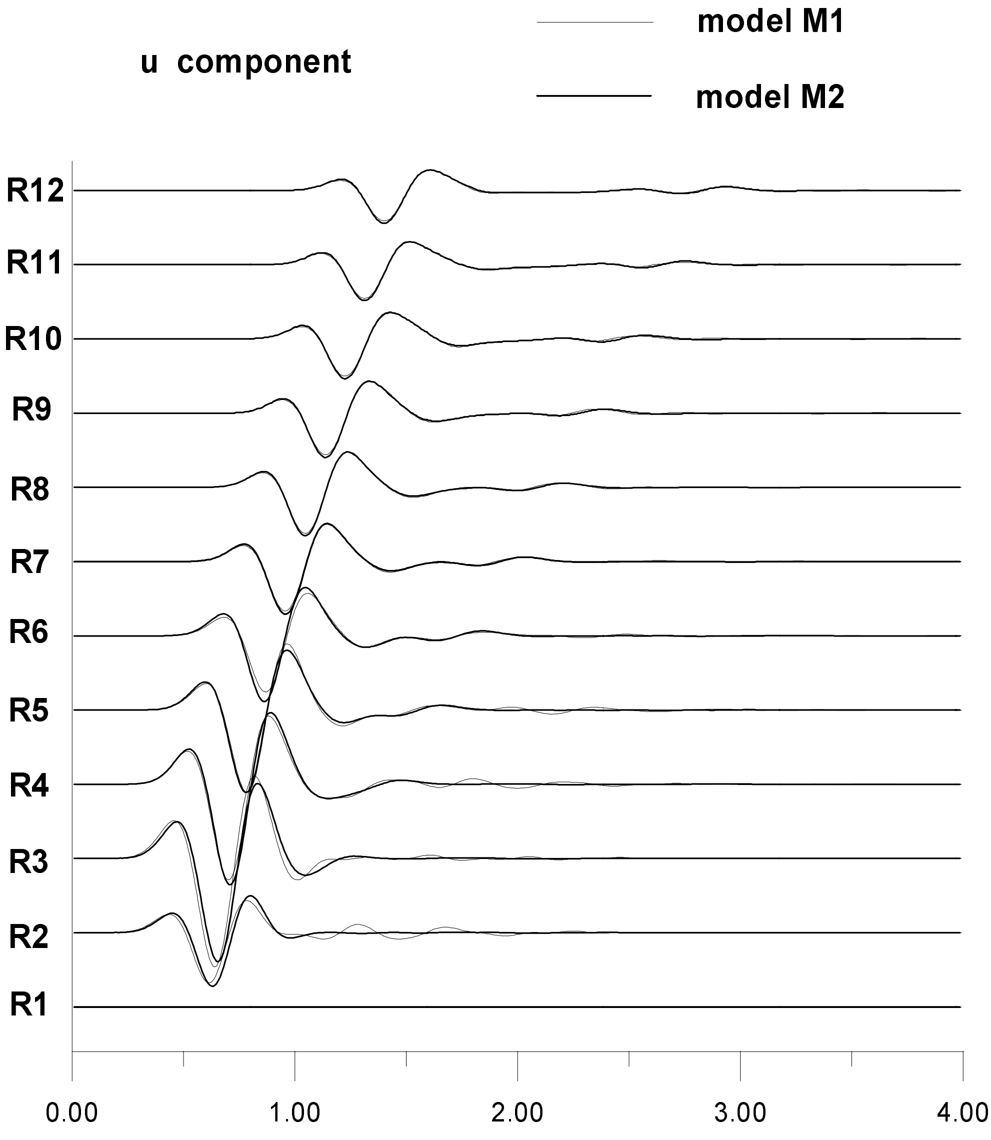

Figure 5.28: *Seismograms for the coarse-grid and fine-grid models,both on a regular grid.*

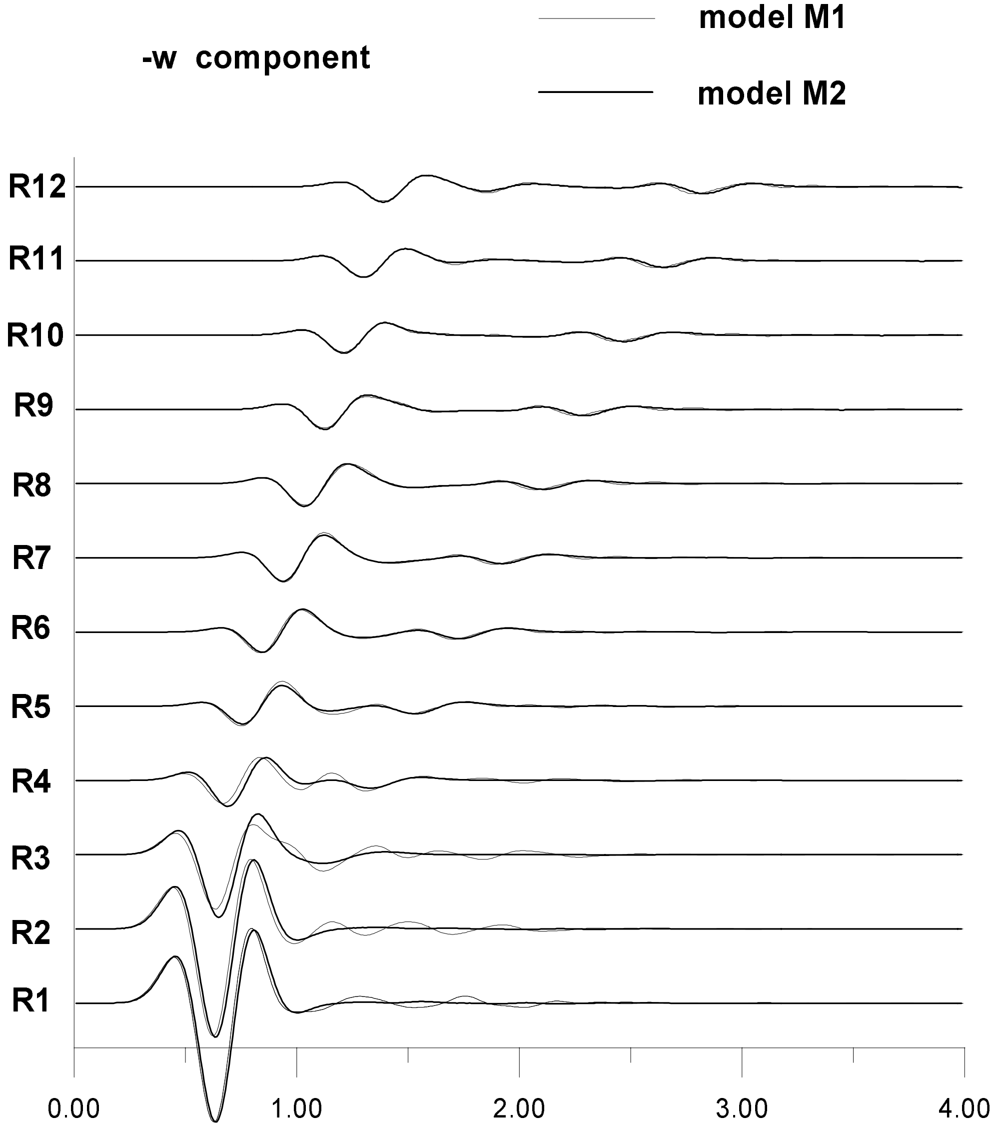

Figure 5.29: *Seismograms for the coarse-grid and fine-grid models,both on a regular grid.*

Fine grid model M3 (irregular grid)

In this model, there is also a fine grid, with the smallest grid step of $\Delta x = \Delta z = 3.333$ m, but the horizontal lines are dense from the top of the hill to the depth of two fine-grid steps under the horizontal plane free-surface level. Then the grid steps increase 10 times at once. This means that two grid steps under the surface the ratio of the second and third grid step under the surface is 10, and from this place to the end of the model the grid is again regular with grid step $\Delta z = 33.33$ m. The described type of the transition from a fine to a coarse grid is shown for the horizontal grid lines (figure 5.30). In this model, there is a change of the vertical lines meshing abrupt as well, but the transition from the fine to the coarse grid is at the horizontal distance of $x = 1000$ m. The parameters of the model are shown in table 5.14. The results for the irregular fine-grid model are in figures 5.31 and 5.32, where they are compared with the results for the regular fine grid.

Table 5.14: *The meaning of the variables is:* α_I, β_I *- P, S wave velocities* (m/s)*;* ρ_I *-density* (kg/m^3)*;* f^*_{max} *-the frequency* (Hz) *at which the absolute value of the spectrum is* 1% *of the maximum spectral value;* Δt *-time step* (s)*;* $\Delta x_{min}, \Delta z_{min}, \Delta x_{min}, \Delta z_{min}$ *are the minimum and the maximum grid steps* (m) *appearing in the model;* N_t *-number of time steps;* K, L *-number of vertical and horizontal lines in the model*

α_I	β_I	ρ_I	f^*_{max}	Δt
2000	1000	1000	5.4	0.0008

Δx_{min}	Δz_{min}	Δx_{max}	Δz_{max}	N_t	K	L
3.333	3.333	33.33	33.33	10000	290	195

The comparison shows that the abrupt change in the grid density doesn't yield any significant change in the seismograms. The computa-

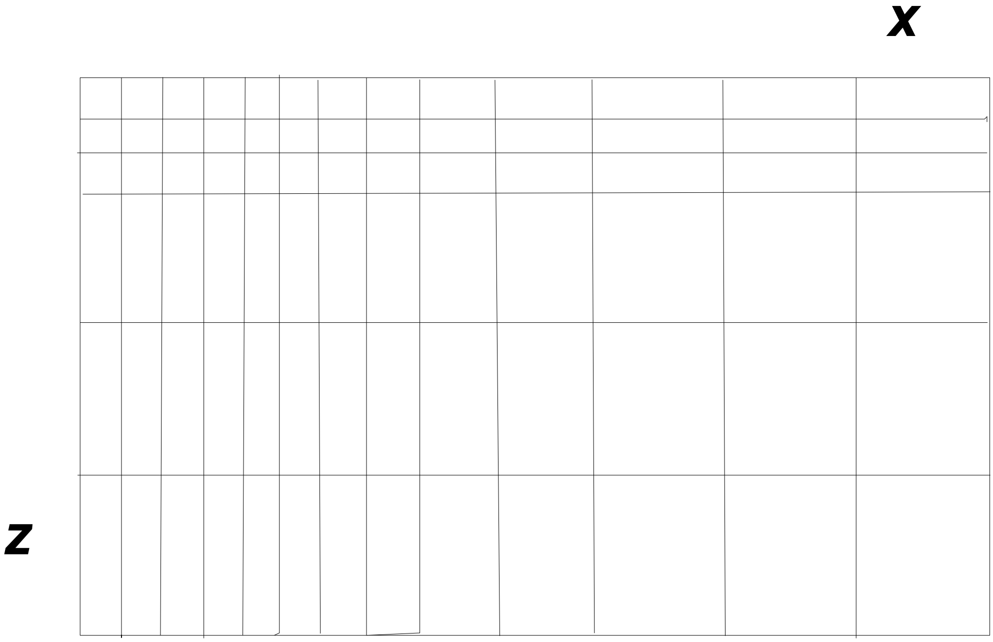

Figure 5.30: *The grid in this figure is made abruptly coarser in the* z *direction, and smoothly in the* x *direction.*

tion is done with the time step that is determined by the minimum spatial step, maximum velocity and the stability condition (section 3.3.6). Therefore, such time step is rather small for those zones of the model where the spatial step is large. Although there is appearing the small ratio $\frac{\Delta t}{\Delta x}$ in this model (Alford, Kelly & Boore, 1974), no visible increase of the dispersion has been found in our results.

We also computed the same model with a smooth change of Δx, and Δz grid steps. The principle of the smooth change is shown in figure 5.30, where it is just shown for the vertical lines. The change started at $x = 1000.0$ m for $\Delta x = 3.333$ m, and it ended at $x = 1166.7$ m, with $\Delta x = 33.33$ m after 13 varying grid steps. The length of grid steps increased as a geometric series with factor $q \doteq 1.2$. The Δz grid step was treated in the same way, the change started at $Z = 6.666$ m, and ended at $z = 111$ m, the proportions of the change were the same as for Δz. The results of this model were also quite similar to those of model $M3$, with only negligible differences.

Thus the abrupt change in the grid density doesn't affect the results in comparison with either those of the model with the smooth change of grid density, so those with a regular grid.

Model M4 (regular grid)

This model is exactly the same as model $M2$, but the source is placed at a depth of $z = 40.0$ m. This is because we received the results for comparison computed for this source depth by the Boundary Integral Equation Method ($BIEM$) (Gaffet & Bouchon, 1989). Nevertheless the difference between The $BIEM$ synthetics contain high frequency oscillations. The question is, whether the oscillations in the $BIEM$ results would be smaller in case of finer sampling of the surface, which now goes from 14 m (for high frequencies) to 47 m (for low frequencies) (personal communication with S. Gaffet). Model with the finest irregular grid computed by the $PSi-2$ had grid step along the topography equal to 3.333 m.

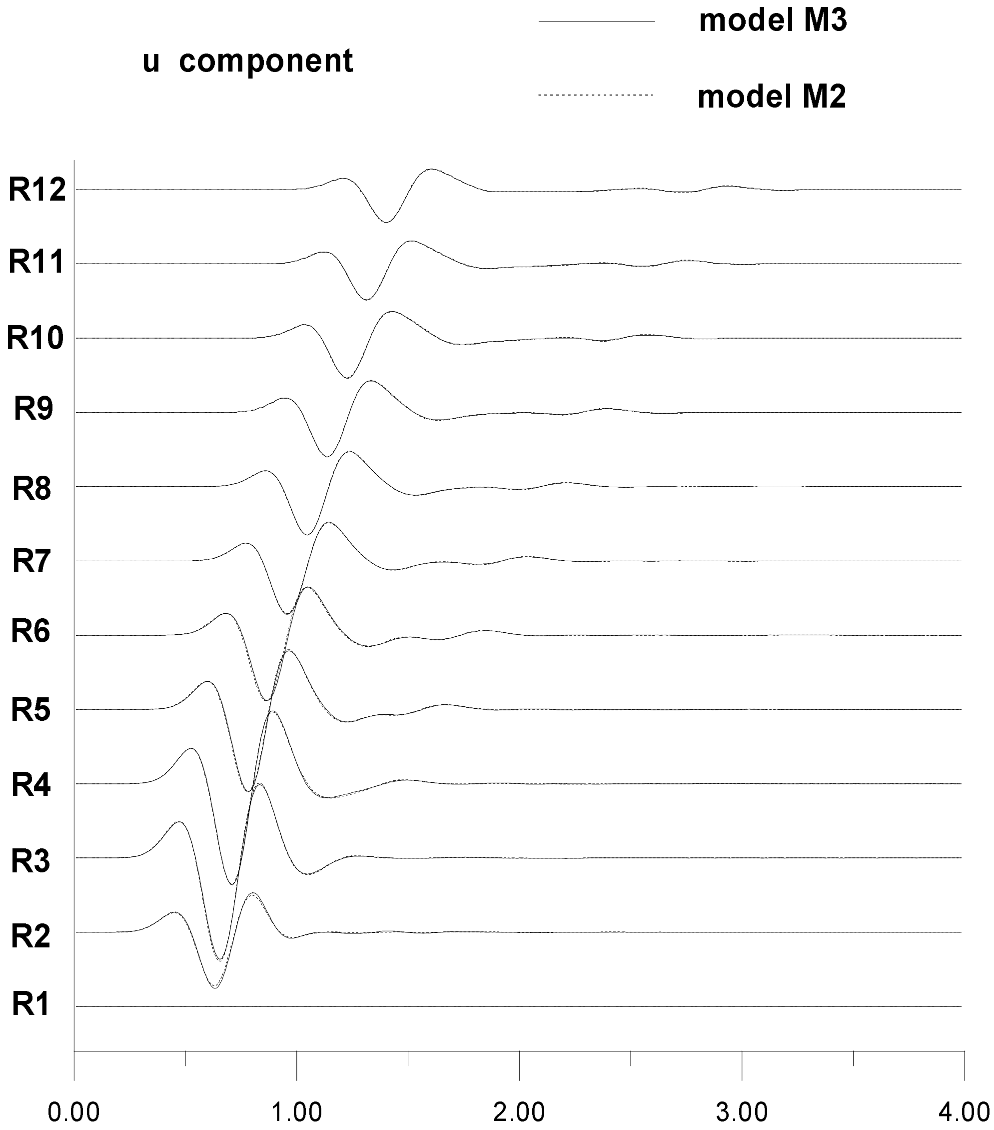

Figure 5.31: *Seismograms for the fine-grid models with regular and irregular grid.*

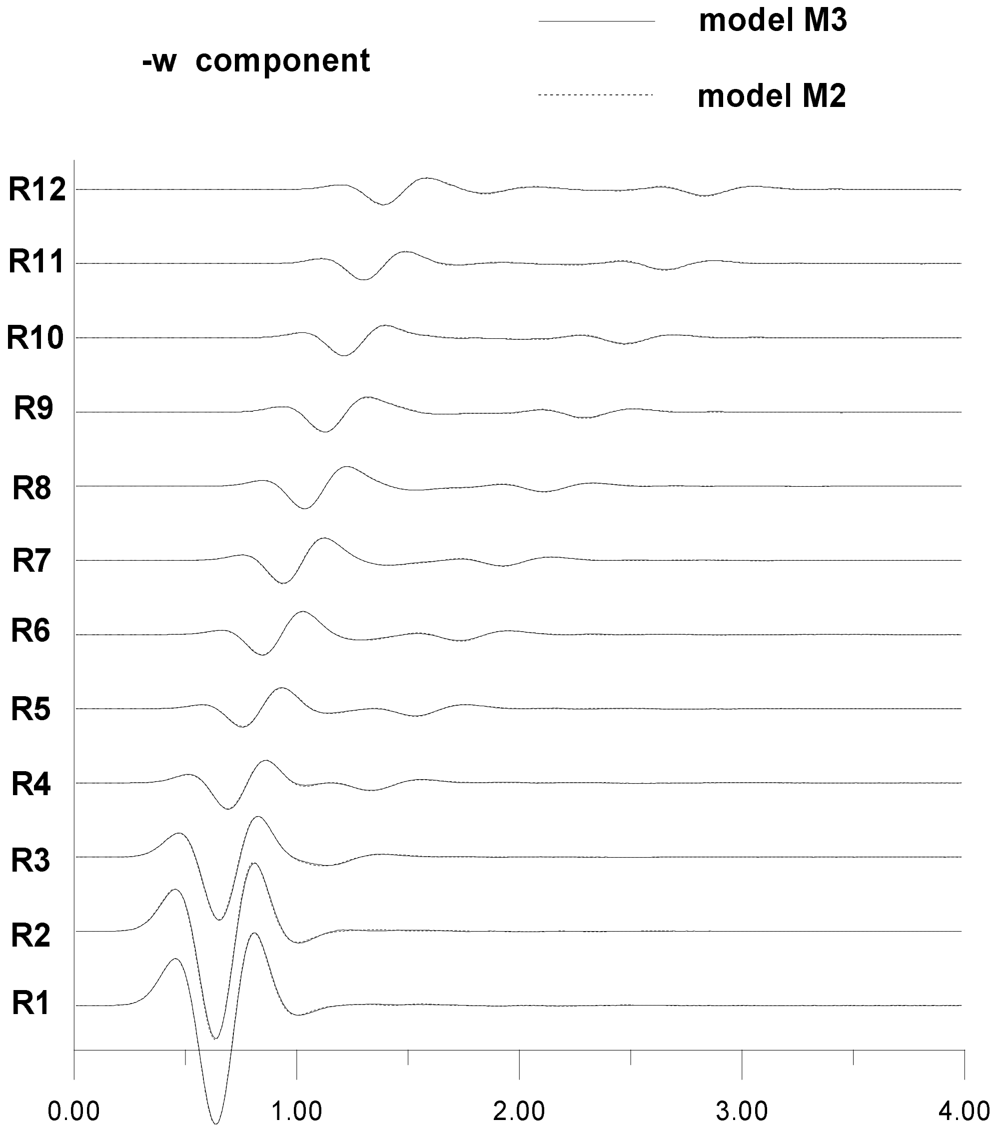

Figure 5.32: *Seismograms for the fine-grid models with regular and irregular grid.*

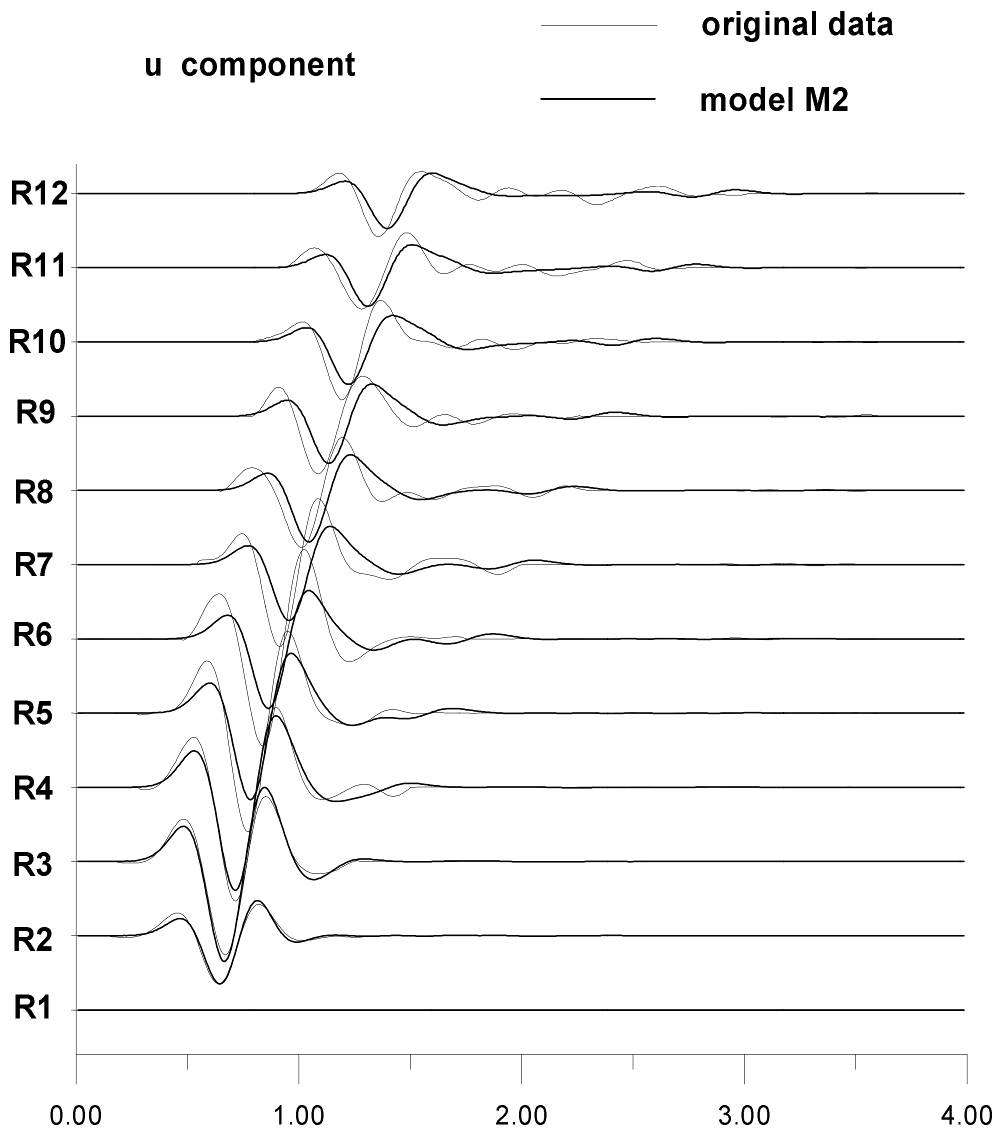

Figure 5.33: *Seismograms for the fine-grid model on irregular grid compared with results obtained from the Boundary Integral Equation Method.*

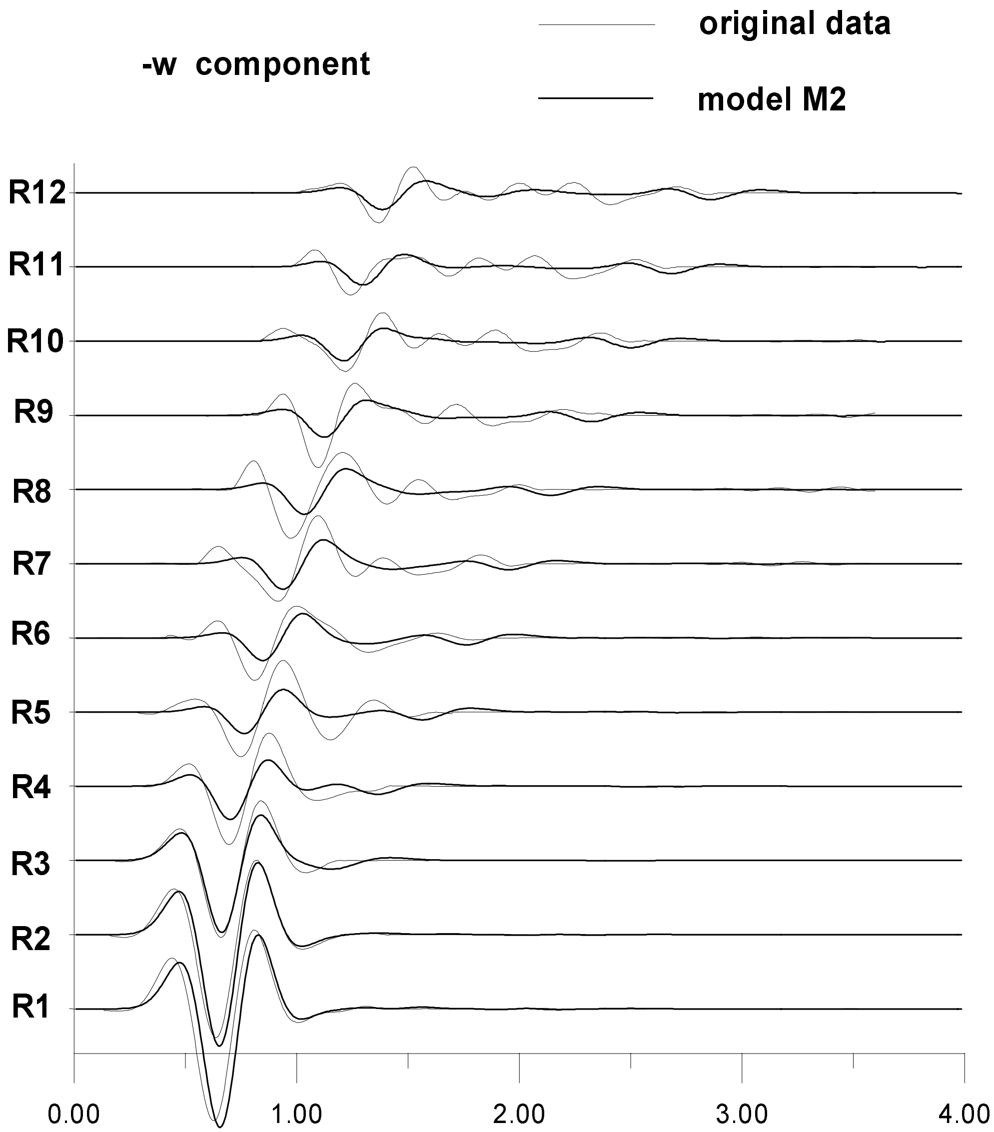

Figure 5.34: *Seismograms for the fine-grid model on a regular grid compared with results obtained from the Boundary Integral Equation Method.*

5.2.3 Ramp-like surface of homogeneous half-space

The model is a 45° ramp. The inclined surface is approximated by elementary steps, as in 5.2.2 (see also figure 5.35). The width and the height of the ramp is 640.0 m. The grid step of $\Delta x = 5.00$ m is used in the whole model. The grid step of $\Delta z = 5.00$ m is used from the top of the model to the grid line $z = 10.0$ m, from this grid line to the bottom of the model the grid step is $\Delta z = 10.00$ m. The source is a plane P wave incident vertically from below, and realized by vertical body forces applied along a horizontal grid line. The vertical position of this line is at $z = 345$ m (figure 5.35, where denoted as "source line"). On the left and right hand side of the model we apply the "symmetry condition" (4.29, 4.30) (i.e. symmetry in the w component, and antisymmetry in the u component). The bottom of the model is treated by Stacey's non-reflecting boundary condition combined with the taper of 40 grid points. The source time function is:

$$f(t) = \sin\left(\frac{2\pi t}{t_s}\right) - \frac{1}{2}\cdot\sin\left(\frac{4\pi t}{t_s}\right), \qquad (5.4)$$

with $t_s = 0.06$ s, the duration of signal.

The time window for the source time function is t_s, the time window for the computation is 1.5 s. Model parameters are in table 5.15. The results for the u and w component are in figures 5.36, 5.37, respectively.

The intention of this experiment was to compare its results with the solution by Jih *et al* (1988), but has not yet been possible for some uncertainties in the model constitution, and in the boundary conditions.

Table 5.15: *The meaning of the variables is the same as in table 5.37*

α_I	β_I	ρ_I	f^*_{max}	Δt
5020	2898	2100	50.0	0.0006

Δx_{min}	Δz_{min}	Δx_{max}	Δz_{max}	N_t	K	L
5.0	5.0	5.0	10.0	2500	1000	470

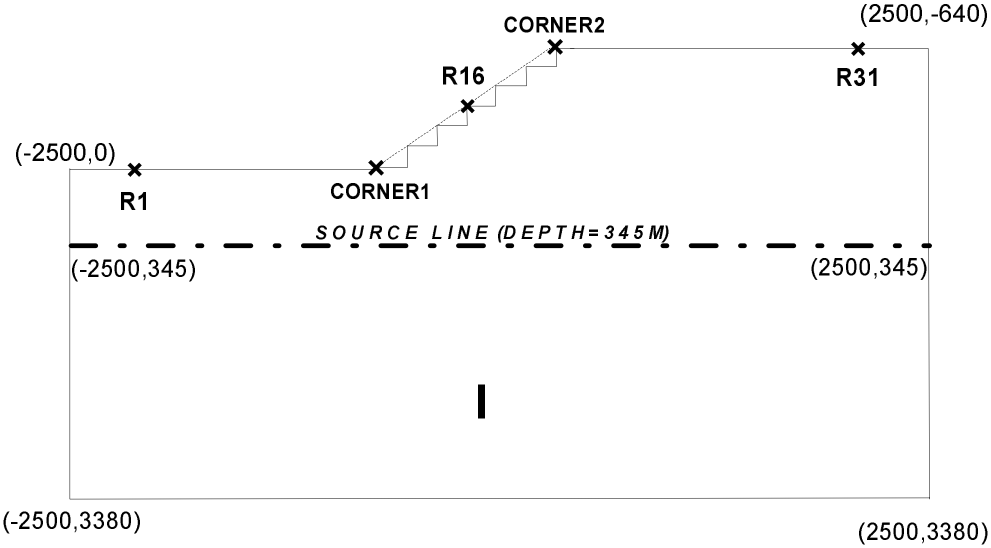

Figure 5.35: *The ramp-like surface of homogeneous half-space. The thin dotted line represents the prescribed function of the surface shape, the continuous line is the model approximation to this function. The elementary steps are just schematic i.e. their number and their relative size differs from the computed model. The highlighted dotted-and-dashed "source line" represents the line along which the vertical body forces of the source is applied to generate a vertical incident plane wave. (coordinates in metres)*

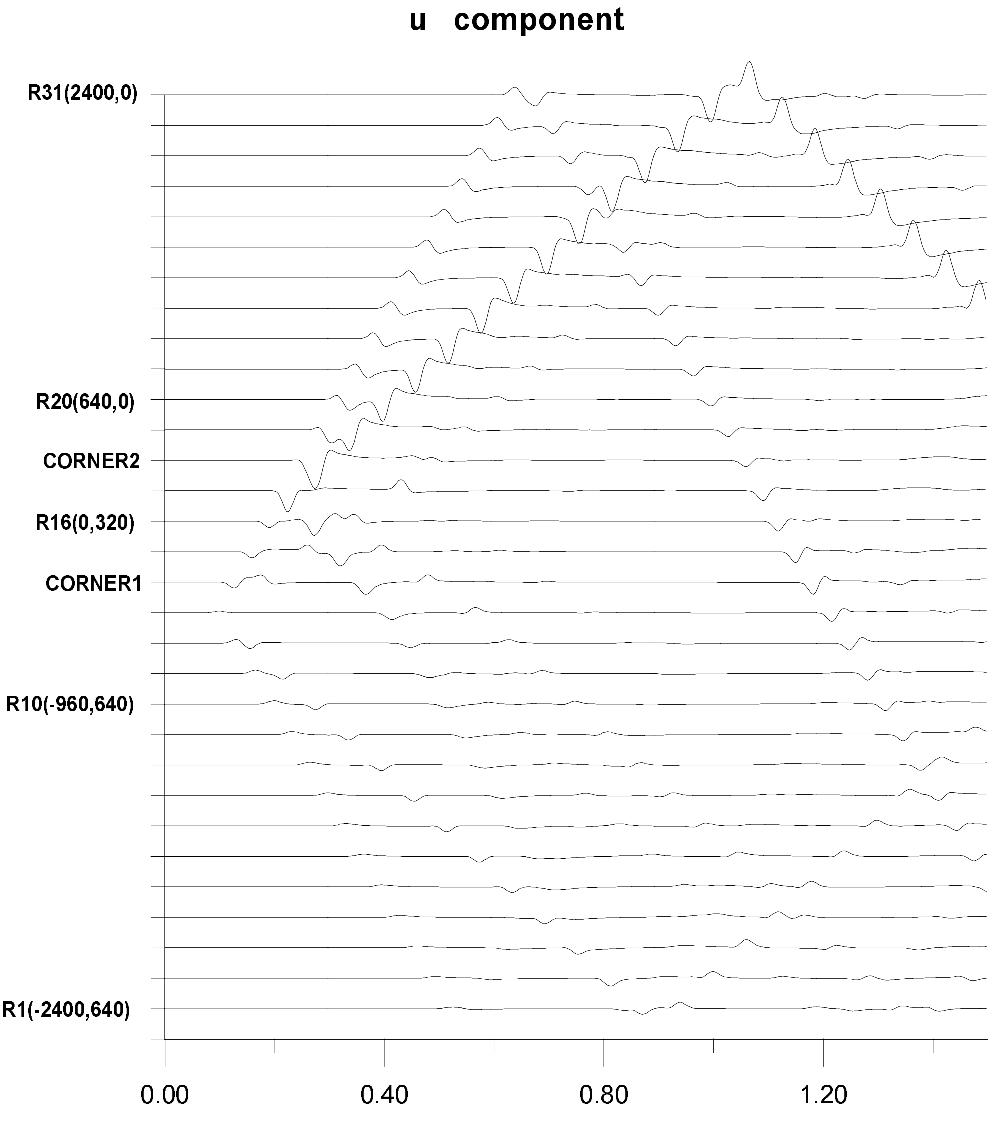

Figure 5.36: *Seismograms for the ramp-like surface of homogeneous half-space, incident P wave.*

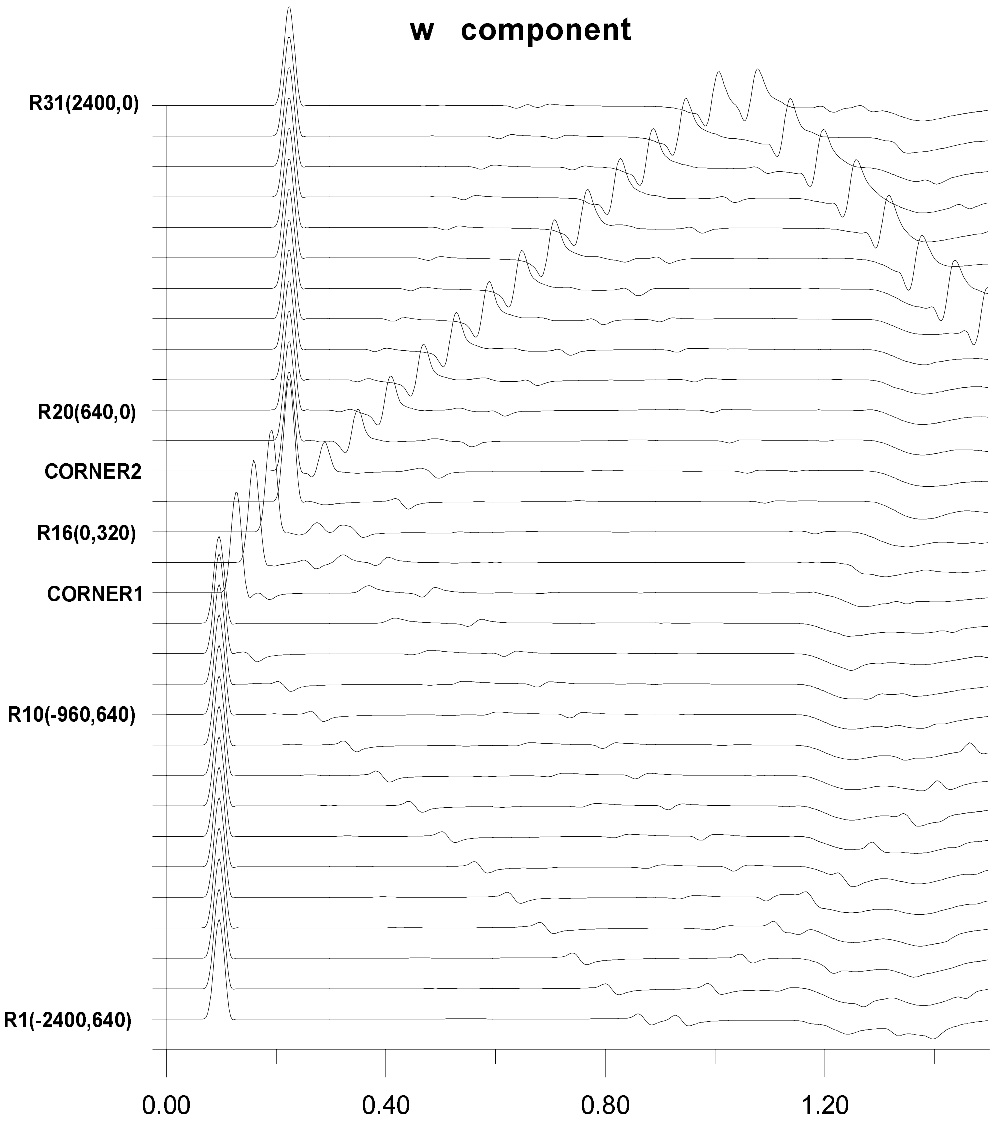

Figure 5.37: *Seismograms for the ramp-like surface of homogeneous half-space, incident P wave.*

5.2.4 Step-like layer of low velocities underlain by homogeneous half-space

The model we investigate here is specified by figure 5.38. The block denoted as I is a low velocity layer with a step-like surface, and it is underlain by block II, a homogeneous half-space with a step-like interface. We computed it both on regular and irregular grids (specified later), and the results were compared with the $SPEM$ method (Seriani, Priolo, Carcione & Padovani, 1992). The $SPEM$ results were obtained after personal communication with E.Priolo. The topography of this model, and the position of the interface, the source (S), and the receivers ($R1$ .. $R8$) is in figure 5.38. The line source is realized by a vertical body force on the surface. The source time function is:

$$f(t) = \frac{a_0 + a_1 t + a_2 t^2}{d_0 + d_1 t + d_2 t^2}[b_0 \cdot \cos(b_1 + b_2 t)] \cdot exp[c_1(t - c_0) + c_2(t - c_0)^2] \ , \quad (5.5)$$

with

$$\begin{gathered} a_1 = a_2 = b_2 = c_1 = d_1 = d_2 = 0 \ , \\ b_0 = c_0 = d_0 = 1 \ , \\ a_0 = 1000, \ b_1 = 22, \ c_2 = 3.6 \ . \end{gathered}$$

The source time function was also retrieved from E.Priolo in the form of the Fortran code function. Thus the time function is the same as that used for the $SPEM$ model for comparison (Seriani, Priolo, Carcione & Padovani, 1992). The time window for the source time function is 0.2s, while that for the computation being 0.6s.

For both sides and the bottom of all computed models, we used Stacey's non-reflecting boundary conditions joined together with tapers of 40 points.

Model S1 (regular grid)

The grid step is the same in both directions $\Delta x = \Delta z = 2.40$ m, thus there are 20 vertical grid steps between the receivers $R2$ and $R3$, and with the other receivers being analogous. The results are presented in figures 5.40, and 5.41. The parameters are listed in table 5.16.

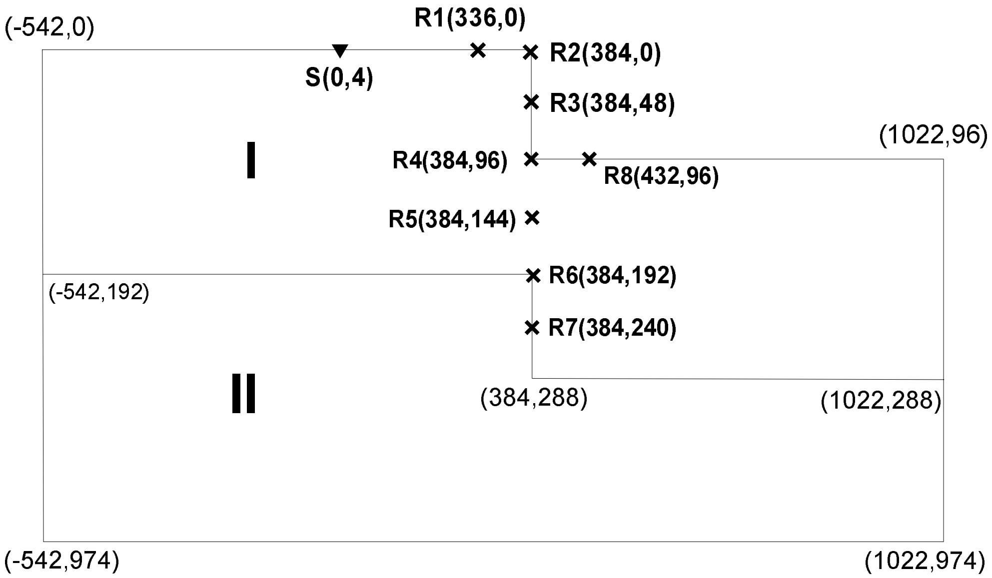

Figure 5.38: *The model of the step-like layer (coordinates in metres).*

Model S2 (irregular grid)

The grid step is the same in both directions, $\Delta x = \Delta z = 2.40$ m, while 5 grid steps along the interfaces, as well as along the free surface, the grid steps are $\Delta x = 0.48$ m and/or $\Delta z = 0.48$ m, as shown in figure 5.39. The grid steps change abruptly.

The results shown in figures 5.40, and 5.41 are compared to the regular grid model $S1$, described previously. The parameters are in table 5.17.

The results in figures 5.40 and 5.41 scarcely differ from one another. At receiver $R2$, there is a numerical instability appearing in the time that is indicated by the dashed-line frame in figures 5.40 and 5.41. The instability appears due to the actual length of the time step in model $S2$. The detailed description of this occurrence, and the way in which it is possible to stabilize the solution is in section 3.3.6, subsection I.

Table 5.16: *The meaning of the variables is the same as in table 5.3*

α_I	β_I	ρ_I	α_{II}	β_{II}	ρ_{II}	f^*_{max}
2000	1200	2100	3000	1750	2300	22

Δt	Δx	Δz	N_t	K	L
0.0005	2.4	2.4	1200	653	408

Table 5.17: *The meaning of the variables is the same as in table 5.4*

α_I	β_I	ρ_I	α_{II}	β_{II}	ρ_{II}	f^*_{max}
2000	1200	2100	3000	1750	2300	22

Δt	Δx_{min}	Δz_{min}	Δx_{max}	Δz_{max}	N_t	K	L
0.0001	0.48	0.48	2.4	2.4	6000	663	443

We also made a computation employing special formulas for the corners with receivers $R2$, and $R4$. The value for each displacement component is retrieved by a linear extrapolation for the "outer corner" (receiver $R2$), or by a linear interpolation for the "inner corner" (receiver $R4$). The described model with the interpolated/extrapolated surface corners was computed on either the regular and the irregular grid. The agreement with the results from model $S1$ and/or model $S2$ was also very close, the curves were not negligible from each other in the scale of figure 5.40.

In figures 5.42 and 5.43, there is a comparison of our results computed for model $S1$ with those obtained for the same model by the $SPEM$ method. The difference appears for the Rayleigh wave that is propagating along the vertical free surface downwards. The $SPEM$ method results were repeated also for a fine-grid model, and they did not differ

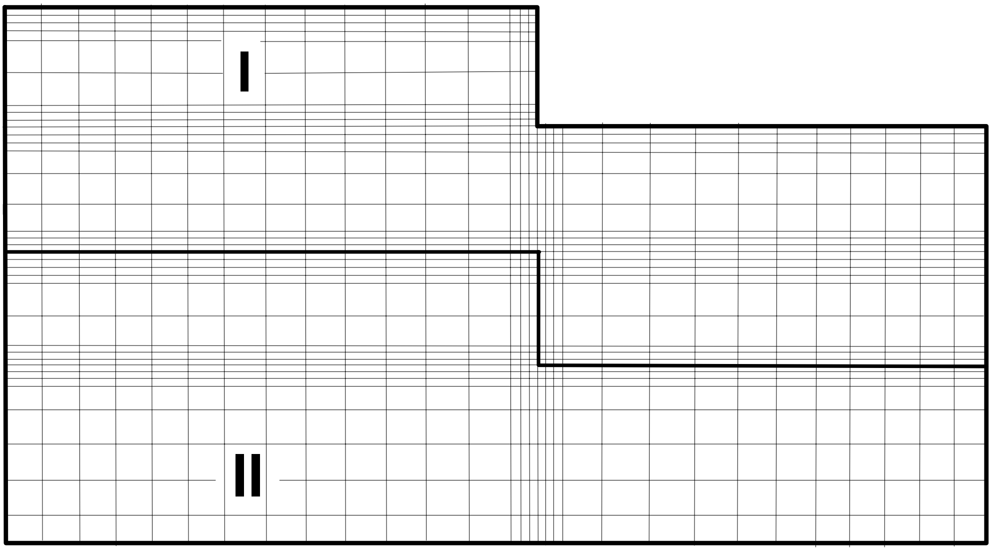

Figure 5.39: *The step-like layer model with fine grid along the interfaces and surface. The interface is represented by the highlighted line inside the model. The positions of the source and receivers remain unchanged with respect to figure 5.38.*

from the presented ones (not shown here; personal communication with E.Priolo).

Since the solution by $PSi-2$ scheme is convergent as the spatial step decreases (models $S1$, $S2$), and the same is also valid for the $SPEM$ method (as reported by E.Priolo), we think, that the difference between the $PSi-2$ and the $SPEM$ method is not due to the accuracy problems of $PSi-2$ at the planar free-surface parts. Another indication for this statement is the close agreement of $PSi-2$ and $SPEM$ results for the planar-surface models.

The difference might be caused by different approximation of the corner, in $PSi-2$ and $SPEM$. Our solution is supported by the fact, that it has been found insensitive of different corner formulations, it agreed with homogeneous FD method rather well, and the solution is consistent with the free-surface condition in sense of section 3.3.5. On the other hand, the $SPEM$ is a more accurate method, in general. Therefore, the disagreement needs further investigation.

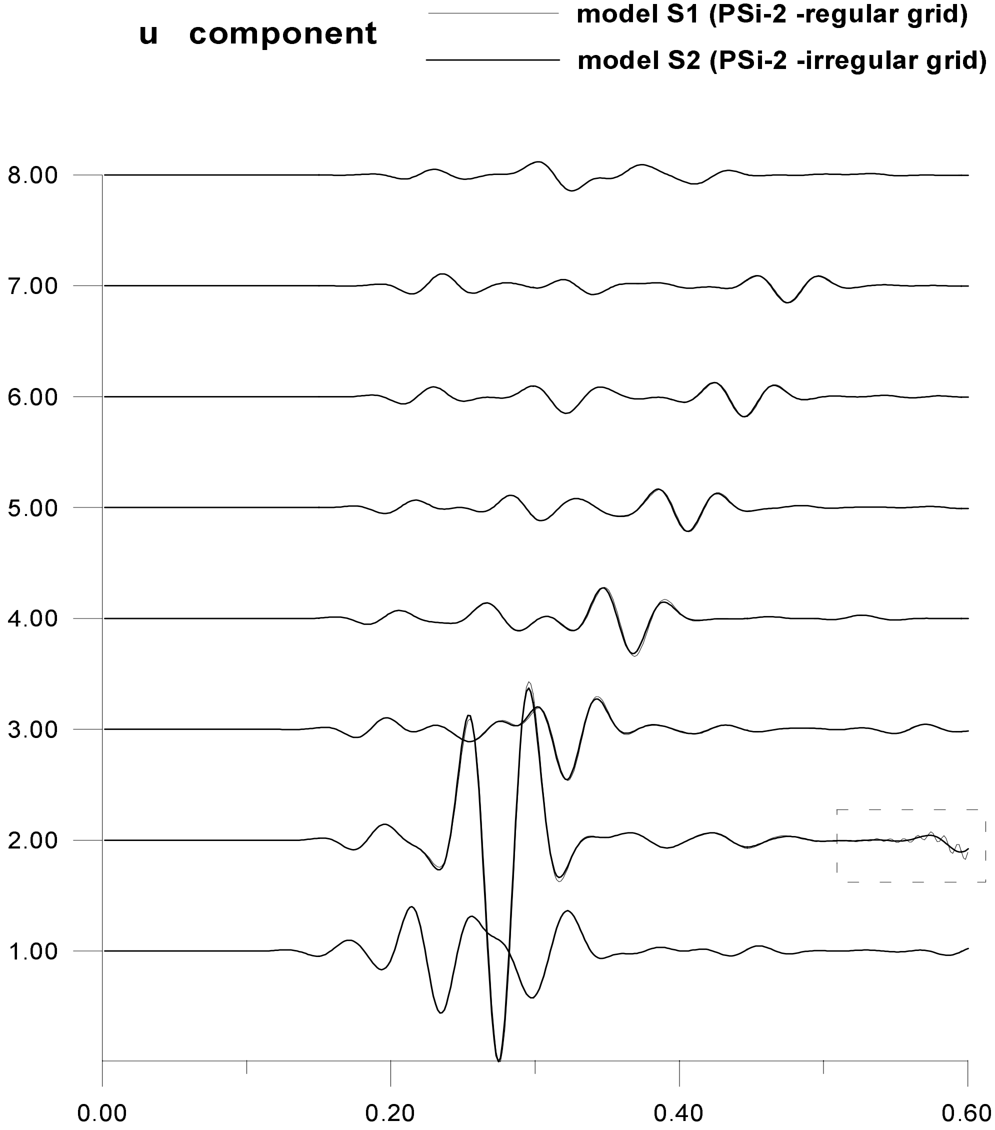

Figure 5.40: *Comparison of synthetics from models with regular and irregular grids. The dashed frame indicates the instability caused by violating the condition of stability 3.44 (described in section 3.3.6, subsection* I*).*

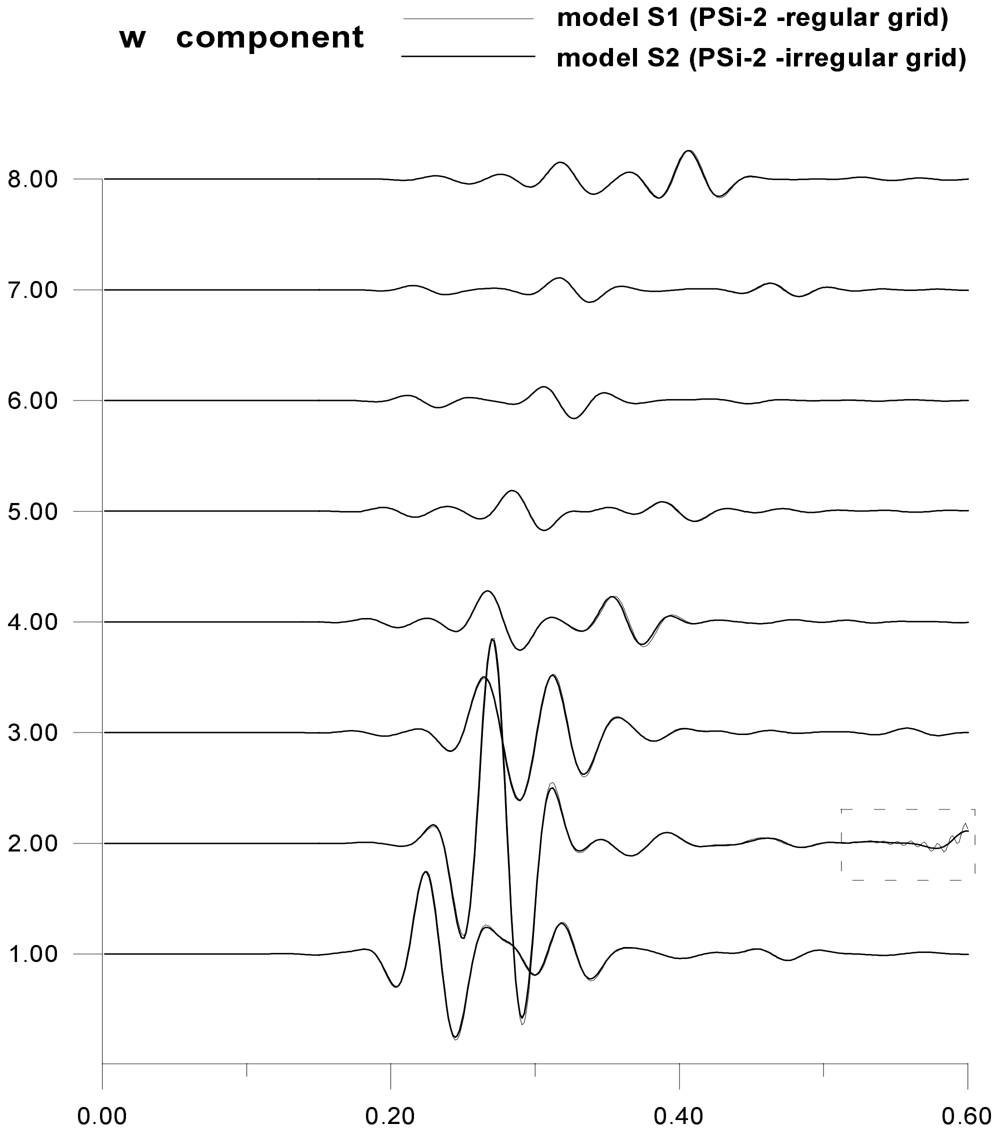

Figure 5.41: *Comparison of synthetics from models with regular and irregular grids. The dashed frame indicates the instability caused by violating the condition of stability 3.44 (described in section 3.3.6, subsection* I*).*

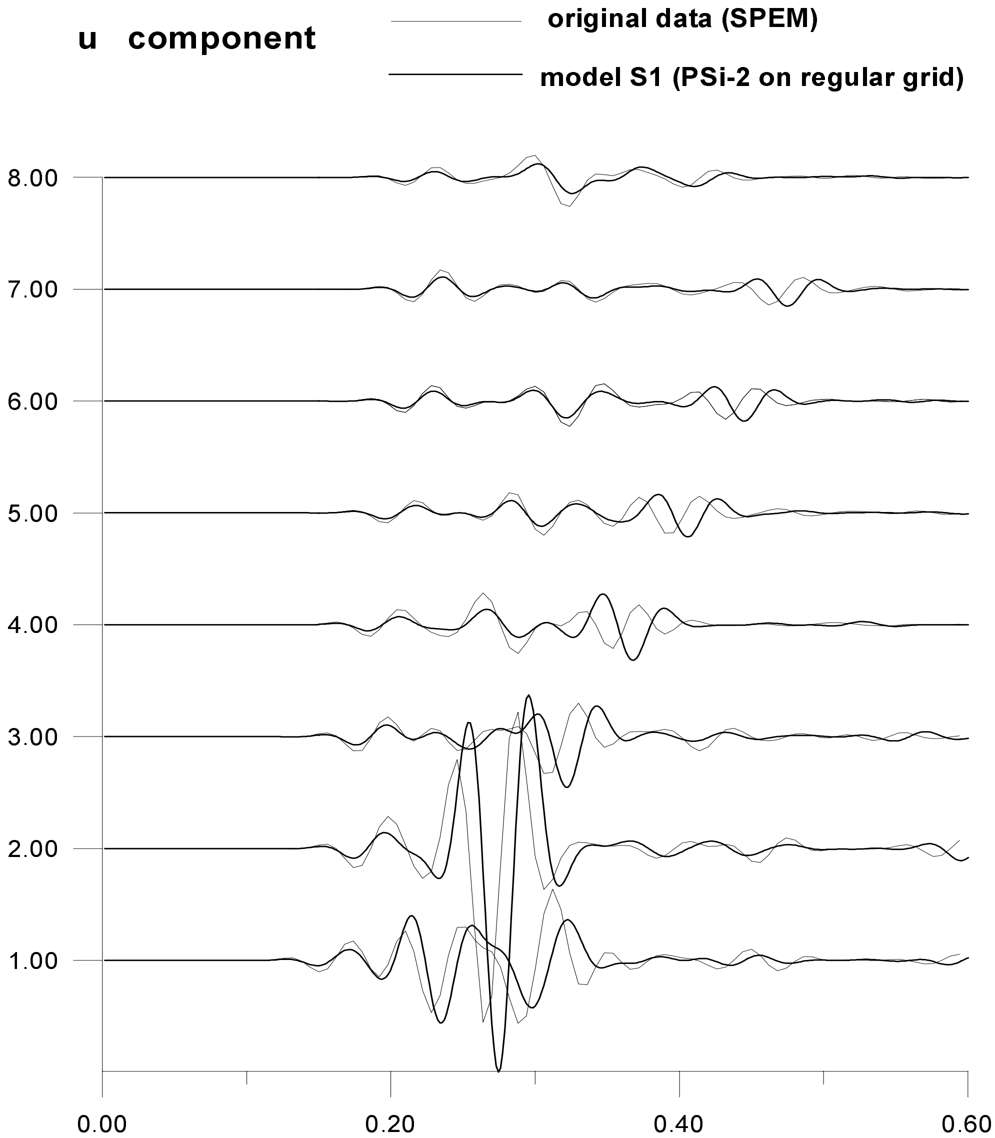

Figure 5.42: *Synthetics from the model with regular grid compared with the $SPEM$ results.*

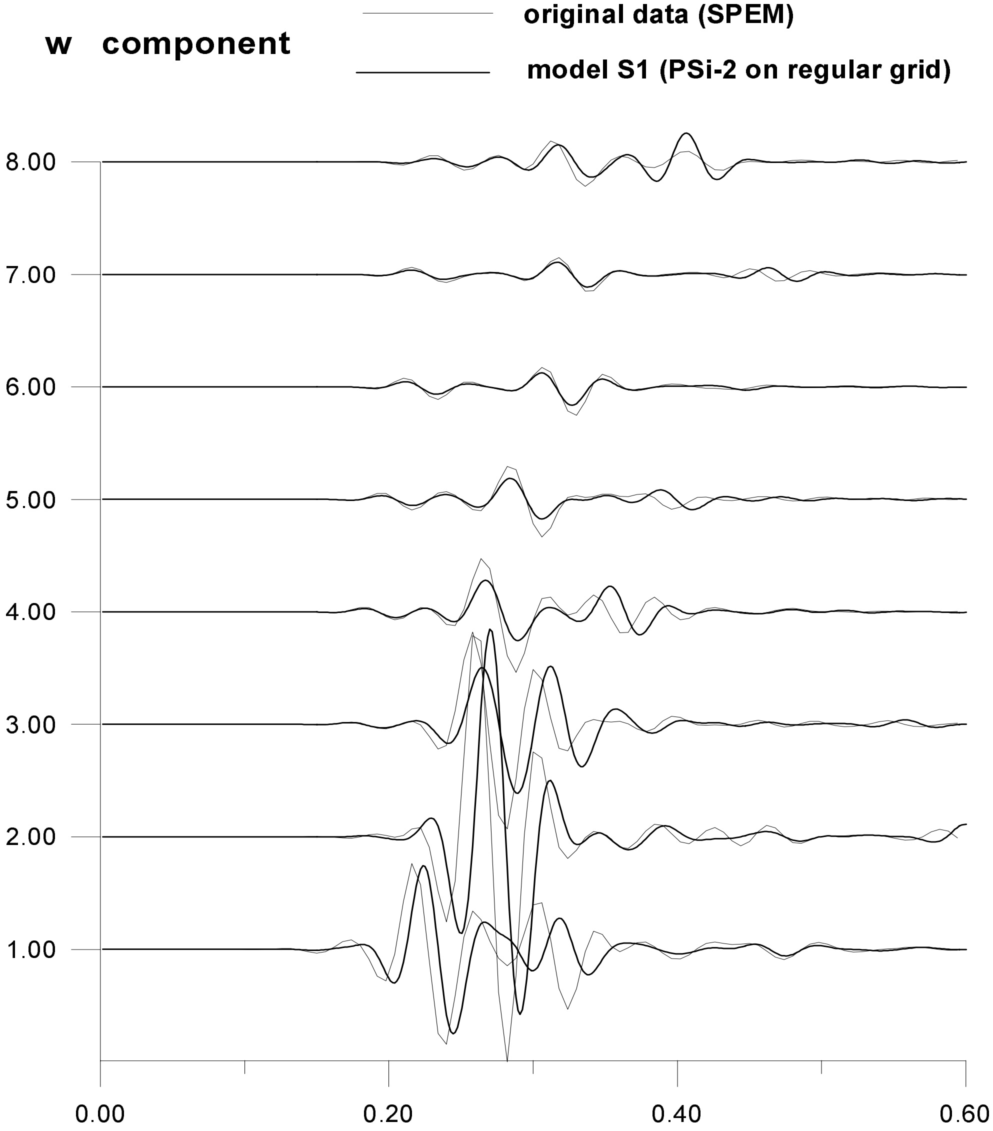

Figure 5.43: *Synthetics from the model with regular grid compared with the $SPEM$ results.*

Chapter 6

CONCLUSION

In this thesis the $PSi-2$ FD scheme for the irregular grid models (heterogeneous formulation) has been derived. This scheme transforms to the $PS-2$ scheme (Zahradník, 1995) in case of regular grid.

The stability condition for the time step, described in 3.3.6, become more restrictive for irregular grid. This phenomenon is detailed in section 3.3.6, subsection I.

The $PSi-2$ is unstable in cases shown in figures 3.7, and 3.8. The instability appears due to the heterogeneous formalism, and consequently to the geometrical averaging when evaluating the effective parameters (even in case when the stability condition for the time step Δt is fulfilled). To stabilize the model, further steps in the model approximation to the prescribed surface must be employed. These artificial modifications of the surface form are specified in section 3.3.6, subsection II, and indicated in figures 3.7, and 3.8.

The $PSi-2$ was tested on models with plane topography and plane interfaces (see section 5.1). The irregular grid models had denser grid meshing along the interface (figures 5.9, 5.17), and the surface. The results were compared with the $SPEM$ method computations for the same models (Priolo, Zahradník 1994). An improvement of the agreement of the two methods, when going from the regular coarse grid to the fine irregular grid, has been found, especially for the model of the low velocity layer.

For the step-like surface of a homogeneous half-space we compared the $PSi-2$ results (model on the regular grid) with results obtained by FD *homogeneous* formulation (Hong & Bond, 1986). The results show a close agreement as far as the accuracy of the data, retrieved from a printed copy, makes it possible.

For the ridge-like surface of a homogeneous half-space we have shown the convergency of the results for model on fine irregular and fine regular grids. The results were compared with those obtained from the Boundary Integral Equation Method ($BIEM$) (Gaffet & Bouchon, 1989), and a certain disagreement has been found. The difference is greater for the w component of the displacement. The $BIEM$ synthetics contain high frequency oscillations. The question is, whether the oscillations could be smaller in case of finer sampling of the surface, which, in this comparison, goes from 14 m (for high frequencies) to 47 m (for low frequencies) (personal communication with S. Gaffet). Model with the finest irregular grid computed by the $PSi-2$ had grid step along the topography equal to 3.333 m.

The step-like layer of low velocities underlain by a homogeneous half-space was computed for the regular coarse grid and for the irregular grid with finer meshing along the interfaces, and the free surface (see figure 5.39). The results for these two models almost did not differ. However, the $PSi-2$ differs form the synthetics computed by the $SPEM$. The previous experiments have shown , that the agreement of these two methods for the planar free surface models (even with discontinuities) has been very close. The difference appears for the Rayleigh wave that is propagating along the vertical free surface downwards. This may lead to conclusion, that this wave is created by unsatisfied free-surface corner condition, but this is unlikely because both methods have self similar results for models with finer grids. Moreover, we also computed the models on the regular coarse and the irregular fine grid with corner points (receivers $R2$, $R4$) obtained by extrapolation, and/or interpolation, and the results had again a very close agreement. It is also to mention that our theoretical analysis of the consistency with the free-surface conditions indicates, that the $PSi-2$ approximation to the corners is applicable.

The reasons of the difference between our $PSi-2$ solution and the $BIEM$ and $SPEM$ approaches is not yet clear, and the investigation should continue.

References

Aboudi, J., (1971). Numerical simulation of seismic sources. *Geophysics*, **36**, 810–821.

Alford, R., M., Boore, M., D., and Kelly, K., R., (1974). Accuracy of finite-difference modeling of the acoustic wave equation. *Geophysics*, **39**, 834–842.

Cerjan, C., Kosloff, R., and Reshef, M., (1985). A nonreflecting boundary condition for discrete acoustic and elastic wave equations. *Geophysics*, **50**, 705–708.

Falk, J., Tessmer, E., and Gajevski, D., (1995). Seismic modelling by the finite-difference method with locally varying time steps.
EAEG meeting, Glasgow.

Falk, J., Tessmer, E., and Gajevski, D., (1995). Tube wave modelling by the finite-differences method with varying grid spacing.
EAEG meeting, Glasgow, talk D013.

Gaffet, S., and Bouchon, M., (1989). Effects of two-dimensional topographies using the discrete wavenumber-boundary integral equation method in $P-SV$ cases. *J. Acoust. Soc. Am.*, **85**, 2227–2283.

Hestholm, S., O., and Ruud, B., O., (19..). 2D Finite difference elastic wave modeling including surface topography. *Geophysical Prospecting.*

Hong, M., and Bond, L., J., (1986). Application of the finite difference method in seismic source and wave diffraction simulation. *Geophys. J. R. astr. Soc.*, **87**, 731–752.

Illan, A., (1977). Finite-difference modelling for P-pulse propagation in elastic media with arbitrary polygonal surface. *J. Geophys*, **43**, 41–58.

Jastram, C., and Tessmer, E., (1994). Elastic modelling on a grid with vertically varying spacing. *Geophysical Prospecting*, **42**, 357–370.

Jih, R., S., McLaughlin, K., L., and Der, Z., A., (1988). Free-boundary conditions of arbitrary polygonal topography in a two-dimensional explicit elastic finite-difference scheme. *Geophysics*, **53**, 1045 –1055.

Kawase, H., (1990) Effects of Topography and subsurface irregularities on strong ground motion. *Research Report.*

Moczo, P., Labak, P., Kristek, J., and Hron, F., (in press). Amplification and differential motion due to an antiplane 2-D resonance in the sediment valleys embedded in a layer over the halfspace. *Bull. Seism. Soc. Am.*.

Nielsen, P., (1994) Numerical modelling of seismic waves: On the elimination of grid artifacts. *Research Report, Norsk Hydro Research Center.*

Seriani, G., Priolo, E., Carcione, J., M., and Padovani, E., (1992). High-order spectral element method for elastic wave modelling, 62nd SEG Annual Meeting. *Expanded abstracts, New Orleans.*

Stacey, R., (1988). Improved transparent boundary formulation for the elastic-wave equation. *Bull. Seism. Soc. Am.*, **78**, 2089–2097.

Tessmer, E., Kosloff, D., and Behle, A. (1992). Elastic wave propagation simulation in the presence of surface topography. *Geophys. J. Int.*, **108**, 621–632.

Virieux, J., (1986). P-SV wave propagation in heterogeneous media: Velocity-stress finite difference method. *Geophysics*, **51**, 889–901.

Zahradník, J., (1995). Simple elastic finite-difference scheme *Bull. Seism. Soc. Am.*, **85**, 1879–1887.

Zahradník, J., and Hron, F., (1992). Robust finite-difference scheme for elastic waves on coarse grids. *Studia geoph. et geod.*, **36**.

Zahradník, J., Moczo, P., and Hron, F, (1993). Testing four elastic finite-difference schemes for behaviour at discontinuities. *Bull. Seism. Soc. Am.*, **83**, 107–129.

Zahradník, J., and Priolo, E., (1995). Heterogeneous formulations of elastodynamic equations and finite-difference schemes. *Geophys. J. Int.*, **120**, 663–676.